Correlation Between Electronic Structure and Light Emission Properties in Phosphorescent Emitters

Dissertation der Fakultät für Physik der

Ludwig-Maximilians-Universität München

vorgelegt von

Stephan Haneder

aus Regensburg

München, den 3. November 2009

Publications on results of this thesis

- *Controlling the Radiative Rate of Deep-Blue Electrophosphorescent Organometallic Complexes by Singlet-Triplet Gap Engineering*
  S. Haneder, E. Da Como, J. Feldmann, J. M. Lupton, C. Lennartz, P. Erk, E. Fuchs, O. Molt, I. Münster, C. Schildknecht, and G. Wagenblast
  Advanced Materials, **20**, 3325 (2008)

- *Effect of Electric Field on Coulomb-Stabilized Excitons in Host/Guest Systems for Deep-Blue Electrophosphorescence*
  S. Haneder, E. Da Como, J. Feldmann, M. M. Rothmann, P. Strohriegl, C. Lennartz, O. Molt, I. Münster, C. Schildknecht, and G. Wagenblast
  Advanced Functional Materials, **19**, 2416 (2009)

- *Charge-transfer states in conjugated polymer/fullerene blends: Below-gap weakly bound excitons for polymer photovoltaics*
  M. Hallermann, S. Haneder, and E. Da Como
  Appl. Phys. Lett., **93**, 053307 (2008)

- *Donor substituted 1,3,5-Triazines as Host Materials for Blue Phosphorescent Organic Light-Emitting Diodes*
  M. M. Rothmann, S. Haneder, E. Da Como, C. Schildknecht, P. Strohriegl
  Submitted

- *Spectral Diffusion in the Zero-Field Splitting of Single Phosphorescent Molecules*
  S. Haneder, E. Da Como, and J. Feldmann
  Manuscript in preparation

Further publications

- *Current-induced heating in quantum well and quantum wire intersubband emitter structure*
  T. Herrle, S. Haneder, H. P. Tranitz, M. Reinwald, and W. Wegscheider
  Appl. Phys. Lett., **91**, 201105 (2007)

- *Role of excited states for the material gain and threshold current density in quantum wire intersubband laser structures*
  T. Herrle, S. Haneder, and W. Wegscheider
  Phys. Rev. B, **73**, 205328 (2006)

Talks and contributions to conferences and workshops

- *Quenching of excitons in deep-blue emitting organic host/guest systems*
  S. Haneder, E. Da Como, J. Feldmann, M. M. Rothmann, P. Strohriegl, C. Lennartz, O. Molt, I. Münster, C. Schildknecht, and G. Wagenblast, ECME 2009, Copenhagen, Denmark, 09/2009

- *Quenching of Coulomb stabilized excitons in deep-blue emitting organic host/guest systems*
  S. Haneder, E. Da Como, J. Feldmann, M. M. Rothmann, P. Strohriegl, C. Lennartz, O. Molt, I. Münster, C. Schildknecht, and G. Wagenblast, Optics and Photonics Meeting of the SPIE 2009, San Diego, USA, 08/2009

- *Photophysics of phosphorescent complexes*
  S. Haneder, Workshop: New concepts in Nanophotonics, Garmisch-Partenkirchen, 10/2008

- *Controlling the Radiative Rate of Deep-Blue Electrophosphorescent Organometallic Complexes by Engineering the Singlet-Triplet Splitting*
  S. Haneder, E. Da Como, J. Feldmann, J. M. Lupton, C. Lennartz, O. Molt, I. Münster, C. Schildknecht, and G. Wagenblast, CLEO 2008, San Jose, USA, 05/2008

- *Tuning of the radiative rate in deep-blue phosphorescent complexes by spin-orbit coupling and singlet-triplet splitting*
  S. Haneder, E. Da Como, J. Feldmann, J. M. Lupton, C. Lennartz, P. Erk, E. Fuchs, O. Molt, I. Münster, C. Schildknecht, and G. Wagenblast, Optics and Photonics Meeting of the SPIE Europe 2008, Strasbourg, France, 04/2008

- *Tuning of the radiative rate in deep blue emitting phosphorescent complexes for OLED application*
  S. Haneder, E. Da Como, J. Feldmann, J. M. Lupton, C. Lennartz, P. Erk, E. Fuchs, O. Molt, I. Münster, C. Schildknecht, and G. Wagenblast, Optics and Photonics Meeting of the SPIE 2008, San Jose, USA, 01/2008

- *Tuning of the radiative rate in deep blue emitting phosphorescent complexes for OLED application*
  S. Haneder, E. Da Como, J. Feldmann, J. M. Lupton, C. Lennartz, P. Erk, E. Fuchs, O. Molt, I. Münster, C. Schildknecht, and G. Wagenblast, ECOER 2007, Varenna, Italy, 10/2007

- *Influence of the metal ion and excited state delocalisation on spin-orbit coupling in blue emitting phosphorescent complexes for organic electroluminescence*
  S. Haneder, E. Da Como, J. Feldmann, J. M. Lupton, C. Lennartz, O. Molt, I. Münster, C. Schildknecht, and G. Wagenblast, ICP 2007, Köln, 08/2007

- *Organometallic complexes: applications as emitters in OLEDs and as probes in biophysics*
  S. Haneder, Workshop Nano for Life Science, Riezlern, Austria, 07/2007

- *Photophysical properties of deep blue emitting Iridium complexes*
  S. Haneder, E. Da Como, A. Rogach J. Feldmann, J. M. Lupton, P. Erk, E. Fuchs, O. Molt, and G. Wagenblast, DPG Tagung, Regensburg, 03/2007

- *Effect of spin-orbit coupling on emission properties of organometallic complexes*
  S. Haneder, E. Da Como, A. Rogach, J. Feldmann, J. M. Lupton, P. Erk, O. Molt, and G. Wagenblast, Winter school, Edmonton, Canada, 03/2007

- *Photophysical properties of deep blue emitting Iridium complexes*
  S. Haneder, E. Da Como, A. Rogach J. Feldmann, J. M. Lupton, P. Erk, E. Fuchs, K. Kahle, O. Molt, and G. Wagenblast, CeNS Joint Workshop, Venedig, Italy, 09/2006

To my parents

Contents

Abstract

In this work we correlate the electronic structure of organometallic complexes to their unique photophysical properties. A detailed understanding of their photophysical parameters is essential for their application as emitters in organic light-emitting diodes (OLEDs).

First, we analyzed the physical parameters which control the radiative rate in a series of phosphorescent organometallic complexes emitting in the blue. By means of low temperature time-gated spectroscopy we were able to observe fluorescence from these nominally phosphorescent molecules, which allows us to extract the singlet-triplet splitting ΔE_{ST}. These experimentally determined values were compared with calculated ones showing a remarkable agreement. ΔE_{ST} has been correlated with the radiative rate, with small values inducing high radiative rates. These findings are of particular interest for the design of phosphorescent complexes. Indeed, a higher phosphorescence radiative rate can decrease the recombination time of excited states and reduce processes detrimental to the efficiency of OLEDs, such as exciton charge-carrier quenching or triplet-triplet annihilation.

To further reveal the intricate electronic structure of the triplet in phosphorescent molecules, we employed single molecule spectroscopy, which allows to overcome the inhomogeneous spectral broadening of the ensemble. First, we demonstrated the detection of single emitters, which is experimentally challenging due to the relatively low phosphorescence radiative rate. This was done by observing a blinking behavior of the phosphorescence intensity and very narrow emission features with linewidths of $0.3\,\mathrm{meV}$. Furthermore, we observed the occurrence of two peaks in the phosphorescence spectra, which represent the zero-field splitting of the emitting triplet state. The detected zero-field splitting shows spectral diffusion and fluctuations in its energetic distribution. These phenomena are ascribed to modifications in the molecular geometry or fluctuations in the local environment of the emitter, which in turn modulate the effectiveness of spin-orbit coupling to the emitting triplet state. Our findings are of general importance for the understanding of the nature of the excited triplet state.

Besides the properties of emitter molecules, we also investigated loss processes occurring in the emitting layer of OLEDs consisting of a host/guest system. In particular, the effect of an electric field on the phosphorescence intensity of a deep-blue-emitting organometallic complex dispersed in different host materials was analyzed. While the hosts are characterized by a higher triplet excitonic level with respect to the emitter, ensuring efficient energy transfer and exciton confinement, the host materials differ in the highest occupied molecular orbital alignment, forming type I and type II host/guest heterostructures. We report a strong field dependent quenching, up to $25\,\%$, of the phosphorescence for thin films of the pure emitter and the type II heterostructure. These results highlight the importance of energy level alignment in the choice of suitable host materials for deep-blue OLEDs and elucidate the role of organic heterostructures in exciton dissociation.

Abstract

Kurzfassung

In dieser Arbeit wird die elektronische Struktur von organometallischen Komplexen mit ihren einzigartigen photophysikalischen Eigenschaften korreliert. Ein detailliertes Verständnis ihrer photophysikalischen Parameter ist notwendig für ihre Verwendung in organischen Leuchtdioden (OLEDs).

Zuerst wurden die physikalischen Parameter analysiert, welche die strahlende Rate in einer Serie von blau phosphoreszierenden organometallischen Komplexen beeinflusst. Durch zeitaufgelöste Messungen bei tiefer Temperatur sind wir in der Lage Fluoreszenz von diesen nominell phosphoreszierenden Molekülen zu messen und somit die Singulett-Triplett Aufspaltung ΔE_{ST} zu bestimmen. Diese experimentell bestimmten Werte zeigen eine bemerkenswerte Übereinstimmung mit berechneten Werten. ΔE_{ST} wurde mit dem der strahlende Rate korreliert, wobei ein kleiner Wert eine hohe strahlende Rate hervorruft. Diese Ergebnisse sind von besonderem Interesse für die Gestaltung von phosphoreszierenden Komplexen. Eine höhere strahlende Rate kann nicht nur die Rekombinationszeit des angeregten Zustandes verkürzen, sondern auch auch Prozesse mindern, die schädlich für die Effizienz von OLEDs sind.

Um ein besseres Verständnis der komplexen elektronischen Struktur des Triplettzustandes in organometallischen Molekülen zu erhalten, wurde Einzelmolekülspektroskopie verwendet. Diese Methode erlaubt es die inhomogene Verbreiterung des Ensembles zu überwinden. Zuerst wurde die Detektion von einzelnen phosphoreszierenden Emittern nachgewiesen, was aufgrund der relativ geringen strahlenden Rate der untersuchten Materialien eine Herausforderung darstellt. Dies geschah durch Beobachtung eines Blinkverhaltens der Emissionsintensität und von schmalbandigen Emissionslinien. Des Weiteren wurde das Auftreten von zwei Emissionsmaxima in den Spektren einzelner Emitter feszgestellt, welche die Nullfeldaufspaltung des emittierenden Triplettzustandes darstellen. Die Nullfeldaufspaltung zeigt spektrale Diffusion und Schwankungen in ihrer energetischen Verteilung. Diese Phänomene ordnen wir Modifikationen in der molekularen Struktur oder Fluktuationen in der lokalen Umgebung des Emitters zu, welche wiederum Schwankungen in der Spin-Bahn Kopplung hervorrufen.

Neben den Eigenschaften von Emittermaterialien wurden auch Verlustprozesse in Emissionsschichten von OLEDs, die aus Wirt/Gast Systemen bestehen, untersucht. Im Speziellen wurde der Einfluss eines elektrischen Feldes auf die Phosphoreszenzintensität eines tiefblau emittierenden organometallischen Komplexes, der in verschiedene Wirtsmateralen dotiert wurde, eingehend analysiert. Das angeregte Triplettniveau der verwendeten Wirte besitzt dabei eine höhere Energie als das des Emitters, was einen effizienten Energietransport zum Emitter gewährleistet. Jedoch unterscheiden sich die Wirte in der energetischen Lage des höchstbesetzten Molekülorbitals, wobei sich so genannte Typ I und Typ II Wirt/Gast Heterostrukturen ausbilden. Für Filme bestehend aus reinem Emitter und Typ II Heterostrukturen konnte eine starke feldabhängige Unterdrückung der Phosphoreszenzintensität von bis zu 25 % beobachtet werden. Diese Ergebnisse zeigen die Bedeutung der Energieniveau-Anordnung bei der Wahl eines geeigneten Wirtsmaterials und klären die Rolle von organischen Heterostrukturen bei der Exzitonendissoziation auf.

Chapter 1

Introduction

Inorganic semiconductors such as silicon or germanium are the dominant materials in electronics since the 20th century. Electronic devices, like transistors, solar cells and laser diodes, based on these materials are omnipresent in our everyday life. However, at the beginning of the 21st century we are facing a new electronic revolution. This revolution is caused by the development and understanding of a new class of materials, known as organic semiconductors. The advantage of this material class is the possibility to realize new devices with unique characteristics. Flexible displays, which can be rolled up like a newspaper or flexible solar cells, which can be implemented in clothes and therefore used to charge electronic devices like cell phones or mp3 players can be realized by employing organic semiconductors. Another advantage is the possibility of low-cost production, e.g. inkjet printed integrated circuits or solar cells. The importance of organic semiconductors is reflected in the award of the Nobel prize in chemistry in the year 2000 given to Alan Heeger, Alan MacDiarmid and Hideki Shirakawa for their discovery and development of conducting conjugated polymers [1, 2].

While these materials do not reach the carrier mobilities of inorganic semiconductors, other physical properties such as their high photoluminescence quantum efficiency propose them as materials of choice for emission applications. In the 1960s investigations on molecular crystals were intensified by many research groups due to the discovery of electroluminescence [3, 4]. During that time a basic understanding of the physical processes of organic semiconductors was established [5]. However, the demonstration of an efficient organic light-emitting diode (OLED) was not achieved. The main hindrances were the too high crystal thickness and insufficient material stability. With the realization of a reasonably efficient OLED the situation changed and

the interest in organic semiconductors increased further [6, 7]. The key point of these demonstrations was to use amorphous thin films of organic semiconductors (of only a few hundred nanometer thickness). In the following years OLEDs were optimized and their efficiency and stability increased [8]. The initial motivations for pursuing this research were the outstanding properties of these devices compared to liquid crystal displays, which are in particular their self-luminous properties resulting in an improved viewing performance as well as higher contrast and brightness [9].

An important development step for the use of organic diodes not only for displays, but also for solid state lighting was realized by the group of Forrest in the year 1998 [10]. The key idea of that study was the use of organometallic complexes as emitters in OLEDs. Because of their peculiar electronic structure, this class of material is suitable for achieving efficient electrophosphorescence necessary for solid state lighting. In OLEDs, light emission occurs via a recombination of electrons and holes. Due to spin statistics this process leads to the formation of 25 % singlets and 75 % triplets. In conventional devices based on purely organic molecules only singlets can be harvested and therefore 75 % of the input energy is transfered to heat and lost for light generation [11]. However, the above mentioned organometallic complexes have the possibility to harvest both singlets and triplets. Therefore, devices with such emitters can reach efficiencies four times larger than conventional ones [12]. Highly efficient OLEDs in the green and red spectral range have been realized during the last years [13, 14], but there is still a lack of a stable and efficient device in the blue spectral range. Such a color is needed for white light generation, which is a key issue because of the wide range of applications involving full-color displays and lighting [15]. Owing to the multi-stack architectures (transport and emitting layers) typically used in highly efficient OLEDs, blue emission can be achieved by the design of several high bandgap materials making up the device [10]. In the framework of this work we mainly focused on the development and understanding of materials emitting in the blue spectral range. Here it is worth to mention the parallelism with inorganic semiconductors lasers, where for many years the blue part of the spectrum has been challenging to develop till the recent results on Gallium nitride diodes [16].

While organometallic complexes are the material of choice for efficient OLEDs, because of their relatively long emission lifetime, different loss mechanisms are pronounced and limit the overall device efficiency and potentially also its stability. A shorter emission lifetime, while maintaining the efficiency would decrease the residence time of

potentially unstable excited states and limit processes detrimental to the efficiency. Therefore, one important topic in this work was to find a route to control the lifetime of emission while maintaining high quantum efficiencies. Thereby, we studied not only the properties of the ensemble emission, but also those of single molecules. On the basis of this technique many physical characteristics, which influence the emission and are masked in ensemble studies, could be revealed for conjugated polymers as well as for inorganic quantum dots [17, 18]. Moreover, we investigated loss processes which reduce the efficiency of OLEDs. Especially quenching of excitation by the applied electric field, which is inevitably present in working devices, is discussed in detail.

The present work is arranged in following way. In chapter 2 we introduce organometallic molecules and describe their electronic structure in the general context of organic semiconductors. First, we will give a theoretical introduction to the electronic and optical properties of molecular systems with delocalized π-electrons. Afterwards organometallic complexes are presented. The focus is an understanding of the photophysical properties in this class of materials, which are relevant for the experimental results. In addition, we discuss transport processes in amorphous organic films. The chapter ends with a treatment of the device design and loss mechanisms of phosphorescent OLEDs with a particular attention on the dissociation of excitons in the presence of an electric field.

Chapter 3 describes the materials, sample preparation techniques and experimental methods used in this work. Novel organometallic complexes with carbene ligands are introduced which offer the possibility to reach efficient blue emission. Materials which are used as hosts for the emitter molecules are characterized with particular attention to their triplet energy levels. The second part of this chapter describes the sample preparation methods. In the last part we present the different spectroscopic techniques, these being time resolved - and single molecule spectroscopy.

The role of spin-orbit coupling and singlet triplet splitting in controlling the radiative rate of deep-blue organometallic complexes is investigated in chapter 4. This study considers complexes with well defined variations in the molecular structure. By using time gated photoluminescence spectroscopy we demonstrate the possibility to observe prompt fluorescence originating from a short-lived singlet state located at higher energy with respect to the emitting triplet. This allows us to determine the splitting between the emitting levels. The determined singlet-triplet splittings show a strong correlation with the radiative rate, suggesting a new approach for tuning the phosphorescence

radiative rate of organometallic complexes.

Even though the phosphorescence lifetime of organometallic complexes is still an order of magnitude higher compared to the lifetime of fluorescence, we demonstrate in chapter 5 the successful spectroscopical observation of single organometallic complexes. This method gives us important insights into the electronic structure of single emitters in the absence of the inhomogeneous spectral broadening of the ensemble. The high spectral resolution obtained by looking at single emitters allows the observation of the zero-field splitting of the emitting triplet substates. Interestingly, the zero-field splitting shows spectral diffusion, which is ascribed to modifications in the molecular geometry following the photoexcitation process and to fluctuations in the local environment of single molecules in the host.

In chapter 6 a study of the effect of an electric field on the luminescence intensity of a deep-blue triplet emitter dispersed in different host materials is presented. Electric field induced quenching has only been partially investigated for phosphorescent host/guest systems. However, such an effect appears to be significant for deep-blue emitters, where operating voltages and consequently electric fields are higher than for green and red emitters. We demonstrate that the quenching shows a strong dependence on the host/guest combination and on the emitter aggregation. This represents an important finding for the interpretation of loss processes occurring in OLEDs.

The work ends with a conclusion and outlook.

Chapter 2

Organometallic complexes for organic light-emitting diodes

This chapter gives an introduction to optical and electronic properties of organometallic complexes, which are a special class of organic molecules. First we describe the electronic properties of organic molecules with a delocalized π-electron system and review theoretical methods for determining their electronic structure. Afterwards organometallic complexes are presented. The focus is an understanding of their photophysical properties, e.g. the radiative rate and the zero-field splitting of the emitting triplet state, which are relevant for the experimental results. In addition, we discuss transport processes in amorphous organic films, both for charges and excitons. The last part of the chapter deals with device design and loss mechanisms in phosphorescent organic light-emitting diodes with a particular attention on the dissociation of excitons in the presence of an electric field.

2.1 Organic molecules with a delocalized π-electron system

Organic molecules consist mainly of atomic assemblies of the element carbon. The electrical and optical properties of these materials are determined by the chemical bonds between the carbon atoms. In the ground state the electron configuration of carbon (C) is $1s^2 \; 2s^2 2p^2$. The electrons in the outer orbitals, $2s^2 2p^2$, have the possibility to form different hybrid orbitals, which allows a multiplicity of molecular structures. Linear
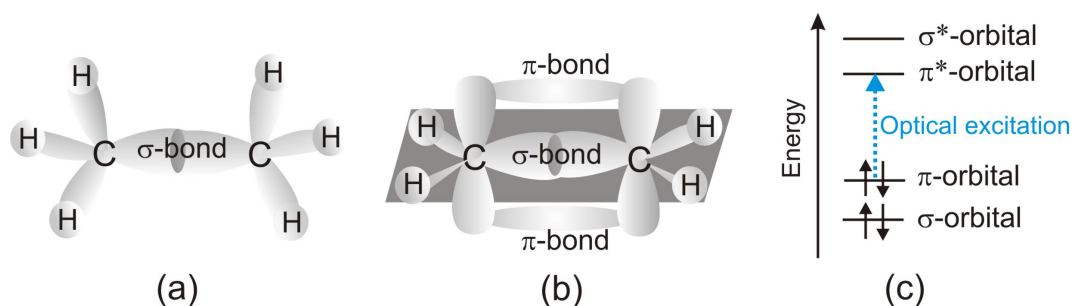
Figure 2.1: *σ- and π-bonds using the example of ethan (a) and ethene (b). The right viewgraph (c) shows a qualitative energy description of bonding and antibonding σ- and π-orbitals. In π-conjugated materials the lowest electronic excitation is a π-π^*-transition.*

combination of one *s*- and three *p*-orbitals results in the formation of four identical sp^3-hybrid orbitals, which are arranged in a tetrahedral geometry. In a molecule a single C$-$C bond is formed by the overlap of two sp^3-orbitals. The resulting σ-bond is covalent and characterized by strongly localized electrons, whose charge density is situated on the axis between two adjacent sp^3-atoms. An example of an organic molecule with sp^3-hybridization is ethane (figure 2.1(a)). It consists only of σ bonds, shows no device relevant electronic properties and from the optical point of view is inactive in the visible spectral range. Another possible configuration of carbon is the sp^2-hybridization. One s-orbital and two p-orbitals form three degenerate orbitals, which are coplanar and have an angle of 120° to each other. The overlap of two sp^2-orbitals results again in the formation of a σ-bond. The remaining p_z-orbital, is oriented perpendicular to the plane of these sp^2-orbitals. By overlapping with a neighboring p_z-orbital, a π-bond or π-orbital with a delocalized electron density is generated. As an example for the simplest π-conjugated system the σ- and π-bonds of ethene are plotted in figure 2.1 (b). The majority of the electron density in the π-orbital is found above and below the axis between two adjacent sp^2-atoms. A clear assignment of the π-electrons to one of the carbon atoms is not possible. Due to the weak overlap of the p_z-orbitals, π-bonds are much weaker than the σ ones.

The overlap of two orbitals form one bonding orbital (σ- or π-orbital), occupied with two electrons, and one antibonding molecular orbital (σ^*- or π^*-orbital). Antibonding orbitals are higher in energy than the bonding orbitals and do not contribute in the formation of the framework of nuclei constituting the molecule. Figure 2.1 (c) shows as an example the energy levels of the π-conjugated molecule ethene. The lowest electronic excitations occurs between the bonding π- and the antibonding π^*-orbital (π-π^*-transition).
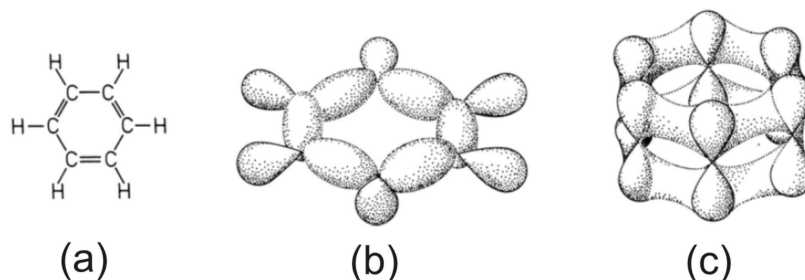
Figure 2.2: *Benzene: (a) Chemical structure, (b) charge density of σ and (c) π-electrons. Modified according to [19].*

A π-conjugated molecule can consist of many π-orbitals, which interact with each other resulting in a delocalization of the electrons over the whole conjugated system. Figure 2.2 depicts benzene as an example of a delocalized π-electron system. The σ-bonds form the structural frame of benzene (b) and the π-electrons are delocalized over the whole molecule (c). Therefore, one must not only consider the overlap of neighboring p_z-orbitals, but rather the collectivity of all p_z-orbitals. This results in the formation of a π-band of the overlapping p_z-orbitals.

If the stoichiometric ratio of single and double bonds ($C-C=C-C=C...$) in the whole system were 1:1, a semi-filled energy band with metallic character would be expected (figure 2.3 left side). However, in reality the alternating single and double bonds can not be clearly assigned to one carbon atom. In such an one-dimensional system with incompletely filled bands the Peierls instability causes a characteristic lattice distortion, which results in different single and double bonds lengths [2, 20]. Consequently, the elementary cell of the lattice is doubled, which leads to an energy gap E_G in the π-system between the bonding π- and antibonding π^*-bands (figure 2.3). Thereby, the energetically lower band is filled with electrons and the energetically higher one is unoccupied. Due to this energy gap π-conjugated systems behave like semiconductors rather than metals. The existence of an energy gap is also revealed by theoretical models, such as in the theory of Su-Schrieffer-Heeger (SSH-model) [21]. By controlling the degree of conjugation length of the π-system the energy gap can be tuned between $1.5\,\text{eV}$ and $3\,\text{eV}$, leading to absorption or emission across the whole visible and near infrared range [19].

The occurrence of an energy gap suggests analogies to inorganic semiconductors. However, due to a high degree of disorder, the electronic properties of organic semiconductors do not show a perfect periodicity, neither inside the single molecules nor in the solid state body consisting of many, often randomly arranged molecules. A high
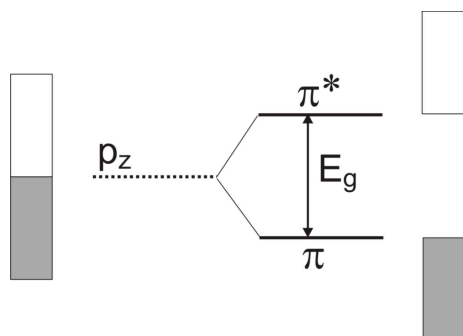
Figure 2.3: *Formation of an energy band due to overlapping p_z-orbitals (left side). In an one-dimensional system with incompletely filled bands the Peierls instability results in the formation of an energy gap E_G between the energetic lower π- and the energetic higher π^*-bands. The gray region denotes the occupation of orbitals in the ground state.*

degree of order can be achieved in molecular crystals of small molecules. However, these are difficult to produce and implement in devices. Therefore, crystals have a limited role in the production of organic optoelectronic devices [22]. Thus, we will not go into detail about the properties of organic crystals and restrict ourselves to isolated molecules and amorphous films. In this case the electronic wave function is localized on the organic compound and the dielectric constant is much lower ($\epsilon \approx 2\text{-}4$) than for an inorganic semiconductor like silicon ($\epsilon_{Si} \approx 11$). As a consequence, the exciton binding energy of electron-hole pairs is high ($0.3\,\text{eV}$ to $1\,\text{eV}$) and the localization of the excitation is pronounced [23, 24, 25]. Therefore, the optical properties of organic molecules are dominated by molecular characteristics rather than the intermolecular interactions in the solid.

It is useful at this point to distinguish between the two major classes of organic compounds, low molecular weight materials, often referred to as small molecules, and polymers. Both have in common a conjugated π-electron system. While small molecules, as the name implies, have a low molecular weight of typically lower than 1000, polymers are large molecules composed of many repeating structural units connected by chemical bonds. An important difference between these two classes of materials is in the way they are processed to form thin films. Small molecules are usually deposited from the gas phase by evaporation, resulting in very pure layers of controlled thickness. On the contrary polymers can only be processed from solution, e.g. by spin-coating or printing techniques.

Figure 2.4 (a) shows an example of a conjugated polymer, polythiophene. The squared bracket labels the repeating unit of the polymer, which is repeated n-times. The number of repeat units can be determined by measuring the molecular weight of the polymer. The π-system is not delocalized over the whole polymer. Defects, kinks and deviations cause a limitation of π-interaction and the occurrence of so-called con-
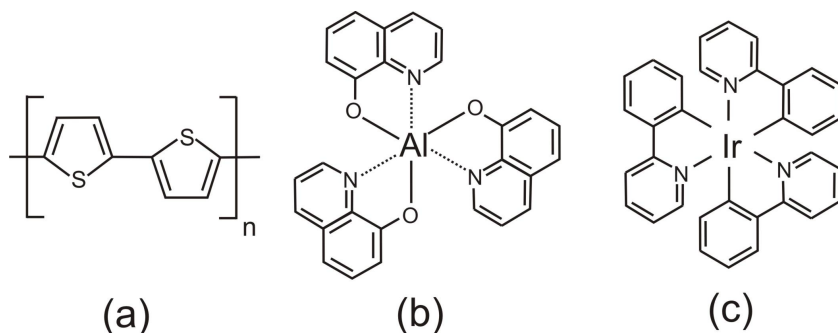
Figure 2.4: *(a) Chemical structure of the polymer polythiophene, (b) of the small molecule Alq3 and (c) the organometallic complex Ir(ppy)$_3$.*

jugation lengths [17]. A special class of low molecular weight materials are so called organometallic complexes, composed of an organic π-conjugated ligand bonding to a metal ion. The eminent advantage of such molecules, which will be discussed in detail in section 2.2, is their high luminescence efficiency upon electrical excitation. Figure 2.4 (b) and (c) show two examples of organometallic complexes, aluminum-tris(8-hydroxychinolin) (Alq3) and iridium tris(2-phenylpyridine) (Ir(ppy)$_3$). The metal ions are aluminum in the first and iridium in the second case. In both molecules the metal core is chemically bound to three identical organic ligands. Organometallic complexes were originally developed for the use in solar-energy conversion and catalysis. Within the last two decades they have triggered a lot of interest due to their applicability in organic light-emitting diodes (OLEDs) [26].

2.1.1 Quantum mechanical description

Quantum mechanics provides a mathematical framework for understanding the electronic structure, energetics and dynamics of a molecular system on the basis of wave functions, Ψ. If Ψ is known, it is in principle possible to calculate the average value of any experimental observable for an assumed set of initial conditions and interactions. However, even for the simplest organic molecules Ψ and also the initial conditions and/or interactions cannot be calculated in a precise manner [19]. As a result, one has to develop approximations to calculate wave functions in order to achieve quantitative comparisons with experiments. One important method for approximating wave functions was proposed by Born-Oppenheimer [19]. This approximation relies on the fact that nuclei are much more massive than electrons. Therefore, electron motions are much faster than nuclear motions, which are parametrized as fixed in space coor-

dinates. This allows us to tread both motions separately in terms of an approximate wave function, where the nuclei provide a fixed background potential for the electrons. The many-body Schrödinger-equation for a stationary electronic state, described by the wave function Ψ, is then given by

$$\widehat{H}\Psi(\mathbf{r}) = \left\{ -\frac{\hbar^2}{2m_e}\sum_j \nabla_j^2 - \sum_{j,k} \frac{Z_l e^2}{|\mathbf{r}_j - \mathbf{R}_k|} + \frac{1}{2}\sum_{j \neq l} \frac{e^2}{|\mathbf{r}_j - \mathbf{r}_l|} \right\} \Psi(\mathbf{r}) = E\Psi(\mathbf{r}). \quad (2.1)$$

r_j are the coordinates of the electrons and R_k those of the nuclei. Z denotes the atomic number, $\widehat{H}$ the Hamilton operator, e the electric charge, m_e the mass of the electron, $\hbar$ the reduced Planck's constant and E the energy. The first term of the Hamilton operator is the kinetic energy, the second one describes the electrostatic interactions between nuclei and electrons and the third one between electrons.

Generally, the calculation of the electron-electron interaction requires time-consuming computing for many-electron systems. Therefore, many sophisticated methods for solving the many-body Schrödinger equation exist. One approach is based on approximation procedures (self-consistent methods). In the Hartree-Fock method, the wave function of all N electrons can be described as a product of the wave functions of the single electrons (Slater determinate)[19]. The interaction of individual electrons with any other electron is described by an effective potential created by the remaining electrons. By involving the variational principle, one can derive a set of N coupled equations. The equations can then be solved by an iterative, self-consistent calculation and finally one obtains the molecular orbitals and their energies. The disadvantage of the Hartree-Fock method is, that it can only be employed for molecules with a small total number of chemically active electrons, typically smaller than ten [27]. Larger, more complex systems need a huge computational effort and calculations cannot be performed anymore within a justifiable time frame.

For the determination of molecular orbitals in π-conjugated systems, Erich Hückel proposed a very simple method based on the linear combination of atomic orbitals (LCAO) [19]. Thereby, the following approximations are made:

- Only π electrons are considered because these determine the general properties of π-conjugated molecules. σ-electrons, while creating the molecular skeleton, are not considered in the calculation.

- At the same time simplifications based on orbital symmetry considerations are

made.

This so-called Hückel method is suitable for the calculation of simple π-conjugated systems like benzene [19]. An extension of the Hückel method is the model from Su-Schrieffer-Heeger [21, 28], which was mainly developed for calculations of polymers. It includes electron-phonon interactions, but neglects electron-electron interaction. In this model strong electron-phonon coupling causes an energy gap between the highest occupied molecular orbital (HOMO) and lowest unoccupied molecular orbital (LUMO).

An appealing alternative to the approximation methods above is the time-dependent density functional theory, which is a generalization of the stationary density functional theory (DFT) to time-dependent potentials. The fundamental variable is no longer the wave function, but the electron density. First we start with a description of the DFT.

In 1964 Hohenberg and Kohn discovered that for a full description of a stationary electric system with N electrons it is sufficient to know its electron density in the ground state $n(\mathbf{r})$ [29]. Out of this quantity one can deduce all other properties of the ground state. This means that all observables are functions of the electron density [30]. In this model the many-body problem is cast into an auxiliary system of noninteracting electrons, which are subject to a local effective external potential V_{KS} (Kohn-Sham-approach) [31]. To determine the electron density, N single electron wave functions Ψ_j, Kohn-Sham functions, are introduced, which satisfy the Kohn-Sham equations

$$\widehat{H}_{KS}\Psi_j(\mathbf{r}) = \left\{ -\frac{\hbar^2}{2m_e}\nabla^2 + V_{KS}[n](\mathbf{r}) \right\} \Psi_j(\mathbf{r}) = E_j\Psi_j(\mathbf{r}). \qquad (2.2)$$

Thus, the Kohn-Sham approach provides a way to map the many-body problem onto a single-body problem, because we are now dealing with a system of independent solutions of one Schrödinger equation.

By solving equation 2.2 one obtains Kohn-Sham functions $\Psi_j(\mathbf{r})$, which can be used to calculate the electron density

$$n(\mathbf{r}) = \sum_j^N |\Psi_j(\mathbf{r})|^2. \qquad (2.3)$$

The effective potential is given by

$$V_{KS}[n](\mathbf{r}) = V_{ext}(\mathbf{r}) + V_{Hartree}[n](\mathbf{r}) + V_{xc}[n](\mathbf{r}) \qquad (2.4)$$

The first term V_{ext} denotes the external potential due to the nuclei, whereas the second term, the Hartree term, accounts for the classical electrostatic interaction between electrons

$$V_{Hartree}[n](\mathbf{r}) = \int d^3 r` \frac{n(\mathbf{r})}{|\mathbf{r} - \mathbf{r}`|}. \tag{2.5}$$

The last term V_{xc} is called the exchange-correlation potential. It includes all nontrivial many-body interactions and has an extremely complex functional dependence on the density. However, approximations exist, which allow an accurate calculation of certain physical quantities. For example in the local density approximation it is assumed that V_{xc} is a function of the electron density at this coordinate n($\mathbf{r}$). This method is already quite accurate for a number of applications. Since V_{KS} depends on n($\mathbf{r}$) and occurs in the Kohn-Sham equations, solving equation 2.2 has to be done in a self-consistent way. In summary, in the Kohn-Sham approach it is assumed that a fictitious system of non-interacting particles exists that possesses the same density as the interacting system.

An extension of DFT is the time-dependent density functional theory (TD-DFT). The formal foundation of TD-DFT is the Runge & Gross theorem, which shows that the time-dependent wave function is equivalent to the time-dependent electronic density [32]. The scope of the extension of the DFT was the description of time-dependent phenomena like the interaction of electromagnetic fields. Especially the calculation of the energies of excited states of isolated systems by TD-DFT became very important during the last decades [27, 30, 33, 34, 35].
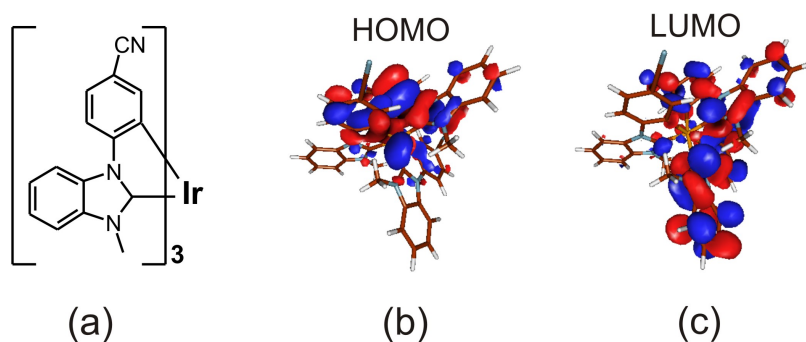
Figure 2.5: *(a) Chemical structure of the molecule Ir(cnpmbic)$_3$ consisting of an iridium atom, which is surrounded by three organic ligands. (b, c) Contour plots of the electron density of HOMO and LUMO of Ir(cnpmbic)$_3$, calculated by TD-DFT. Additionally, their geometrical structure is depicted. Calculation were obtained via the Kohn-Sham approach using the BP86 functional in combination with a split valence basis set [34].*

Figure 2.5 (a) shows the chemical structure of the molecule iridium tris(1-cyanophenyl-

3-methylbenzimidazolin-2-yilidene-C,C$^{2\text{‘}}$) (Ir(cnpmbic)$_3$), which consists of a heavy metal ion surrounded by three organic ligands. In figure 2.5 (b) contour plots of the electron density of the HOMO (b) and LUMO (c) of Ir(cnpmbic)$_3$ together with its geometrical structure are depicted. The electron density was calculated by TD-DFT. Such plots reveal the potential of TD-DFT in illustrating the spatial distribution of the electron density in the molecular frame. In section 4.4 we will explain such contour plots in more detail.

2.1.2   Optical transitions in molecules

The existence of an energy gap in molecules with a π-conjugated electron system shows the possibility of electron transitions between the HOMO and LUMO levels. By optical excitation an electron is excited from the ground state S_0 to an excited state S_n by absorption of a photon. Emission results from radiative recombination of the excited electron and the hole left in the HOMO.

In the following we consider only transitions between the ground state S$_0$ and the first excited state S$_1$. Figure 2.6 (a) and (b) show these electronic states, expressed by potential energy curves as a function of the nucleus distance R. Excitation of an electron leads to a redistribution of the electronic configuration. This new distribution changes the nuclei distances, resulting in a shift of the equilibrium distance of the potential [19]. Because of the large nucleus mass compared to the electron mass, an electronic transition occurs without changes in the positions of the nuclei (Born-Oppenheimer approximation) and therefore, it appears vertical in figure 2.6.

As shown in figure 2.6 several transitions can take place between the ground and the excited state. Every molecule reveals characteristic vibrational modes ν, which are illustrated as levels within the electronic states. Since the energy of the vibrational modes is above $100\,\text{meV}$, at room temperature only the lowest vibrational state of the ground state S$_{0,\nu=0}$ is occupied and absorption occurs from this level to vibrational levels of the excited state $S_{1,\nu\text{‘}}$. Therefore, the vibrational structure of the excited electronic state can be observed in the absorption spectrum (figure 2.6(c)). Once an electron is excited to S$_{1,\nu\text{‘}}$ it relaxes by internal conversion to the lowest vibrational level of the electronic excited state S$_{1,\nu\text{‘}=0}$. This non-radiative process happens in a very fast time regime, typically below $10^{-13}\,\text{s}$ [22]. From this state the electron can undergo a transition to a vibrational level of the electronic ground state S$_{0,\nu}$ by emitting a photon.
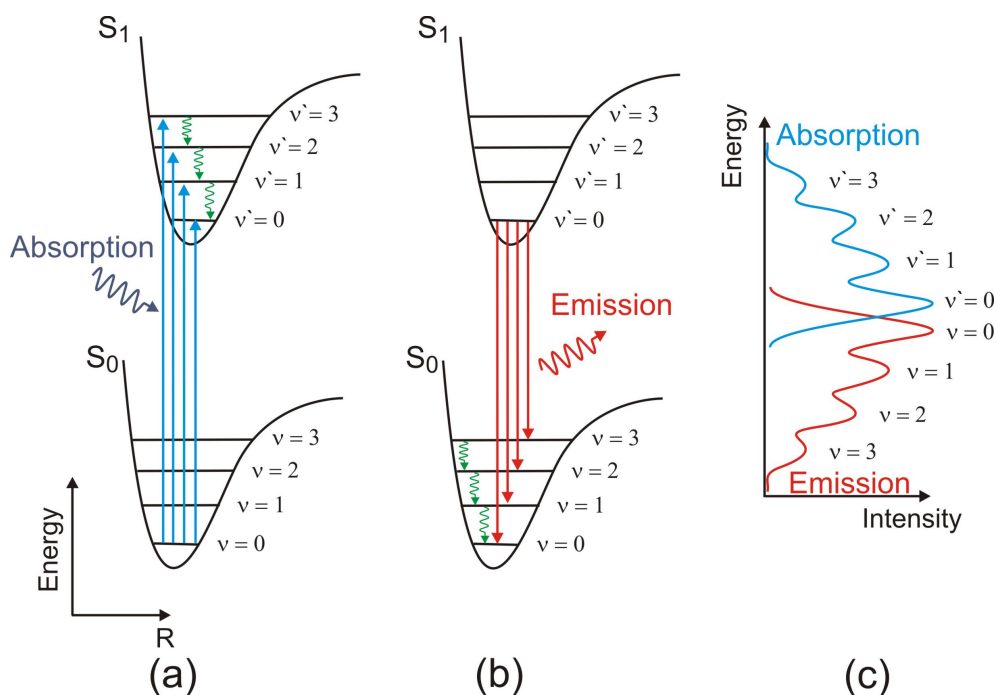
Figure 2.6: *Schematical sketch of the (a) absorption and (b) emission processes in organic molecules. The potential curve of the ground S_0 and the excited state S_1 is depicted as a function of the nuclei distance R. The vibrational levels are labeled as ν in the ground state S_0 and as $\nu`$ in the excited state S_1. (c) The absorption and emission spectrum of the respective transitions is shown together with their vibronic sidebands.*

The emission spectrum also shows vibrational levels, which appear at lower energies compared to the transition from $S_{1,0}$ to $S_{0,0}$. The transition probability between two states and therefore the intensity of an electronic transition is determined by the overlap of the wave functions in the initial and final state (Franck-Condon principle).

Typically the emission spectrum is mirror-symmetric to the absorption spectrum, whereas the energy of the emitted light is lower than that of the absorption 2.6(c). The difference between the $(\nu=0)$-$(\nu`=0)$-transition in absorption and emission is called Stokes-shift. It is caused by a reorganization of the molecule in the excited state, which leads to a dissipation of energy and thus lowering of the potential energy curve [19]. There are also other mechanisms, which lead to a reduction of the emission energy compared to the absorption energy, e.g. solvent effects, excited state reactions, complex formation and/or energy transfer [36, 37].

Photophysical processes

So far we have not considered the spin coordinate of the electron. This variable can play a crucial role in determining the optical properties of organic molecules. Once an electron is excited to a higher electronic state, it forms, together with the hole in the HOMO, a bound state, which is stabilized by Coulomb attraction. Such bound electron-hole pairs are called singlets or triplets depending on the overall electronic spin they possess.
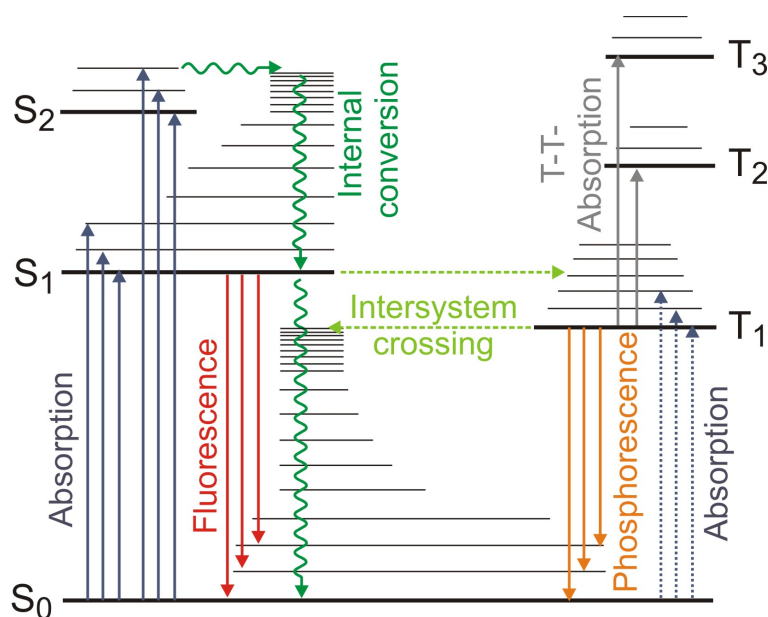
Figure 2.7: *Jablonski-diagram of a typical organic molecule. Schematically drawn are the singlet and triplet electronic states together with their vibrational levels. Besides absorption, all radiative (fluorescence and phosphorescence) and non-radiative processes (internal conversion and intersystem crossing) are shown. Taken from [19].*

A complete description of the photophysical processes between electronic states is provided by the Jablonski-diagram in figure 2.7 [22]. It includes energetically higher lying singlet (S_2) as well as triplet states (T_2, T_3) together with their vibrational levels. Optical excitation from the ground state S_0 to higher lying singlet states S_i leads to a fast non-radiative internal relaxation, typically in the ps-time range, to the first excited singlet state S_1 (Kasha´s rule) [5, 37]. The excess energy is released as phonons (heat). The difference in electronic energy between singlet and triplet states with the same electronic configuration results from a lower electron-electron repulsion in the triplet state. Thereby, the energy of T_1 is lowered by double the amount of the exchange integral J compared to S_1 [38]. For pure molecules this singlet-triplet splitting, ΔE_{ST},

is typically in the range of $0.8\,\mathrm{eV}$ [39, 40]. As shown in chapter 4, the value of ΔE_{ST} can differ dramatically in organometallic complexes from those in purely organic molecules and has an impact on the photophysical properties of these compounds.

The radiative transition from $S_1 \to S_0$ is called fluorescence and $T_1 \to S_0$ phosphorescence. The triplet state T_1 is usually occupied by intersystem-crossing (ISC) from the excited singlet state. Transitions between singlet and triplet states are formally forbidden, because they involve a change in the electron spin. However, due to spin-orbit coupling (SOC), which is introduced by nuclei in the molecule, ISC and also phosphorescence become partially allowed.

Important experimental parameters in this context are the quantum yield and the lifetime of the first excited singlet and triplet states. The quantum yield is the ratio of emitted photons to the number of absorbed photons. It is therefore a measure of the efficiency of an emission process. A general expression for the quantum yield fluorescence Φ_{Fl} and phosphorescence Φ_{Ph} is given by

$$\Phi_{Fl} = k_r^S / \left(k_r^S + k_{nr}^S \right), \tag{2.6}$$

$$\Phi_{Ph} = \Phi_{ISC} \cdot k_r^T / \left(k_r^T + k_{nr}^T \right), \tag{2.7}$$

where k_r^S (k_r^T) is the radiative rate constant for fluorescence (phosphorescence), k_{nr}^S (k_{nr}^T) the sum of all non-radiative transitions from the first excited singlet (triplet) state and Φ_{ISC} the quantum yield for ISC from the excited singlet to the triplet state. The radiative rate of emission is determined by the experimentally measurable lifetime τ of the emitting state, which is given by

$$\tau^{S,T} = 1 / \left(k_r^{S,T} + k_{nr}^{S,T} \right) \tag{2.8}$$

The lifetime in the absence of non-radiative processes is called the radiative lifetime. By measuring the quantum yield and lifetime of emission, one can experimentally identify the radiative and non-radiative rate constants of the corresponding state from the equations above. Generally, fluorescence lifetimes are in the range of 10^{-9} to $10^{-7}\,\mathrm{s}$ and phosphorescence lifetimes in the range of 10^{-6} to $10^2\,\mathrm{s}$.

Thus, the radiative rate constant of the first excited triplet state is typically very low in purely organic molecules. Therefore, instead of emitting a photon the triplet state decays by a non-radiative process. As a consequence, the quantum yield of phosphorescence is low at room temperature and difficult to measure. At cryogenic

temperatures the non-radiative decay of the T_1 state can be hindered and phosphorescence can eventually be detected by time-gated spectroscopy [39]. An enhancement of ISC and phosphorescence is achieved by the introduction of a heavy metal ion into the molecule, which significantly increases the spin-orbit coupling in the system. Thereby, the radiative lifetime of the first excited triplet state is enhanced by more than three orders of magnitude [10, 41].

In all purely organic semiconductors the triplet level leads to a fundamental limitation of the efficiency of the electroluminescence in OLEDs. Due to spin-statistics of the injected charge carriers a maximum singlet generation of 25 % is obtained [11]. The remaining 75 % of the charge carriers form triplet excitons, which are typically non-luminescent. Therefore, only 25 % of the input energy can be converted to light. However, the use of organometallic complexes as emitters in OLEDs overcomes this problem by enabling radiative recombination of the 75 % of triplet excitons as described in section 2.4 [10].

Optical excitations in organic solids

Due to the low dielectric constant in organic solids electrostatic screening is very weak and electron-electron interactions are very dominant. Once an electron is excited to a higher electronic state, it forms, together with the hole in the HOMO, a bound state, which is stabilized by Coulomb attraction. This bound electron-hole pair is termed exciton. Generally speaking, an exciton is described by a neutral delocalized wave function that moves over a certain coherence length within a lattice. The strength of
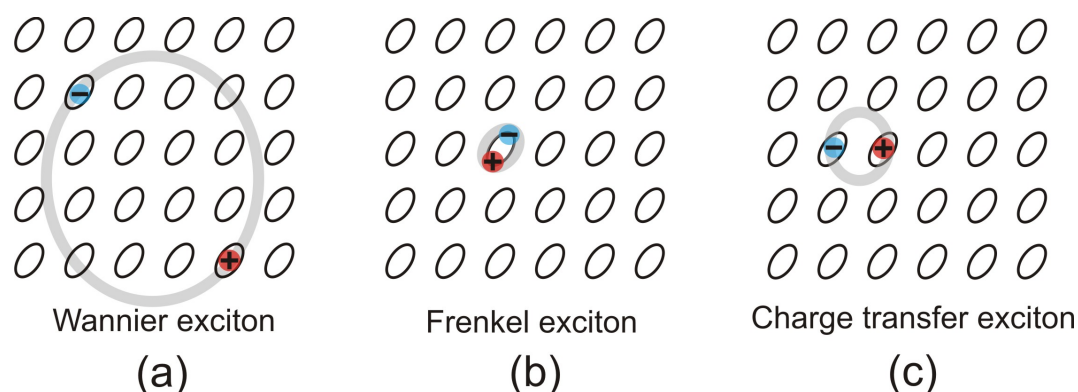
Figure 2.8: *Schematic illustration of excitons with different radius in an arrangement of molecules or atoms, (a) Wannier excitons, (b) Frenkel excitons and (c) charge transfer excitons. Adopted from [22].*

the Coulomb attraction is called binding energy E_B and is determined by the energy difference between the bound electron-hole pair and the free electron and hole. In contrast to inorganic semiconductors, where E_B is in the order of kT at room temperature, organic materials exhibit large binding energies of 0.3 - 1 eV [24, 25, 42, 43].

The size of E_B reflects the difference in the spatial extension of the electron-hole pair. In inorganic semiconductors typically only weakly bound Wannier excitons are observed, in which the radius of the exciton spans over several lattice constants (figure 2.8) (a) [44]. In contrast, in organic molecules excitons are strongly bound and located on the same molecule. Such strongly localized electron-hole pairs, which have a radius of 1 - 3 nm, are termed Frenkel excitons (figure 2.8 (b)) [45]. In addition, there are electronic excitations which are neutral but polar, and where the excited electron is transferred to the nearest or next-nearest neighboring molecule, while still remaining correlated with its parent hole. Such excitations are referred to as charge transfer (CT) excitons or polaron pairs (figure 2.8 (c)). Values of both their binding energies as well as their radii lie between Frenkel and Wannier excitons [46, 47]. As we will describe in section 2.3, organic molecules maintain the properties of the single isolated entity with only small perturbative interactions with neighboring molecules.

Exciton dissociation

Once an exciton is formed, it can be dissociated into free charge carriers. The dissociation probability shows a strong dependence upon both external electric field and temperature [48, 49, 50]. As we will discuss in chapter 6, such a process can have an impact on the efficiency of OLEDs. In the following we will give an introduction to the theoretical description of field-induced dissociation in organic semiconductors, as described by the Onsager theory [51, 52, 53].

According to this model, dissociation of excitons proceeds in the following steps: First, absorption of photons generates excitons. Then autoionization of the excited state occurs. With an efficiency of Φ_0 quasi-free electrons with a kinetic energy and holes are produced. Subsequently, these hot electrons thermalize, forming weakly bound pairs within the sphere of action of the Coulomb potential of the holes, these are referred as polaron pairs (PPs). In a final step some of these PPs are dissociated with a probability $f(r, \theta, F)$ by thermal activation or an external electric field. The remaining ones, R = 1-Φ_0, are reconverted into excitons (figure 2.9). The activation energy can be reduced by an electric field F, which modifies the Coulomb potential.
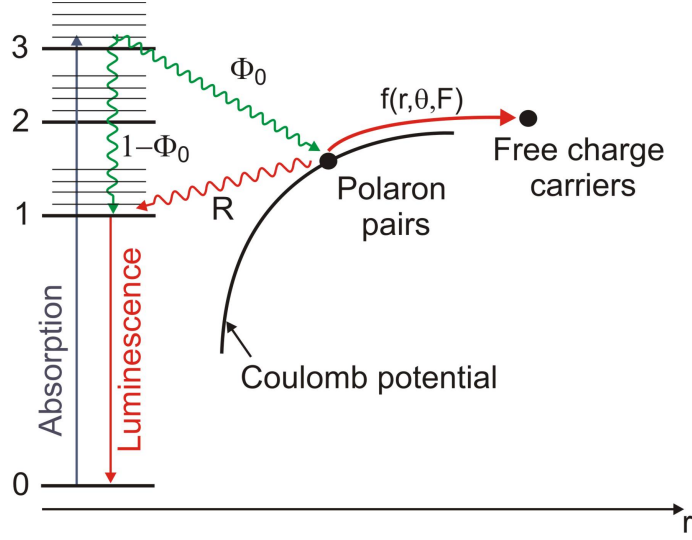
Figure 2.9: *Schematic diagram of multi-step exciton dissociation in an organic semiconductors. First, by absorption of photons, excitons in the excited states $1, 2, 3, ..$ are created. Subsequently, autoionization of excited states occurs. With an efficiency of ϕ_0 quasi-free electrons with a kinetic energy and holes are produced. The hot electrons thermalize, forming PPs within the sphere of action of the Coulomb potential of the holes. The remaining excitons $(1-\phi_0)$ relax to the first excited state 1 and decay. The probability of dissociation of PPs at a distance r at an angle θ to the applied field F is expressed by $f(r, \theta, F)$. The fraction of PPs, which return to state 1, is given by $R=1- f(r, \theta, F)$.*

The fraction of weakly bound pairs separated at a distance r with an angle θ to the applied field is given within the Onsager model [54, 55, 56]. The total dissociation efficiency is expressed by

$$\Phi(F) = \Phi_0 \int f(r, \theta, F) g(r, \theta) d\tau, \qquad (2.9)$$

where Φ_0 was described above, $g(r, \theta)$ represents the spatial distribution of PPs and $d\tau$ is the volume element. With the approximation of an isotropic density and the same separation distance for all PPs r_0, $g(r, \theta)d\tau$ can be approximated by $4\pi r^2 g(r)$, where $g(r) \approx \delta(r - r_0)/4\pi r_0^2$ is approximated by a δ-function. According to reference [56], a solution of equation 2.9 is given by

$$\Phi(r_0, F) = \Phi_0 \left[1 - \left(\frac{kT}{eFr_0} \right) \sum_{j=0}^{\infty} I_j \left(\frac{e^2}{\epsilon kT r_0} \right) I_j \left(\frac{eFr_0}{kT} \right) \right]. \qquad (2.10)$$

$I_j(x)$ is a recursive formula, which is expressed by

$$I_j(x) = I_{j-1}(x) - \frac{x^j \exp(-x)}{j!} \qquad (2.11)$$

and

$$I_0(x) = 1 - \exp(-x), \tag{2.12}$$

where $j = 1,2,3,...$ ϵ is the dielectric constant, k the Boltzmann constant, e the electric charge and T the temperature. Equation 2.10 is used in chapter 6 to fit the exciton dissociation efficiency of thin films containing emitter molecules.

The activation energy for the generation of free charge carriers is determined by the Coulomb binding energy U_{PP} of the PPs at the distance r_0:

$$U_{PP} = \frac{e^2}{4\pi\epsilon r_0} \tag{2.13}$$

2.2 Properties of organometallic complexes

Organometallic complexes are a special class of molecules. They consist of a metal ion, which is chemically bound to a framework of organic ligands. The presence of the metal ion influences not only the radiative rate of the phosphorescence or the ISC rate, but also adds excited states to the electronic spectrum compared to purely organic molecules with a π-conjugated system. In this section we will describe the electronic structure of these molecules with particular attention to their optical properties.

2.2.1 Electronic structure and excited states

The combination of a metal ion and organic ligands results in combined electronic orbitals and therefore optical transitions with hybrid characteristics. Besides ligand-centered (LC or π-π^*) transitions, which has been discussed above, pure metal (d-d^*)- and metal to ligand-charge transfer (MLCT) transitions emerge. Note, π-orbitals are associated with the organic ligands and d-orbitals with the metal. Nearly all organometallic complexes used in this work have six d electrons and 5 d-orbitals. The presence of ligands results in a splitting of the d-orbitals in energy into three lower (t_{2g}) and two higher orbitals (e_g), also called ligand field [37]. A transition between these two sets of orbitals is termed d-d^* transition. The extent of energetic splitting between t_{2g} and e_g-orbitals is described by crystal-field theory. In this model the effect of the electrostatic repulsion between the electrons of the organic ligands, which are treated as negative point-like charges, and the d-electrons of the metal is considered [57]. The investigated compounds exhibit an octahedral symmetry, where the ligands are sym-
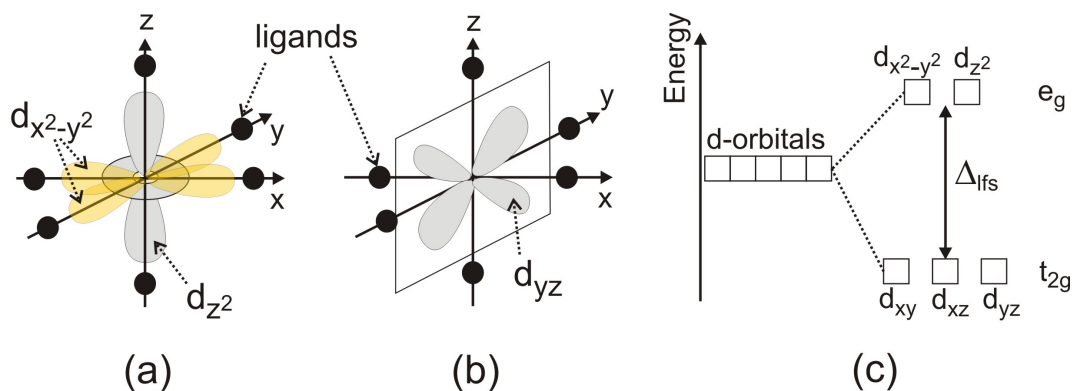
Figure 2.10: *(a,b) Orientation of selected d-orbitals relative to six octahedrally arranged ligands. The repulsion between d-electrons and ligands (black points) is higher for d_{z^2} and $d_{x^2-y^2}$-orbitals, because they are spatial closer to the ligands than the other three orbitals, e.g. d_{yz}. (c) d-orbitals split in an octahedral ligand field into two sets, where d_{xy}, d_{xz} and d_{yz}-orbitals (t_{2g}), are lower in energy than the d_{z^2} and $d_{x^2-y^2}$-orbitals (e_g). The magnitude of splitting is determined by the ligand field strength Δ_{lfs}.*

metrically arranged around the central metal atom. Figure 2.10 (a) and (b) show the orientation of selected d-orbitals relative to six octahedrally arranged ligands. Since d-electrons closer to the ligands experience a higher repulsion than those further away, the degeneracy of the d-orbitals is lost. Consequently, they split into two sets, where the d_{xy}, d_{xz} and d_{yz}-orbitals, are lower in energy than the d_{z^2} and $d_{x^2-y^2}$-orbitals (figure 2.10 (c)). The magnitude of splitting is determined by the ligand field strength Δ_{lfs}, which is mainly affected by the arrangement of the ligands around the metal ion and the nature of the ligands. Thereby, one distinguishes between weak field-ligands, which have a low electrostatic interaction with the metal ion and cause a small Δ_{lfs} and high-field ligands, which create a large Δ_{lfs}. In the latter case, the lower orbitals are typically completely filled with electrons (low spin configuration). Since the three lower and the two higher d-orbitals have the same symmetry with respect to the metal center, transitions between those orbitals are generally forbidden (Laporte selection rules). Therefore, d-d* transitions are typically non-luminescent and are not desirable as low energy emitting state. In highly luminescent molecules the crystal field strength must be strong enough to raise the d-d* transition above the π-π*- or MLCT one, which are allowed transitions. As we will mention in section 3.1, this point is especially essential for complexes which show emission in the deep-blue spectral range.

Another important transition in organometallic compounds is the MLCT transition, which takes place when the d-orbitals of the metal (d_{xy}, d_{xz} and d_{yz}) constitute the HOMO of the complex and antibonding π*-orbitals of the ligands the LUMO. In this
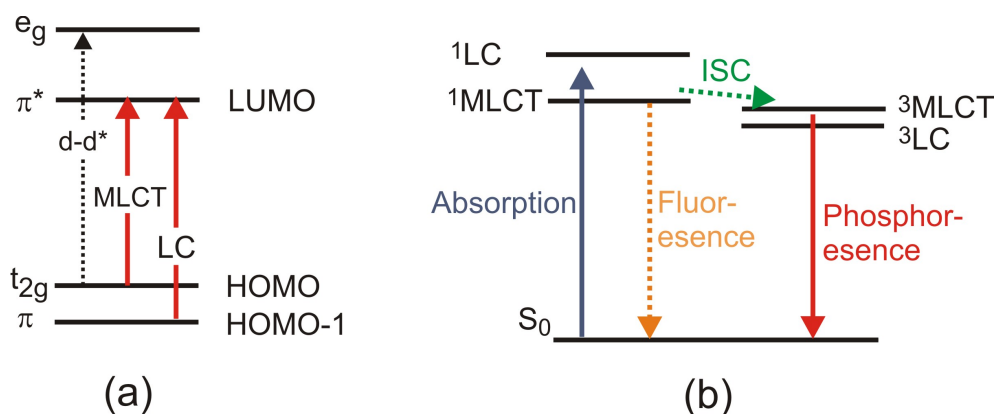
Figure 2.11: *(a) Orbital diagram for an organometallic complex showing t_{2g}, π-bonding and e_g, $\pi*$-antibonding orbitals together with the emerging transitions. (b) Simplified Jablonski diagram for the ground (S_0) and the first excited singlet (^1LC, ^1MLCT) and triplet states (^3LC, ^3MLCT).*

combination electrons are transfered from the metal to the ligands upon photoexcitation. In figure 2.11 (a) all the possible transitions in organometallic complexes are summarized. As mentioned above, d-d*-transitions are desirable energetically above the one of emitting state. In organometallic complexes used for OLEDs, MLCT and LC states are usually situated close together energetically and thereby the emitting triplet state can have more MLCT or LC character [33, 58]. In future discussions we will neglect d-d*-transitions, because of negligible influence on the emitting triplet state for the investigated organometallic complexes.

Compared to LC excitons, MLCT excitons have a large overlap with the heavy metal ion. Consequently, the SOC is higher and there is greater mixing between singlet and triplet MLCT states, which enhances the ISC and the phosphorescence rate (see section 2.2.2). A high radiative rate is essential for obtaining efficient and stable phosphorescent OLEDs, as will be discussed below. Thus, it is desirable that the emitting triplet state is a pure MLCT state or has a high MLCT character [59].

In figure 2.11 (b) a simplified Jablonski diagram for the ground and the first excited states of an organometallic compound is shown. Absorption takes place from the singlet ground state to a singlet ^{1}MLCT or ^{1}LC state. Depending on the amount of SOC, ISC lifetime to a triplet ^{3}MLCT or ^{3}LC state varies from 1 ps to a few hundred fs and the lifetime of the lowest excited triplet state lies between 1 μs and 500 μs [60, 61, 62, 63]. Because of the fast ISC rate of most organometallic complexes, fluorescence is typically very weak or even not observable in a steady state experiment. For MLCT transitions the exchange interaction and thus the singlet-triplet splitting differs

significantly compared to ligand-centered transitions. Due to a larger spatial extension of MLCT excitons, the singlet-triplet splitting is smaller compared to ligand-centered excitons. According to reference [64], the amount of splitting is in the range of $0.37\,\text{eV}$ or even smaller. Thereby, it occurs often that the singlet and triplet MLCT states lie inside the one of the LC states, as shown in figure 2.11 (b) [64, 65].

Here we remind the reader that figure 2.11 (b) is a simplified scheme. For a more detailed model one has to take into account a higher number of electronic states, which result for example from a loss of degeneracy of triplet states (section 2.2.3) [64]. Therefore, understanding the electronic structure and the resulting photophysical properties is challenging and calls for the use of advanced spectroscopical techniques. In this thesis we attempt to pinpoint the electronic structure of this class of molecules by using time-resolved and single molecule spectroscopy.

2.2.2 Spin-orbit coupling and phosphorescence decay rates

Without SOC and electron spin interactions all singlet-triplet transitions are strictly forbidden and singlet and triplet states are so-called ´pure´ states. However, SOC mixes singlet and triplet states, so that transitions between those states become allowed. SOC is the magnetic interaction between the spin magnetic momentum and the orbital magnetic momentum of an electron. In organometallic complexes the lowest triplet state mixes with one or more singlet states, which results in a high phosphorescence radiative rate. The theoretical description of state mixing is typically done by perturbation theory [66]. In this approach the Hamiltonian is split into a part, where the energy levels E_{S_n}, E_{T_n} and wave functions Φ_{S_n}, Φ_{T_n} of singlet and triplet states are considered as known and into an additional part, representing the physical disturbance to the system. As long as the magnitude of perturbation is small compared to the unperturbed Hamiltonian, the changes in various physical quantities can be expressed as corrections to those of the unperturbed system.

The phosphorescence radiative rate constant k_r is related to the energy of the emitting state E_{T_1} and its transition dipole moment $|\mu_{T_1}| = |\langle \Phi_{S_0} |e\mathbf{r}| \Phi_{T_1}\rangle|$ via [38]:

$$k_r = const \cdot E_{T_1}^3 \left|\mu_{T_1}\right|^2 . \tag{2.14}$$

According to first order perturbation theory, the transition dipole moment can be

approximated by

$$\mu_{T_1} = \sum_n \frac{\left\langle \Phi_{S_n} \left| \hat{H}_{SO} \right| \Phi_{T_1} \right\rangle}{E_{T_1} - E_{S_n}} \left\langle \Phi_{S_0} \left| e\mathbf{r} \right| \Phi_{S_n} \right\rangle, \tag{2.15}$$

where $\left\langle \Phi_{S_0} \left| e\mathbf{r} \right| \Phi_{S_n} \right\rangle$ is the transition dipole moment from the S_n singlet state to the ground state S_0, $e\mathbf{r}$ the electric dipole operator and E_{S_n}, E_{T_1}, Φ_{S_n}, Φ_{T_1} are the energies and wave functions of the Hamiltonian without spin-orbit interaction [64, 67]. $\hat{H}_{SO}$ denotes the SOC Hamiltonian. Note that in equation 2.15 we take only direct spin-orbit interaction of T_1 and S_n into account and neglect indirect interaction via vibrational mixing of T_1 with upper triplets [68]. By combining equations 2.14 and 2.15 the phosphorescence rate can be expressed by

$$k_r = const \cdot E_{T_1}^3 \sum_n \left| \frac{\left\langle \Phi_{S_n} \left| \hat{H}_{SO} \right| \Phi_{T_1} \right\rangle}{E_{T_1} - E_{S_n}} \cdot \left\langle \Phi_{S_0} \left| e\mathbf{r} \right| \Phi_{S_n} \right\rangle \right|^2. \tag{2.16}$$

Therefore, the magnitude of the phosphorescence radiative rate depends on three factors: The spin-orbit matrix element $\left\langle \Phi_{S_n} \left| \hat{H}_{SO} \right| \Phi_{T_1} \right\rangle$, the energy gap between S_n and T_1 and the transition dipole moment of the perturbing singlet states.

The SOC Hamiltonian H_{SO} describes the coupling between the spin and orbital momenta of an electron i. It is given by

$$H_{SO} = \frac{e^2}{2m_e^2 c^2} \sum_k \sum_i \frac{Z_k}{r_{ik}^3} \mathbf{l}_i \mathbf{s}_i, \tag{2.17}$$

where m_e is the electron mass, Z_k is the nuclear charge of the nucleus k, $\mathbf{l}_i$ and $\mathbf{s}_i$ are the orbital and spin momenta of an electron i [69, 70, 71]. r_{ik} represents the distance between electron i and nucleus k. The expectation value of r^{-3} for hydrogenic orbitals is proportional to Z^3. Thus, the overall SOC Hamiltonian is proportional to Z^4 and therefore much stronger in compounds containing a heavy metal atom. For such molecules the contribution of the heavy metal atom nucleus is predominant and the contribution to H_{SO} of the other nuclei with smaller nuclear charge can be neglected. The materials used in this work typically contain iridium atoms, which lead, due to their high atomic number of 77, to a pronounced and effective SOC and thus strong phosphorescence.

As already discussed above, in organometallic complexes a large number of excited states exist in a small energetic range. In principle, all of them can contribute to the ra-

diative rate of phosphorescence via SOC. However, many of these SOC matrix elements contribute sparsely and can be neglected. It is expected that singlet states which are close in energy to the lowest emitting triplet state will contribute most. There is still an ongoing discussion about the most effective SOC routes in organometallic compounds, in terms of the magnitude of the spin-orbit matrix elements. From experiments it is known that for many complexes the lowest triplet state is ligand-centered [64]. To
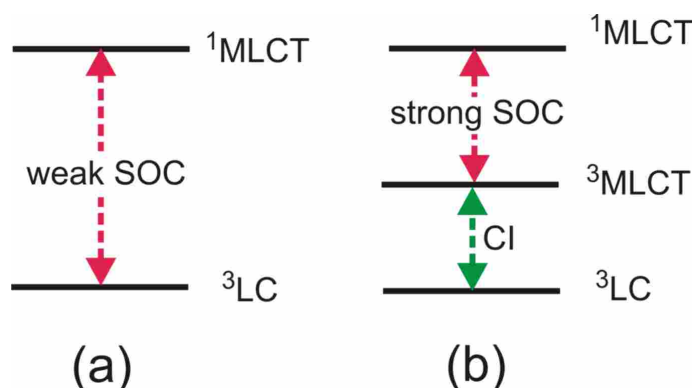
Figure 2.12: *Spin-orbit coupling (SOC) between different excited states. (a) Coupling between ³LC and ¹MLCT involves only two-center integrals and is weak. (b) SOC between ³MLCT and ¹MLCT involves one-center integrals and is typically efficient. ³LC couples to ³MLCT by configuration interaction (CI) [68].*

interpret the effect of SOC in such complexes, Komada et al proposed a mechanism, where the increase of the radiative rate is ascribed to a direct SOC between ¹MLCT and ³LC states (figure 2.12 (a)) [72]. However, this mechanism involves only two-center integrals on the metal. Thus SOC between these two states is expected to be small and therefore can not be responsible for the large effects of SOC found in organometallic complexes [68].

Another mechanism was proposed by Miki et al., where ¹MLCT states interact effectively by one-center SOC with ³MLCT states, which couples with ³LC states by configuration interaction (CI) (CI results from electron-electron interaction) (figure 2.12 (b))[73, 74]. According to the investigations of Obara et al., this indirect interaction is the dominant SOC route for many complexes [68]. In an alternative interpretation, using molecular orbital theory, the spin-orbit matrix element increases with the increase of the d metal orbital´s participation in the transition, implying an enhanced MLCT character in the lowest triplet state [34, 63].

As illustrated in equation (2.16) the energy gap between the perturbing singlet states S_n and T_1 is an important parameter influencing the radiative rate. Assuming that the

intense phosphorescence in organometallic complexes originates mainly from mixing between S_1 and T_1, one can neglect the influence of higher lying singlet states. In this case, the phosphorescence radiative rate is largely determined by the exchange energy between the first excited singlet and triplet states ($\Delta E_{ST} = E_{S_1} - E_{T_1}$). While purely organic molecules typically exhibit a value of ΔE_{ST} in the range of about $0.8\,\mathrm{eV}$, for organometallic complexes values between $0.3\,\mathrm{eV}$ and $0.7\,\mathrm{eV}$ have been reported [64]. As mentioned above, ΔE_{ST} reflects the amount of the MLCT character of the corresponding wave functions. This means that by increasing the participation of d-orbitals in the lowest triplet state, the delocalization of the electronic wave functions is increased. This leads to a larger spatial separation between interacting electrons compared to pure ligand-centered transitions. This then leads to a reduction of the electron-electron repulsion and the exchange interaction, which is proportional to ΔE_{ST}. While ΔE_{ST} is important for obtaining high radiative rates, there are no systematic studies correlating these two molecular properties for a set of organometallic complexes.

As mentioned above, ISC rates are high for organometallic complexes and the timescales for this process are in the ps to fs regime exceeding the one of the fluorescence decay ($\approx 1\,\mathrm{ns}$) [60, 75, 76, 77, 78]. Therefore, nearly all excitations are transferred before they can emit light from the singlet state. For example, Ir(ppy)$_3$, which has a very high MLCT character in the emissive triplet state, exhibits an ISC time of about $50\,\mathrm{fs}$ [78]. For compounds with a lower MLCT contribution, such as Pd(thpy)$_2$, ISC times are more than one order of magnitude slower ($\approx 1\mathrm{ps}$) [64].

One must consider that in this section we treated the triplet state as one single state. Due to spin statistics and magnetic dipole-dipole-interactions each triplet state splits up into three substates. Because of the low energetic separation of the three substates, we deal with a system of three equilibrated states at sufficiently high temperature and for example a simple expression can be used for the average decay of the triplet state. In the next section we will address this aspect in detail.

2.2.3 Zero-field splitting of the triplet state

Triplet states are formed by the coupling of two spin 1/2 particles, e.g. an electron and a hole, which have a total spin quantum number of $S = 1$ (in contrast to singlet states, where $S = 0$). Thus, three different possibilities for the spin magnetic quantum number m_S arise for the triplet state, resulting in three components (m_S=1, 0, -1),

which differ mainly by their relative spin orientations. The three components of the triplet are defined as $T_{III} = \alpha_1\alpha_2$, $T_I = \beta_1\beta_2$ and $T_{II} = \alpha_1\beta_2 + \alpha_2\beta_1$ for m_s=1,-1 and 0, respectively. The singlet component is given by $S = \alpha_1\beta_2 - \alpha_2\beta_1$. α and β represent the spin functions of the respective electrons, where α stands for a spin-up vector and β for a spin-down vector [38].

In the presence of anisotropic interactions the sublevels of the triplet state split up resulting in an energetic separation of these states, termed zero-field splitting (ZFS) (figure 2.13). The magnitude of the ZFS is determined by internal magnetic interactions, spin-spin-interaction (SSI) and SOC. It is practically impossible to experimentally distinguish the contribution of SSI and SOC to the ZFS. The energy of the sublevels shifts ΔE_i due to SOC can be expressed by [79]

$$\Delta E_{1(i)} = \sum_n \frac{\left|\left\langle \Phi_{S_n} \left| \hat{H}_{SO} \right| \Phi_{T_{1(i)}} \right\rangle\right|^2}{E_{T_{1(i)}} - E_{S_n}}, \tag{2.18}$$

where $T_{1(i)}$ are substates of the first excited triplet state with $i = \mathrm{I}, \mathrm{II}, \mathrm{III}$ and $E_{T_{1(i)}}$ are their corresponding energies. According to equation 2.18, strong SOC in the molecule should induce a large ZFS. Indeed, it has been demonstrated that organometallic complexes, which have a strong SOC, show a much higher ZFS than purely organic molecules. Yersin et al. reported for a series of phosphorescent molecules values of ZFSs ranging from $0.1\,\mathrm{cm}^{-1}$ to $211\,\mathrm{cm}^{-1}$, while for purely organic molecules values below $1\,\mathrm{cm}^{-1}$ have been reported [22, 63, 64, 80]. Therefore, we conclude that in organometallic complexes the amount of ZFS is mainly determined by SOC.

Due to SOC anisotropy, the photophysical properties of the individual substates,
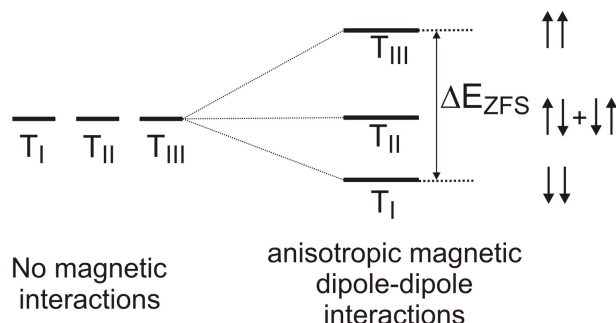
Figure 2.13: *The effect of anisotropic magnetic dipole-dipole interaction on the triplet substates T_I, T_{II} and T_{III}. In the absence of an external magnetic field the interaction results in a zero-field splitting (ZFS) of the sublevels. On the right side the spin vector representation of the triplet substates is shown.*
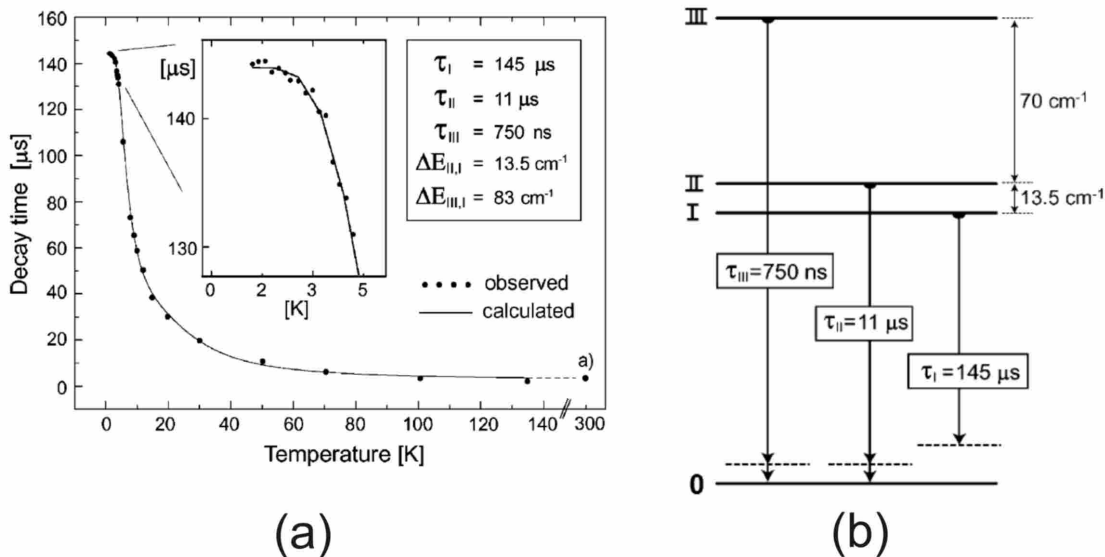
Figure 2.14: (a) Emission decay time of Ir(ppy)$_3$ dissolved in tetrahydrofuran versus temperature. From a fit of the decay curve, one obtains the decay times of the individual substates (τ_I, τ_{II}, τ_{III}) and the energy differences between the respective states ($E_{II,I}$ $E_{III,I}$). (b) Associated energy level diagram. Adapted from reference [80].

e.g. radiative decay rates, occupation probabilities and relaxation dynamics, can differ dramatically leading to a non-equilibrium occupation of substates. However, fast spin-lattice relaxation (SLR) between the substates typically compensates the occupation imbalance at high temperatures. Therefore, at room temperature the individual features smear out and one observes only an averaged behavior of the substates. At a temperature below 5 K the SLR rate can decrease dramatically leading to a non-equilibrium occupation of substates. Therefore, a direct study of their individual properties is possible. Besides, for molecules with a high ZFS only the lowest substate is occupied at low temperatures, allowing a direct observation of the photophysical properties of this state. [80]. For example, Ir(ppy)$_3$ shows an emission decay of 2 μs at room temperature. By cooling down to cryogenic temperatures the emission decay time increases to 145 μs at T = 1.2 K, which stems form the energetically lowest triplet substate (figure 2.14 (a)). Under assumption of fast thermalization the decay times of the other substates and the energy difference between the substates can be extracted from temperature dependent measurements (inset). The effectiveness of SOC to the individual substates can differ dramatically from each other, which is reflected in the different emission decay times (figure 2.14 (b)).

In this work we investigate the ZFS of single organometallic complexes. With these

studies it is possible to reveal that the ZFS is not a static quantity and fluctuates in time for single emitters. We conclude that this fluctuation is caused by temporal variations of the effectiveness of SOC, probably as a consequence of small changes in the molecular structure induced by the environment or the excited state.

2.3 Transport processes in amorphous organic films

A solid state body consisting of π-conjugated materials is typically a collection of disordered organic molecules or polymers. Ordered molecular assemblies can only be formed with small molecules in special cases such as in molecular crystals. The great advantage of amorphous films is their simple fabrication (section 3.2). However, the properties of these films differ significantly from those of crystalline inorganic semiconductors. In particular, because of the weak van der Waals forces in organic semiconductors, the intermolecular coupling is weak, resulting in low mobilities of charge carriers. A detailed understanding of the disorder on the mobility of charge carriers and excitons is necessary for a systematic design of molecules and thin films, which are used for OLEDs. In the following chapter we will address transport processes in amorphous organic films.

2.3.1 Charge carrier transport

Because of the large energy gap and the low concentration of charge carriers, π-conjugated organic molecules become conductors when an external voltage is applied and excess charge carriers are injected. However, similar to inorganic semiconductors, the conductivity of a solid state body consisting of organic semiconductors can be increased enormously by inserting dopant molecules and it can become conductive already at moderate temperatures [22].

Before we present a microscopic model for charge carrier transport in amorphous films, the energetic distribution of the transport levels in organic semiconductors will be outlined. Considering transport of charge carriers in organic molecular solids, one has to keep in mind that this involves ionic molecular states. E.g. electron transport involves negatively charged radical ions. Furthermore, an additional charge on a molecule leads, due to an interaction between electrons and nuclei, to a deformation of the molecular geometry. Thereby, the charged molecule polarizes the molecules in its
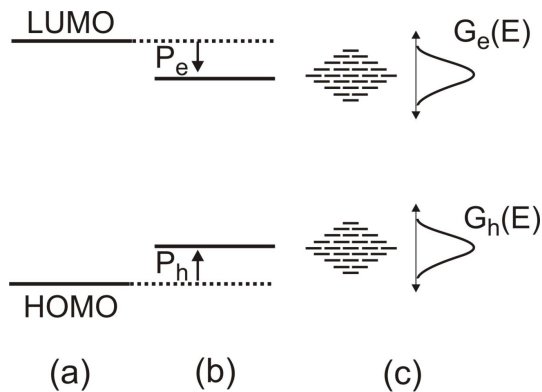
Figure 2.15: *(a) HOMO and LUMO level of a neutral isolated molecule. (b) An additional charge, electron or hole, on the molecule causes a polarization of the environment. P_e and P_h are the polarization energies of electrons and holes, leading to a renormalization of the energy levels of the charged molecule, which lie in between the HOMO and LUMO. (c) The energy levels underlie a static distribution and can be described by a Gaussian shaped density of states (DOS) [22].*

environment. The time scale for this process is very fast and the electronic polarization follows the movement of the charge almost instantaneously. Such a quasiparticle consisting of a charge dressed by its own polarization field is called a polaron. Overall, the transport gap is lowered compared to the one of the unperturbed, neutral molecule (figure 2.15 (a)-(b)) [81, 82, 83].

Because of the static allocation of molecules in an amorphous layer, each molecule has its specific dielectric environment, resulting in an energetic disorder of electronic states. In addition, molecules can differ in their conjugation length due to structural defects or bending. The distribution of the energy levels of the excited states are described by a Gaussian shaped density of states (DOS), whose width is a measure of the disorder in the system (figure 2.15 (c)). Charge carrier transport in amorphous layers takes place by a hopping process of charges from molecule to molecule [22]. Thus, charge carrier mobility is by some orders of magnitude smaller than in inorganic semiconductors [22].

An established microscopic model of the hopping transport in disordered organic films was given by Bässler et al. [84]. This model is mainly based on two assumptions. First, as mentioned above, the distribution of the excited energy levels can be described by a Gaussian shaped DOS. The second assumption refers to the hopping rate ν_{ij} between two molecules i and j. The rate is expressed by

$$\nu_{ij} = \nu_0 \exp(-2\gamma\Delta R_{ij}) \begin{cases} \exp(-\frac{E_j - E_i - eF(x_j - x_i)}{kT}) & \text{if } E_j > E_i \\ 1 & \text{if } E_i \geq E_j \end{cases} \tag{2.19}$$
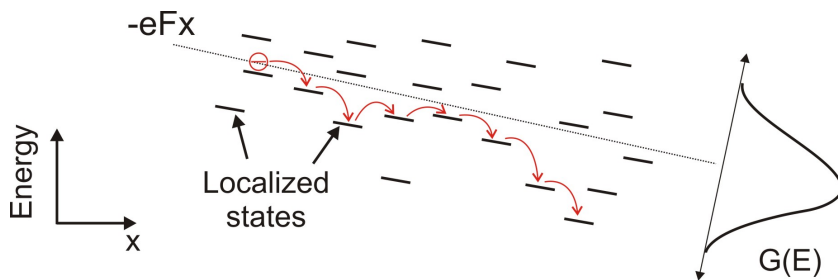
Figure 2.16: *Schematic diagram of the hopping transport in disordered organic semiconductors along an electric field F. The hopping process can occur either to neighbor molecules with lower or with higher energy. The energy distribution of states is assumed to be a Gaussian distribution function G(E). Adapted from [22].*

where E_i and E_j are the energies of the transport states, ν_0 is a prefactor, F is the external applied electric field, γ is the constant of the exponential decreasing wave function and ΔR_{ij} the norm of the distance of involved molecules. If $E_i \geq E_j$, the second term is equal to 1, meaning that no activation energy is necessary for hopping from an energetically higher state to a lower one. The model of Bässler cannot be solved analytically. However, Monte-Carlo simulations of the charge transport in an idealized sample have shown a good agreement with experimental results [84]. Figure 2.16 shows the hopping transport of a single polaron in an amorphous organic semiconductor along an electric field F. In this example an electron moves in a Gaussian distribution of LUMO levels. The mobility μ of a charge carrier in dependence of an electric field can be written in following way

$$\mu(F) = \mu_0 \exp(\beta\sqrt{F}), \tag{2.20}$$

where μ_0 is the mobility in the absence of an electric field and β is the field amplification factor [22, 85].

In organic semiconductors charges are usually provided by an external circuit, meaning that they are injected from metallic contact layers. The interface between the metal and the organic layer plays an important role for the description of the charge transport inside the organic layer. If a contact does not provide enough charge carriers and therefore limits the current inside the organic layer, one speaks of an injection-limited current. In contrast, in the presence of Ohmic contact layers the current is limited by the organic semiconductor itself (space-charge-limited current). In this case, by increasing the applied voltage more and more excess charge carriers are injected. As soon as their density becomes too large, a space charge is built, which determines the current to a large extent. In the presence of a space-charge current, a relationship be-

tween the current density, the mobility and the applied electric field can be established. Under the assumption of a constant mobility without trapping states, one finds for the dependence of the current density following relation

$$j = \frac{9}{8}\epsilon\epsilon_0\mu\frac{V^2}{d^3},$$ (2.21)

where d is the thickness of the organic layer and V the applied voltage. This is the so-called Child´s law [86]. This situation is found only in special cases and does not reflect the experimental conditions observed most frequently. Only in a few cases is an organic semiconductor free of charge-carrier traps and energetically distributed trapping states are present [22]. In this case, the dependence of the voltage on the current density becomes much more complicated to describe.

2.3.2 Energy transfer in host/guest systems

Like charge carriers, neutral excitations (excitons) can hop from one molecule to another which is in close proximity to the first. Thereby, the energy transfer can take place from a donor to an acceptor molecule or as in the case of polymers inside of a DOS of energetic states of the same polymer [87]. In the first case the energy transfer takes place in a combined system between a donor (host) and an acceptor molecule (emitter). This directed energy transfer plays an important role in OLEDs, because here the emitter molecules are typically doped into a host material in order to avoid aggregation and thus a reduction of their efficiency [88, 89]. An efficient energy transfer of excitons is even possible at low concentrations of acceptor molecules, provided that the exciton diffusion is large enough [90]. Excitons not only migrate to emitter molecules, but also to low-energetic defects or trap states, which can cause a strong luminescence quenching. This point is crucial for the development of OLEDs, where such defects must be avoided [91, 92, 93].

Radiationless energy transfer of excitons can occur via a Förster or Dexter mechanism. In the Förster model the energy transfer is described by a dipole-dipole interaction between a donor D and an acceptor A [94, 95]. The corresponding transfer rate $k_{Forster}$ is expressed by

$$k_{Forster} = \frac{1}{\tau_D}\left(\frac{R_0}{r_{DA}}\right)^6,$$ (2.22)

where R_0 is the Förster radius

$$R_0 = \frac{3c^2}{4\pi n^2} \int_0^\infty \frac{f_D(\omega)\sigma_A(\omega)}{\omega^4} d\omega. \tag{2.23}$$

r_{DA} is the distance between the donor and the acceptor, τ_D the radiative lifetime of the donor state, $f_D(\omega)$ the normalized emission spectrum of the donor and $\sigma_A(\omega)$ denotes the absorption cross section spectrum of the acceptor. The transfer rate (equation 2.22) has a strong dependence on the distance between the involved molecules ($k_{Forster} \propto (r_{DA})^{-6}$). If a sufficient overlap between the absorption spectrum of the acceptor and the emission spectrum of the donor, and a small value of r_{DA} compared to R_0 is provided, an efficient energy transfer is obtained [37]. R_0 typically has values between 5 and 10 nm.

Dexter energy transfer occurs as a result of an electron exchange interaction [96]. The energy transfer requires an overlap of the wave functions of the donor and the acceptor and therefore, is observable only for small distances between donor and acceptor (smaller than 1.5 nm) [37]. The transfer rate k_{Dexter} is given by [97]

$$k_{Dexter} \approx J \exp\left(\frac{-2r_{DA}}{L}\right), \tag{2.24}$$

where J is the spectral overlap integral between the normalized donor emission and acceptor absorption spectra and L the typical penetration depth of the wave function into the environment.

Until now we have not considered the spin of the involved neutral excitations. For both mechanisms spin conservation rules have to be fulfilled. For the Förster mechanism the spin of the individual components has to be conserved, whereas for the Dexter mechanism the combined spin of the participating molecules has to be conserved during energy transfer [94, 95, 97]. In the latter case, energy transfer can follow:

$$^3D^* + {}^1A \rightarrow {}^1D + {}^3A^* \text{ or}$$
$$^1D^* + {}^1A \rightarrow {}^1D + {}^1A^*.$$
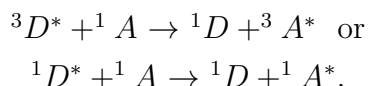
The star denotes the excited state and the index 3 and 1 refers to a triplet or singlet exciton, respectively. Hence, singlet-singlet and triplet-triplet energy transfer are allowed via the Dexter mechanism, (figure 2.17 (a)). The Förster mechanism promotes in principle only singlet-singlet energy transfer (figure 2.17 (b))
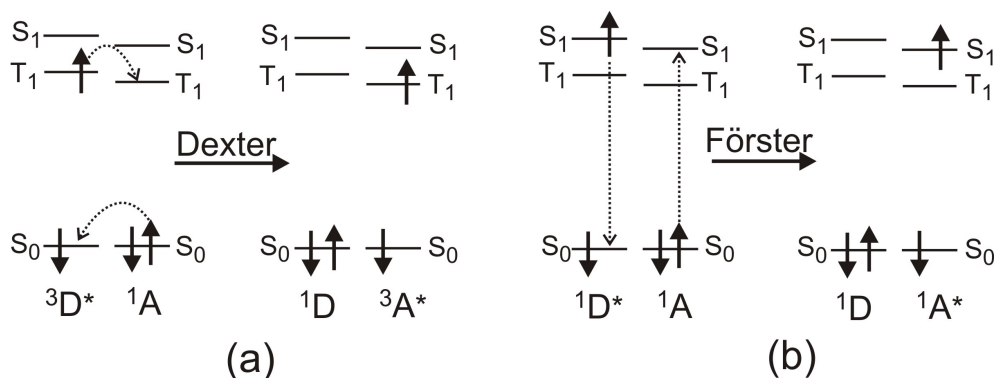
Figure 2.17: *(a) Since in the Dexter mechanism only the combined spin of the participating molecules has to be conserved, energy transfer from the triplet state of the donor $^3D^*$ to the triplet state of the acceptor ^3A is possible. Note, the star indicates that the molecule is in an excited state. (b) The Förster mechanism typically only allows energy transfer from the first excited singlet state S_1 of a donor $^1D^*$ to the corresponding state of an acceptor ^1A.*
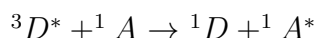
$$^1D^* +^1 A \rightarrow {}^1D +^1 A^*.$$
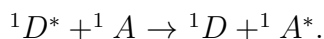
However, in the presence of strong SOC, Förster energy transfer from the triple state of the donor to the singlet state of the acceptor

$$^3D^* +^1 A \rightarrow {}^1D +^1 A^*$$

is also observable [98]. Especially for the organometallic molecules studied in this work this process can be efficient.

As we will discuss in the following chapter, transport processes of charge carriers and of excitons play a significant role in OLEDs. Before an exciton is generated inside the device, polarons with an opposite electronic charge have to move through amorphous organic films and energy transfer to the emitting triplet state has to take place.

2.4 Phosphorescent organic light-emitting diodes

After describing the basic physical properties of organic molecules and amorphous layers, we will present the working principle of OLEDs in this section. There are two different classes of OLEDs, which have to be distinguished: OLEDs which employ small molecules as organic materials and polymer-based OLEDs. In the first case the organic materials are deposited by thermal vacuum evaporation, offering the possibility to produce layers in a controlled manner and the fabrication of so-called multilayer OLEDs with a sequence of deposition of different layers.

In this section we will first give an overview over the working principle and the detailed device setup of an OLED. Then we will focus on phosphorescent OLEDs. By using phosphorescent small molecules as emitters, the efficiency can be increased reaching values comparable to fluorescent tubes [99]. Additionally, efficiency and loss-mechanisms in such devices, which are quite pronounced due to the relatively long lifetime of the excited state, will be discussed.

2.4.1 Device structure and working principle

In the easiest OLED structure, the organic light-emitting layer is sandwiched between two contact layers, the cathode and the anode. For the latter, transparent conductive indium tin oxide (ITO) and for the cathode aluminum are employed as electrodes. The emission layer has a thickness ranging from 10 - 100 nm [97]. The basic mechanism of electroluminescence involves (1) charge carrier injection via the electrodes, (2) drift of charge carriers towards the opposite electrode in an electric field, (3) formation of bound electron-hole pairs (excitons) in the organic layer and (4) radiative recombination of these pairs (figure 2.18). The light is emitted through the semitransparent anode. We will now describe the four processes in more detail.
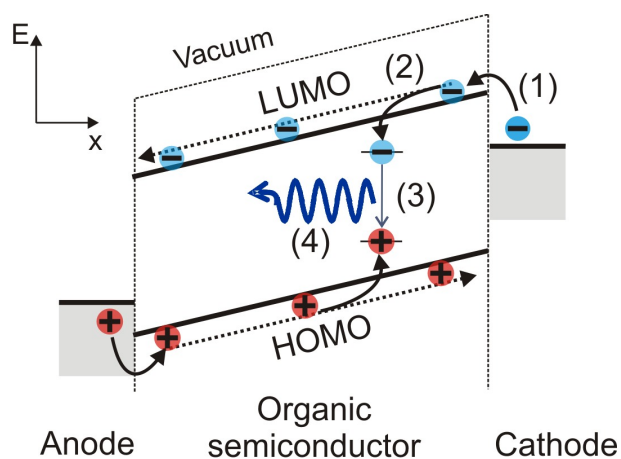
Figure 2.18: *Energy diagram and charge carrier processes of an OLED consisting of a single organic layer and electrodes. The basic mechanism of electroluminescence involves four steps: (1) Charge carrier injection via the electrodes (2) drift of charge carriers towards the opposite electrode in the presence of an electric field, (3) formation of electron-hole pairs (excitons) in the organic layer and (4) radiative recombination of these pairs.*

1. The exact description of the injection of charge carriers into the organic layer is complex and a microscopic description is necessary [100]. In order to enter

the organic layer, charges have to overcome a potential (barrier), which is given by the difference between the work function of the metal and the LUMO of the organic layer for electrons and the HOMO for holes. Note, holes are injected from the anode and electrons from the cathode. The injection is typically described by a tunnel process or by thermal injection [22]. In the first case, charge carriers have to tunnel through the barrier, while in the second case they overcome it by thermal activation. For small barrier heights and for small electric fields thermally activated injection is the dominant process, while in the opposite case, tunnel processes contribute the most. For a detailed description of charge carrier injection one has to take into account the formation of dipoles at the metal-organic interface, which causes modifications in the vacuum level at this interface [101]. If the electrode delivers enough charge carriers to the organic layer, then the current in the organic layer enters the space charge limited regime (section 2.3.1).

2. After injection, the charge carriers drift under the presence of the external voltage towards each other. Holes move towards the cathode and electrons towards the anode. Due to the different mobilities of electrons and holes, the charge carriers often do not meet in the middle of the emission layer, but at the interface of the metal and the organic layer.

3. When electrons and holes are on adjacent molecules, they attract each other because of the Coulomb potential and form excitons (section 2.1.2). To ensure an efficient recombination, the same amount of electrons and holes has to be present in the recombination zone. Otherwise charge carriers can move through the organic layer to the contact layer without forming excitons. According to simple spin statistics, the fraction of singlet and triplet excitons is predicted to be 1 to 3. With the use of a fluorescent emitter, triplet excitons do not emit light, leading to an inherent efficiency limitation in OLEDs, since triplet excitons recombine via non-radiative channels. Therefore, a maximum of 25 % of the energy can be converted to light [102]. In contrast, a phosphorescent emitter can harvest both singlet and triplet excitons and convert them to light leading to a high electroluminescence efficiency [12, 103].

4. The last step is the recombination of excitons with emission of luminescence. Fluorescent emitters have a radiative decay lifetime in the ps - ns range. In comparison, phosphorescent emitter lifetimes are in the μs range. Due to this long

lifetime, radiationless deactivation of excitons can be pronounced in phosphorescent OLEDs. Especially at high driving conditions quenching processes such as triplet-triplet-annihilation and triplet-polaron quenching are typically present. A key issue for the design of phosphorescent OLEDs is to employ emitters with enhanced radiative decay rates, so that the triplet excitons can decay radiatively before coming into contact with other excitons and/or a polarons. The emission wavelength is determined by the optical energy gap of the emitter material, which can be tuned according to its chemical structure.

While the structure presented above is capable of generating electroluminescence, it is not a state-of-the-art device. These require more complex architecture structures. To ensure that exciton recombination takes place within the emitting layer (EML), multiple layers with optimized transport characteristics have to be added (figure 2.19). The recombination zone is typically sandwiched between an electron (ETL) and hole transporting layer (HTL) and sometimes a hole blocking layer (HBL) with adapted HOMO and LUMO levels. ETL and HTL are used to obtain optimized transport from the contacts to the recombination zone and also to minimize the leakage of holes to the cathode and electrons to the anode. An important issue which has not been discussed so far is that the layers in the vicinity of the EML must contain materials with triplet levels high enough to prevent triplet exciton transfer out of the recombination zone. While this is typically the case for the HTL, it may not be the case for the ETL. To prevent energy transfer from the recombination zone to the ETL sometimes an HBL is sandwiched between the EML and the ETL. Indeed, it has been shown that a added blocking layer can significantly improved the device performance [103, 104]. The HOMO and LUMO of all layers must match each other in a suitable way, to facilitate the injection of electrons and holes into the EML.

The structure shown in figure 2.19 is an example of a state-of-the-art blue-emitting phosphorescent OLED. Focusing on the EML we note that in order to prevent aggregation of the emitter molecules and so a reduction of the device efficiency, the EML is composed of a conducting host material in which the emitter is doped at low concentrations (below 15 %). The host material has to fulfill following criteria: the lowest triplet level has to exceed the lowest emitter triplet level to ensure energy transfer of excitons from the host to the emitter; and the HOMO and LUMO levels have to match the ones of the emitter in a suitable way. In the structure shown in figure 2.19 the emitter material $Ir(cnpmbic)_3$ was doped at a low concentration of 10 % in the host material iridium
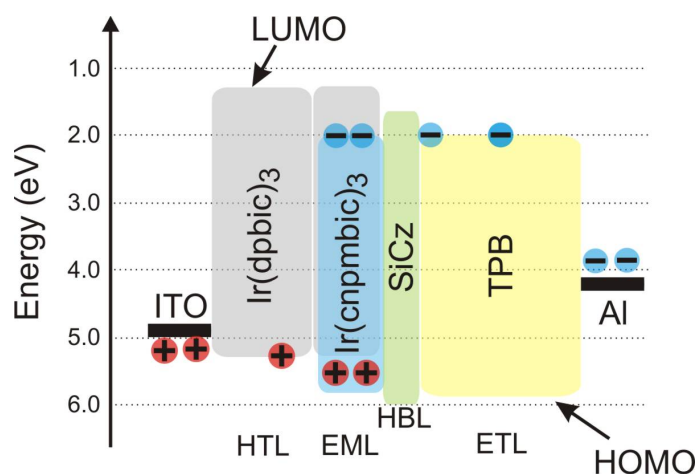
Figure 2.19: *Structure and schematic energy diagram of an efficient, phosphorescent multilayer OLED. With a suitable choice of an electron and a hole transporting layer (ETL, HTL, respectively), recombination takes place within the emitting layer (EML), consisting of the emitter Ir(cnpmbic)₃ doped into the host material Ir(dpbic)₃ at a concentration of 10 %. A hole blocking layer is typically used to prevent exciton migration out of the EML. The ETL consists of TPB, the HBL of SiCz and the HTL of Ir(dpbic)₃. The device structure was prepared by molecular beam deposition.*

tris(1-phenyl-3-phenylbenzimidazolin-2-yilidene-C,C$^{2'}$) (Ir(dpbic)$_3$), which is also used as an HTL. The ETL consists of N,N´-bis(3methylphenyl)-N,N´-bis(phenyl)-benzidine (TPD) and the HBL of 9-(4-tertbutylphenyl)-3,6-bis(triphenylsilyl)-9H-carbazole (SiCz). The wavelength of the emitted light can be tuned by modifying the chemical structure of the emitter molecule, in this case of the organometallic complex. Because of the big variety of such complexes, efficient OLEDs for the green and red wavelength region has been produced [105, 106, 107]. However, blue-emitting organometallic complexes for OLEDs are still difficult to develop because of the intrinsic instability or low quantum efficiencies of such molecules.

The HOMO and LUMO levels of the materials shown in figure 2.19 and of the one used in this work were determined via density functional calculations. For the HOMO and LUMO first the geometry of the neutral as well as the charged states were optimized using the BP86-functional [108, 109], in combination with a split-valence basis set including polarization functions on all heavy atoms [110]. To account for dielectric solid state effects an ultraviolet photoelectron spectroscopy/inverse electron photoemission spectroscopy UPS/IEPS calibrated version of the conductor like screening model was used in conjunction with the single point calculations [111]. All calculations were carried out with the turbomole program package [112]. These data were compared with cyclic voltammetry curves and UPS showing a reasonable agreement, with a variance below 0.3 eV.

To date, white light OLEDs with long operational lifetimes have been obtained mainly with a combination of a blue fluorescent emitter and phosphors for the other colors [113]. Such an elegant approach relies on an efficient harvesting of singlet and triplet excitons and requires, therefore, a precise deposition of the emitter molecules in the transporting hosts. In contrast, efficient white light OLEDs based on blue phosphors can be obtained with all the emitters in one single layer, simplifying the processing [114]. However, blue phosphors have so far proven to be rather unstable. While a physical explanation for blue phosphor based device instability is still lacking, a shorter phosphorescence lifetime, eventually approaching the sub-microsecond time regime, would decrease the residence time of potentially unstable excited states. Therefore, one important question of this work was, how the phosphorescence lifetime can be reduced while maintaining high quantum efficiency. In chapters 4 and 5 we will analyze parameters which control the radiative rate in phosphorescent organometallic complexes emitting in the deep-blue by looking at the ΔE_{ST} and the SOC via the ZFS.

The challenges in producing blue phosphorescent OLEDs can be summarized as follows: finding suitable deep-blue phosphors with short phosphorescence lifetimes and high efficiencies [34, 115, 116]; development of host materials with good charge transport properties, maintaining high triplet levels for triplet exciton confinement [61, 117]; HOMO and LUMO levels of the host material matching the ones of the adjacent charge transporting layers for optimal hole and electron injection, respectively.

2.4.2 Efficiency and loss processes

As future light sources, OLEDs have to fulfill high standards in terms of efficiency. In the last decade the efficiency could already be increased considerably by the use of multilayer structures and organometallic complexes as emitters [10, 12]. However, quenching mechanisms like triplet-triplet annihilation (TTA), triplet-polaron annihilation (TPA) and electric field induced quenching can be severe in phosphorescent OLEDs and reduce their overall efficiency at high brightness. Before we will discuss these different loss processes in more detail, a description of OLED efficiency is presented.

Efficiency

The external efficiency of an OLED, η_{ext}, is defined as the ratio of the number of emitted photons M to the number of injected electrons:

$$\eta_{ext} = \frac{M}{j \cdot U}, \tag{2.25}$$

where j is the current density and U the applied voltage. M is expressed by ϕ/A, where A is the emitting area and ϕ the luminosity. The unit of M is lm (lumen) and of η_{ext} lm/W.

The external quantum efficiency can be written as

$$\eta_{ext} = \eta_{out}\eta_{int}, \tag{2.26}$$

where η_{int} defines the internal quantum efficiency of the emissive molecule and η_{out} the output coupling fraction of the device [118]. η_{out} is limited by losses occurring mainly due to total reflection and re-absorption of the emitted light. Such loss channels are pronounced in OLEDs due to refractive index mismatches of the corresponding organic materials and internal reflections. Therefore, η_{out} is typically limited to 20 % [12]. During the last years extensive work has been performed to develop structures with an increased light-output coupling efficiency. In a recent publication Sun and co-workers demonstrated an enhancement of η_{out} of about 2.3 times over that using conventional flat glass substrates [119]. In another publication by Reineke et al. increased output coupling efficiencies were used to demonstrate OLED efficiencies comparable to those of Neon tubes [99].

While technologically relevant, the output coupling efficiency does not depend on the materials used in the OLED. However, the molecules have an influence on the internal quantum efficiency, which is defined as the ratio between the number of generated photons and the number of injected electrons. The internal quantum efficiency can be described by

$$\eta_{int} = \eta_{PL}\eta_{r}\chi. \tag{2.27}$$

η_{PL} is the luminescence efficiency of the emissive molecule, χ describes the portion of excitons formed per injected charge carrier in the diode and η_{r} the portion of emissive excitons, reflecting the ratio of singlet and triplet exciton formation. For a fluorescent molecule η_{r} is 25 % due to spin statistics, since 75 % of the generated excitons are
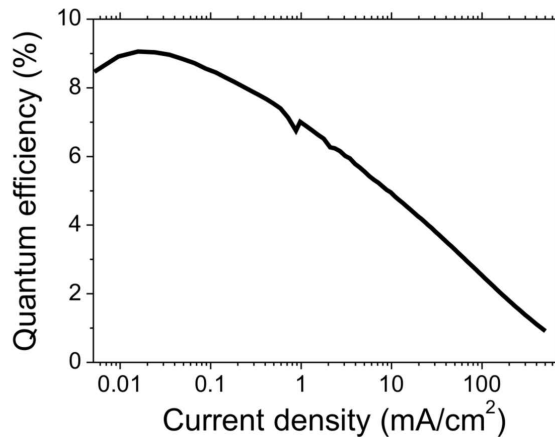
Figure 2.20: *Quantum efficiency of the device setup shown in figure 2.19 as a function of the current density. At higher current density loss channels become crucial, resulting in a reduction of the quantum efficiency.*

triplets. For a phosphorescence emitter η_r reaches $100\,\%$, since both singlet and triplet excitons are harvested [12]. Therefore, the use of organometallic complexes as emitters for OLEDs increases the internal quantum efficiency by a factor of four.

Although internal quantum efficiencies above $90\,\%$ can be reached with phosphorescent emitters, different loss channels, such as TTA, TPA and electric field induced quenching, limit η_{int}. It has been proposed and demonstrated that TTA and TPA are in particular pronounced in phosphorescent OLEDs because of the long lifetime of triplet excitons (μs - ms), leading to a reduction of the quantum efficiency especially at high current densities. But also electric field assisted dissociation of excitons can be present in an operating OLED and limit its efficiency [120]. In figure 2.20 the external quantum efficiency of the OLED shown in figure 2.19 as a function of the current density is plotted. The device exhibits an η_{ext} of up to $9\,\%$ at low current densities. However, the overall efficiency drops off considerably for current densities higher than the moderate value of $0.02\,\mathrm{mA/cm^2}$. This behaviour is usually called roll-off in literature. Currently the origin of the roll-off in efficiency is the subject of a scientific debate. In particular, it is not clear which one of the three phenomena mentioned above is mainly contributing. In the following we will discuss in detail the physical processes identified as possible origins for this decrease in efficiency.

Triplet-triplet annihilation

Triplet-triplet annihilation was first observed and described in phosphorescent OLEDs by Baldo et al. [61]. Their theoretical framework will be used as a basis in this work. In the following we will assume that only excitons on emitter molecules participate in TTA

and not those on the host. Due to the high phosphorescence lifetime, high densities
of triplet excitons can be reached during operation, leading to the annihilation of two
triplet excitons, according to following process:

$$T_1 + T_1 \Rightarrow S_0 + S_n \quad (\text{or } T_n) \tag{2.28}$$
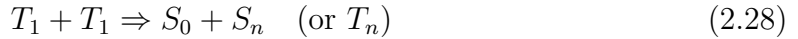
This process involves two excitons interacting, resulting in one molecule in the ground
state (S_0) and one in a higher excited state (S_n). This is an important process for
understanding quenching since two excitons with the potential to emit two photons are
converted into one, which can emit only one photon, after the fast relaxation from S_n to
S_1. The total energy of this process is conserved, i.e. $E_{T_1} + E_{T_1} = E_{S_n}$. Therefore, TTA
has a certain probability which depends on the energy resonance condition described
by the equation above. In organometallic molecules, because of the fast ISC, S_n is
rapidly converted to T_n and the final products of equation 2.28 can be $S_0 + T_n$.

Experimentally TTA can be observed as a quenching of phosphorescence in the early
times after photoexcitation. The time dependence of the triplet exciton concentration
$[T_1]$ at a time $t = 0$ after short-pulse optical excitation can be written as

$$\frac{d[T_1]}{dt} = -\frac{[T_1]}{\tau_T} - \frac{1}{2}k_{TTA}[T_1]^2. \tag{2.29}$$

τ_T is the decay lifetime of the first excited triplet state and k_{TTA} the rate constant for
TTA. Equation 2.29 can be solved to

$$L(t) = \frac{L(0)}{\left(1 + [T_1(0)](k_{TTA}\tau_T/2)\right)e^{t/\tau_T} - [T_1(0)](k_{TTA}\tau_T/2)}, \tag{2.30}$$

assuming that the luminescence intensity (L) is linearly proportional to the concentra-
tion of excited states $(L(t) \propto [T_1(t)]/\tau)$ [61].

Triplet-polaron quenching

Another quenching process is triplet-polaron annihilation. In this case, an exciton
transfers its excitation energy to a polaron with a non-radiative decay. This process
can be considered very similar to Auger recombination in inorganic semiconductors.
In order to investigate this quenching mechanism, experiments under continuous-wave
illumination I_{CW} and steady-state current flow were carried out. If we assume that

the rate of TPA is proportional to the average charge-carrier density $[n_{charge}]$, then this process follows:

$$\frac{d[T_1]}{dt} = -\frac{[T_1]}{\tau_T} - k_{TP}[T_1][n_{charge}] + I_{CW}, \qquad (2.31)$$

where k_{TP} is the rate constant for TPA [61].

The results of most publications illustrate that TTA and TPA are mainly responsible for the roll-off in quantum efficiency at increasing current densities for various phosphorescent OLEDs [61, 105]. In contrast, other groups have shown that the decrease of efficiency can be ascribed to an electric field assisted dissociation of excitons [45, 120, 121], which was discussed in section 2.1.2. For blue emitters, where operating voltages are higher than for green and red, such an effect appears to be significant.

Exciton dissociation by an external field in OLEDs

Dissociation of bound electron-hole pairs is a well-known process, and has been studied in the past mainly for pure films consisting of fluorescent molecules or polymers and for blend systems used in photovoltaics [48, 49, 122]. However, the effect of an electric field on triplet excitons and especially the impact of this quenching process for the roll-off in the external quantum efficiency of an OLED is still under controversial discussion in literature [105, 121].

Kalinwoski et al. demonstrated that the decrease in electrophosphorescence efficiency of an OLED at high electric fields stems from field assisted dissociation of PPs, which are precursors of the emitter excitons (section 2.1.2). It has also been concluded that TTA and TPA processes only play a role in the roll-off at low current densities [120]. Additionally, Holmes and co-workers showed that in their investigated device the roll-off in the external quantum efficiency is also due to the electric field induced dissociation of bound electron-hole pairs [121]. In contrast, Reineke et al. ruled out exciton dissociation by an external electric field in state-of-the-art phosphorescent OLEDs at low applied fields [105]. The argument proposed by Reineke is that the binding energy of triplet excitons in small molecules is too high for them to dissociate at typical OLED driving voltages. However, large local fields, which are significantly higher than the average applied field, can build up at interfaces in multilayer OLEDs and electric field induced quenching can become critical even for small external fields [123].

To shine light into this discussion we have investigated electric field induced quenching of the PL intensity of a deep-blue emitter in combination with several host mate-

rials. We will demonstrate in chapter 6 that electric field quenching of the phosphorescence depends on the concentration of emitter molecules in the EML and on the energy level alignment of the host/emitter combination.

Chapter 3

Materials, sample preparation and experimental methods

In this chapter first novel organometallic complexes with carbene ligands are introduced and their chemical structure and electronic transitions are described in detail. Additionally, we characterize a host material with particular attention to its triplet energy level. In the second part of this chapter we describe the sample preparation methods used in this work. The last part deals with different spectroscopic techniques.

3.1   Materials

In this work novel organometallic complexes with carbene ligands, which are the emitting molecules in blue phosphorescent OLEDs, have been investigated extensively. Moreover, we have characterized small molecules not necessarily containing a metal ion, which are used as hosts for emitter molecules. For the study of single molecules a red emitting organometallic complex was employed.

3.1.1   N-heterocyclic carbene complexes

Since the introduction of organometallic complexes as emitters in OLEDs, there have been big steps in their optimization in terms of phosphorescence efficiency. In the green and red spectral range phosphorescent OLEDs with high efficiency and stability have already been demonstrated [12, 103, 107]. Devices with the green emitting $Ir(ppy)_2acac$

have shown external quantum efficiencies of up to 19 % and sufficient device stability to reach application demands [64].

However, there is still lack of stable and efficient blue-emitting OLEDs, which are essential for the commercial launch of such devices for lighting. Lots of effort has been done to shift the emission wavelength of organometallic complexes to the deep-blue spectral range, while maintaining a high radiative rate and high photoluminescence efficiency. This is a particularly challenging task since shifting the lowest emitting triplet state can lead to the population of non-radiative states. The first attempt
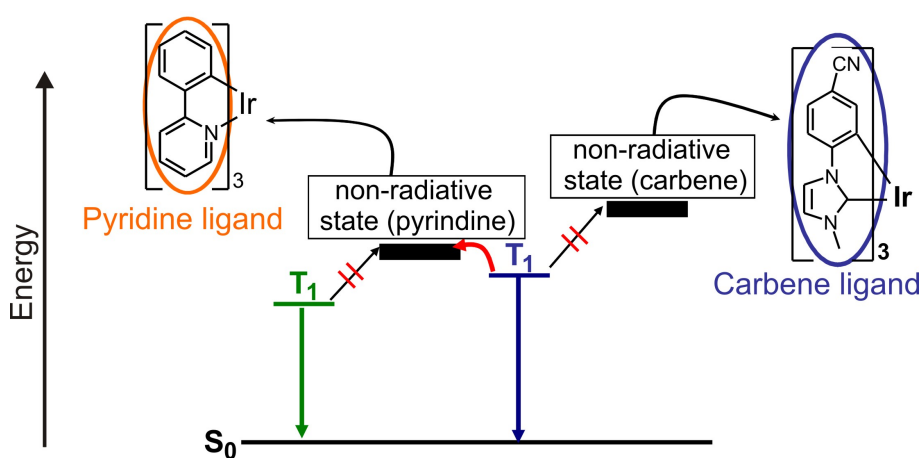

Figure 3.1: *Compared to complexes with pyridine ligands, at compounds with carbene ligands a non-radiative state (black line) can be shifted to higher energies. Therefore, even for blue-emitting molecules non-radiative states are not populated at room temperature and efficient blue phosphorescence is possible for complexes with carbene ligands.*

was carried out by modifying the ligand structure of molecules with pyridine ligands [124, 125, 126]. However, it turned out that this approach is not suitable to reach efficient deep-blue emission because of a significant decrease in luminescence efficiency due to a close non-radiative state (black level in the left side of figure 3.1). The origin of the non-radiative state are probably e_g-orbitals, which promote non-luminescent d-d^*-transitions (section 2.2.1) [127, 128]. Thus, organometallic complexes had to be designed in a way that the energy of such a non-radiative excited state is increased, inhibiting thermal population at room temperature. In 2003, N-heterocyclic carbene complexes were unveiled as a powerful new class of phosphorescent emitter materials [127, 129]. Such complexes show efficient phosphorescence at room temperature for emission energies exceeding 3 eV (413 nm). A key feature of these molecules is their strong metal-ligand bonds, suggesting that the cyclometalated carbenes are stronger field ligands than their pyridyl counterparts. This enables both triplets emitting at

high energies (deep-blue part of the spectrum) and a high-energy non-radiative state, as shown in figure 3.1.

Accordingly, this new class of emitters provides an unmatched potential for reaching the desired deep-blue color space with phosphorescent OLEDs. As an example, figure 3.2 shows the absorption and phosphorescence spectrum of the complex iridium tris(1-cyanophenyl-3-methylbenzimidazolin-2-yilidene-C,C$^{2'}$) (Ir(cnpmbic)$_3$). The phosphorescence spectrum shows emission at room temperature in the deep-blue region of the visible spectrum peaking at 450 nm. The classification of transitions observed for this compound in the absorption spectrum is carried out in agreement with literature assignments [63, 128]. The peak at a wavelength of 250 nm can be attributed to a ligand-centered (^{1}LC) excitation and the weak maxima at around 310 nm and 350 nm result from S$_0$ to ^{1}MLCT transitions. A shoulder caused by absorption to the
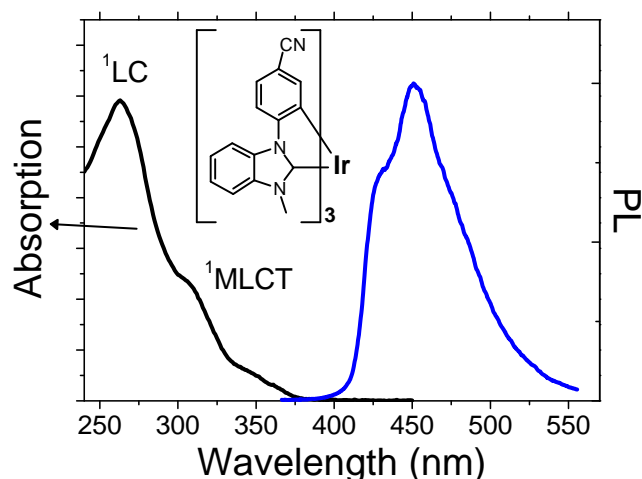
Figure 3.2: *Steady state absorption and emission spectrum of the complex Ir(cnpmbic)$_3$. All the spectra were obtained with the molecules dispersed in a thin film of PMMA. Excitation was performed at 337 nm. In the inset the chemical structure of the compound is shown.*

triplet state is expected at wavelengths higher than 350 nm. Due to the low extinction coefficient of this transition, it is not observable in the absorption spectrum of figure 3.2. Compared to fluorescent molecules, organometallic complexes typically reveal a large Stokes shift and not mirror-symmetrical absorption and emission spectra. This is due to the fact that emission occurs from the triplet state and absorption mainly from the ground to higher lying singlet states, especially to ligand-centered states. The high quantum efficiency ($\Phi_{PL} = 80\%$) and short phosphorescence lifetime ($\tau_T < 20\,\mu$s) make the material shown in figure 3.2 an ideal candidate for an emitter in the deep-blue.

Before synthesis of the emitter materials a quantum chemical screening of potentially luminescent metal complexes by TD-DFT was conducted (section 2.1.1). As an

approximation to the maximum emission wavelength the vertical transition from the S_0 state to the T_1 state was calculated. The calculated wavelengths are in very good agreement with the experiment, reflecting the potential of TD-DFT [129]. In addition, the singlet-triplet splitting ΔE_{ST} was calculated by TD-DFT considering a fixed triplet molecular geometry and a triple zeta valence basis set [110].

3.1.2   Organometallic complex for single molecule studies

While detecting phosphorescence of fluorescent dyes by single molecule spectroscopy (SMS) remains challenging due to the long lifetime of the corresponding triplet excited state (ms‑s), organometallic complexes can overcome this problem. In this material class strong spin-orbit coupling (SOC) is responsible for an enhancement of the phosphorescence radiative rate, enabling lifetimes in the microsecond time regime (section 2.2). However, the number of photons emitted per second is still low compared to what is observed in fluorescent transitions. Therefore, only sparse studies on the detection of single organometallic compounds exist [130, 131, 132].
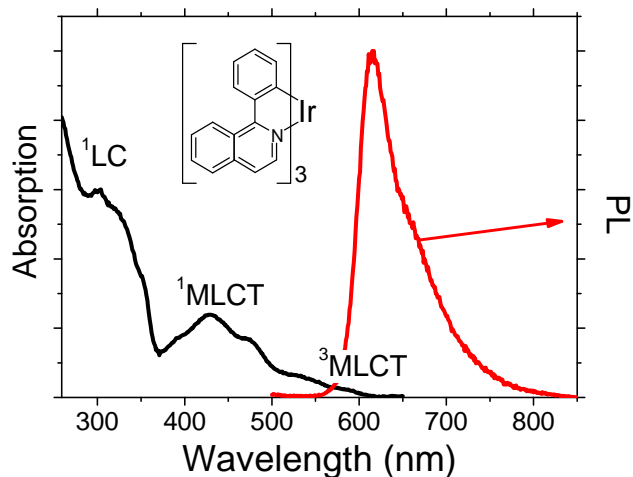

Figure 3.3: *Steady state ensemble absorption and emission spectrum of the compound Ir(piq)$_3$ dissolved in Toluene at room temperature. Excitation was performed at 425 nm. In the inset the chemical structure of the compound is shown.*

Since blue-emitting compounds have to be excited at wavelengths lower than 400 nm, leading to an undesirable increase in the background signal, we have chose to use the red phosphorescent emitter iridium tris(1-phenylisoquinolinato-C^2,N) (Ir(piq)$_3$) for these studies (inset figure 3.3). The absorption spectrum of this compound shows two pronounced shoulders with the maxima at about 300 nm and 430 nm (figure 3.3). The first one corresponds to ^{1}LC and the low energetic one to ^{1}MLCT states. The weak shoulders between 525 nm and 600 nm result from S$_0$ to ^{3}MLCT transitions. The

unstructured emission spectrum exhibits a peak at 615 nm, which is assigned to the 0-0 transition (electronic origin) between the lowest triplet state T_1 and the ground state S_0 [133]. At room temperature Ir(piq)$_3$ has a phosphorescence quantum yield of 26 % and a lifetime of 1.1 μs, which is determined by the strength of SOC [107]. In chapter 5 we present experiments on the single molecule level for observing the fine structure of this compound.

3.1.3 Host materials

During this work, a high number of host compounds were synthesized by the research group at BASF with the aim to use them as host materials for carbene emitters. These tailor-made materials were applied to develop deep-blue electroluminescent devices with excellent efficiency. The most important requirement for these materials is a sufficiently high triplet energy to ensure energy transfer from the host to the emitter (section 2.3.2). Small fluorescent molecules meet this requirement. As an ex-
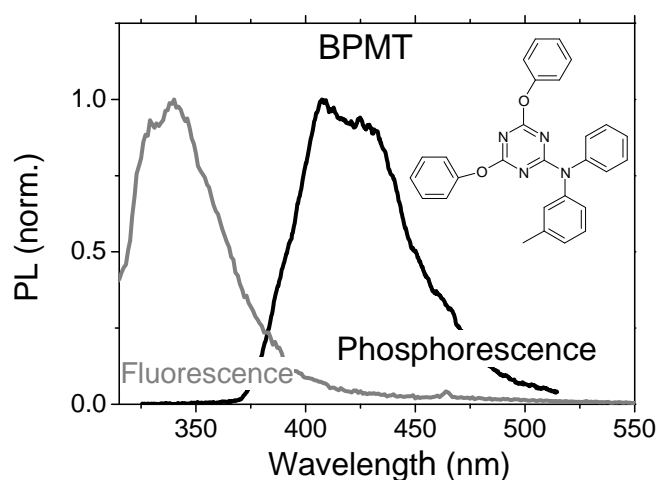
Figure 3.4: *Fluorescence and phosphorescence spectrum and chemical structure of the host material BPMT.*

ample, figure 3.4 shows the fluorescence and phosphorescence spectrum of the material 2,4-Bis(phenoxy)-6-(3- methyldiphenylamino)-1,3,5-triazine (BPMT), together with its chemical structure. The phosphorescence spectrum was observed exclusively by low temperature gated spectroscopy [39]. The energy level of the host triplet exciton is at 3.05 eV (407 nm), exceeding the one of blue emitters which is in the range of 2.76 eV (450 nm). The high energy peak at 3.73 eV (333 nm) in the fluorescence spectrum is assigned to the 0-0 transition (electronic origin) between the S_1 state and the ground state S_0.

If such a large bandgap material is used in an OLED, it can necessitate high operating voltages, in order to reach the current densities ensuring high external efficiencies. An elegant way for obtaining hosts with sufficiently high triplet energies and without the need for a wide electronic bandgap is the use of organometallic molecules as hosts (chapter 6.1.1) [134]. In these compounds the mixing of singlet and triplet states lead to a decreased exchange interaction (chapter 4.4).

3.2 Sample preparation

To investigate the physical properties of the introduced materials, an appropriate sample preparation is necessary. Most experiments were carried out on thin amorphous films, which were produced by spin-coating. We also prepared sandwich structures, where an emitter is dispersed in a host, to study the effect of an electric field on the phosphorescence intensity.

Before preparation of thin films or devices, the employed substrates, ITO or silicon, were cleaned according to the following procedure:

- Isopropanol for 10 minutes in ultrasonic bath

- Aceton for 10 minutes in ultrasonic bath

- Helmanex solution for 15 minutes in ultrasonic bath

- 2x ultrapure water for 10 minutes in ultrasonic bath

- Drying of the substrates with a nitrogen stream

3.2.1 Thin amorphous films

For investigations on thin organic films we use an undoped silicon wafer covered with a 200 nm thick thermal oxid layer. Fabrication of thin films was done by the technique of spin-coating. Here, the materials of interest are dissolved in a suitable ultrapure solvent. In most cases we employed dichloromethane (Merck Uvasol®, purity = 99,9 %). Before the rotary disk of the spincoater is started, a small amount of the solution is deposited onto the substrate by a pipette. The solvent evaporates during the spin-coating and one obtains a homogenous thin film (figure 3.5). A rotation speed of 2500 rounds per minute and a concentration of 10 mg/ml typically produced 100 nm thick films.
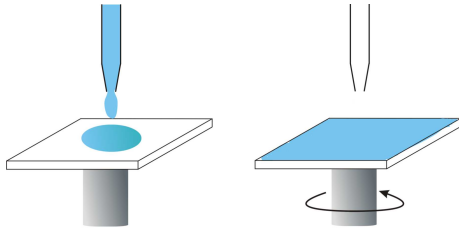
Figure 3.5: *Fabrication of thin organic films by spincoating. Before the rotary disk of the spincoater is started, a small amount of the solution is deposited onto the substrate by a pipette. The solvent evaporates during the spincoating and a homogenous thin film is generated.*

3.2.2 Structures for experiments on field induced quenching

In order to study the effect of the modulation of the emitter phosphorescence intensity upon the application of an electric field, we prepared sandwich structures, where an emitter is dispersed into hosts at low concentrations (chapter 6). The different films were prepared by spin coating from chloroform solutions on top of silicon oxide (SiOx) (thickness $10\,nm$) coated ITO substrates. ITO is a transparent conductor, and therefore an ideal electrode for optoelectronic experiments. A second SiOx layer was then deposited on the organic thin film (thickness $\approx 125\,nm$) before the evaporation of the top aluminum electrode [97]. A scheme of the structure is shown in figure 3.6. SiOx blocking layers were used to minimize charge carrier injection upon the application of voltage and to avoid quenching by the surface plasmons at the metallic interfaces. Experiments were also performed using $10\,nm$ of LiF instead of SiOx with the aim to clarify the intrinsic nature of the effects in contrast to interfacial phenomena. Furthermore, we connected the ITO with the positive and the aluminum with the negative pole. This reverse bias configuration and the SiOx layers assured a low current density, not exceeding $1\,A/m^2$ at $2\,MV/cm$. This experimental configuration allowed us to study the effect of the electric field in the absence of carrier injection and therefore exciton-polaron quenching. Indeed, this quenching mechanism starts to be relevant ($< 3\,\%$) typically for currents larger than $10\,A/m^2$ [105, 135].

To avoid short-circuits between the electrodes, the edges of the ITO layer were removed with an acid. For this step the middle part of the ITO is protected with
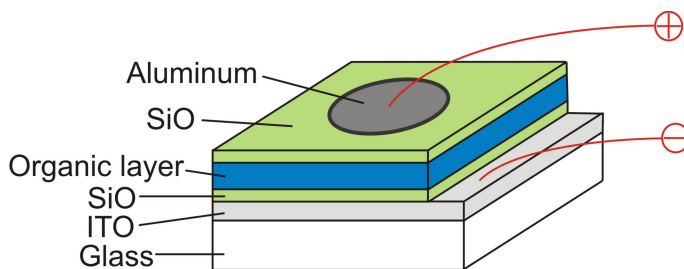
Figure 3.6: *Schematic device setup of the structure used for field induced quenching experiments.*

sticky tape and the device is placed in a solvent of 32 % hydrochloric acid for 10 minutes (figure 3.7 (a)). After cleaning the ITO, SiOx is evaporated crosswise on the ITO layer (b). Then the solution is spincoated onto the substrate (c) and a second SiOx layer is evaportated with the same orientation (d). The form of the aluminum layer is depicted in figure 3.7 (e) [136].
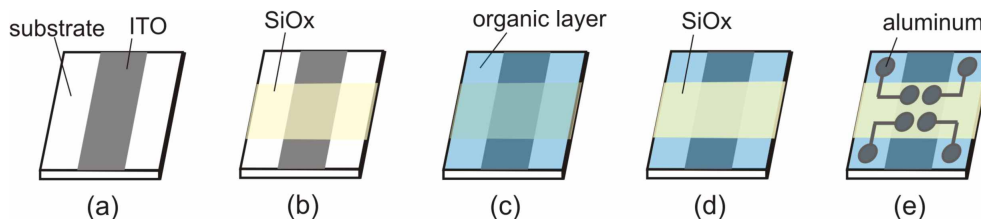
Figure 3.7: *Detailed sample preparation: (a) Etching of the ITO substrate, (b) evaporation of SiOx, (c) spincoating of the solution, (d) evaporation of a second SiOx layer, (e) evaporation of aluminum.*

3.3 Experimental setups

In the following section the experimental setups used in this work are described in detail. We employed time resolved photoluminescence spectroscopy to probe the properties of either pure emitter molecules or dispersed in host/emitter blends. Beside ensemble measurements, we also performed investigations on single phosphorescent triplet emitters with a home-built wide-field emission microscope described in the last part.

3.3.1 Time resolved photoluminescence spectroscopy

To measure fluorescence and phosphorescence of emitter and host materials and also to study the influence of an electric field on the emission properties of emitter molecules, we used following setups, which differ mainly in the type of the luminescence detection (figure 3.8).

In both setups the samples are mounted in a cold finger Helium cryostat. To ensure a good heat exchange, we attached them with silver paste onto the cold finger. The temperature was adjusted between 5 K and 300 K by controlling the helium flow. For all measurements the samples were kept under a dynamic vacuum of 10^{-6} mbar. A quartz window in the cryostat allows the excitation of the samples by a laser source and detection of the PL. The emitted light is then focused onto the entrance slit (width
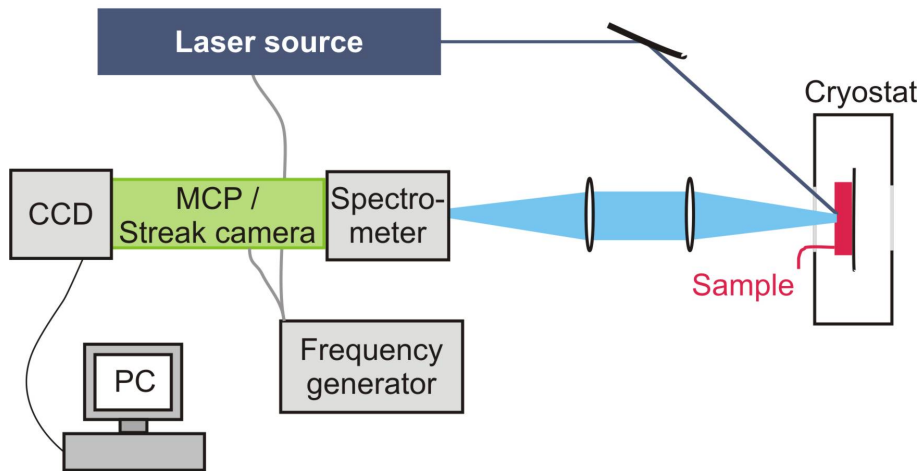
Figure 3.8: *Schematical depiction of the time resolved photoluminescence setup.*

$200\,\mu$m) of a spectrometer (*Chromex 250is/sm*). Before the light hits the charge-coupled device (CCD) camera, it passes through a micro channel plate (MCP) or a streak camera system. The acquired picture can later be analyzed by computer software. The excitation source and the MCP were externally triggered by a frequency generator (*Hewlett Packard 33120a*). For the device structures presented in section 3.2.2 a laser was used as excitation source and simultaneously an electric field was applied to the device by a Keithley source or a pulse generator.

Time gated setup

The core piece of this setup is a temporal switchable MCP (*Princeton Instruments PG-200*), which intensifies photons by the multiplication of electrons via secondary emission. The MCP consists of a semiconducting plate on whose metallized ends an accelerator voltage is applied. The plate is perforated like a sieve with a regular array of tiny channels (microchannels) leading from one end to the other and which have diameters of about $10\,\mu$m. A photon that enters such a channel, knocks an electron out of the wall via photo effect. The generated electrons are then accelerated by an electric field and during their way to the anode they produce further free electrons, like in a photomultiplier. A cascade of electrons starts to propagate through the channel and therefore can amplify the original signal by several orders of magnitude. At the end of the device the electrons are reconverted to photons and detected by a CCD camera. The accelerator voltage can be switched on continuously or for a defined time frame. It is also possible to define the point in time at which the MCP is on with respect to

a trigger signal (laser pulse). Therefore, the MCP not only allows the amplification of weak signals and a high dynamic range, but it also enables the possibility to choose detection windows with a variable width (ns‑ms range) and delay in respect to the optical or electrical excitation.

Streak camera

For time resolved measurements of phosphorescence decays a streak camera system (*Hamamatsu, C5680*) was used. The system was operated with a single sweep plug-in unit (*M5677*), allowing the measurement of luminescence lifetimes in time ranges from 5 ns to 10 ms, which are relevant for observing phosphorescence decays. The highest achievable time resolution is 50 ps. Figure 3.9 shows a scheme of the operation principle
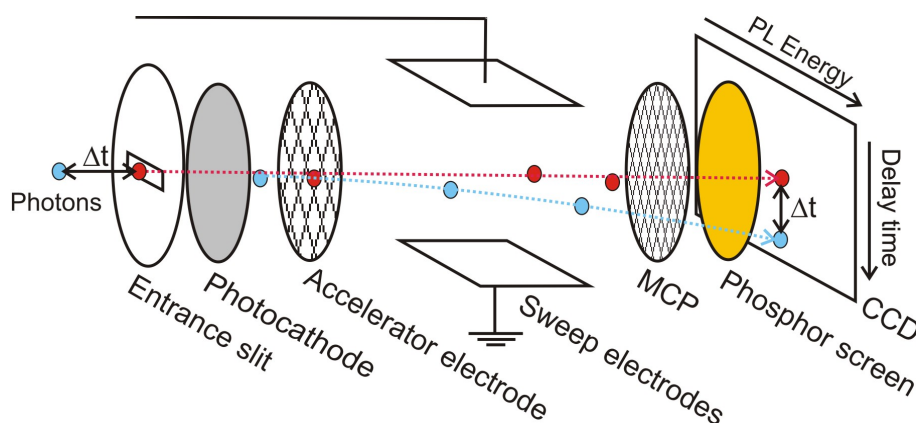
Figure 3.9: *Schematic of the operation principle of a streak camera. Photons arriving the entrance slit with a time delay of Δt (blue spots) are vertically deflected more than photons arriving earlier (red spots). The time delay between photons at the entrance slit can therefore be read out at the image of a CCD camera.*

of a streak camera system. The photons, which are initially dispersed horizontally by a spectrometer, enter a slit and are focused onto a photocathode. Here, they are converted into photoelectrons which are accelerated by an electrode. Afterwards, these electrons enter a region where two electrodes are arranged in a planar capacitor geometry. A sweep voltage, which increases linearly with time, deflects the electrons vertically. The amount of deflection of electrons depends on their arrival time at the vertical electrodes. The latest electrons (blue spots in figure 3.9) see a larger electric field and hence are deflected more than electrons arriving earlier (red spots) in the voltage sweep. In an MCP, which acts here as a photomultiplier, the electrons are amplified before they reach a phosphor screen. Here, they are reconverted to photons,

which produce an image on a CCD camera. The vertical axis measures the amount of deflection and is therefore representative of the time axis. Thus, the resulting image contains the spectral information in the x-axis and the time information in the y-axis.

Excitation sources

Photo excitation of deep-blue emitters and host molecules requires an excitation wavelength in the UV, which is provided either by a pulsed nitrogen laser or by the second harmonic of an optical parametric amplifier (OPA) pumped by a regenerative laser system.

The regenerative laser system: The regenerative laser system (*Coherent, RegA*) consists of a compact Ti:Sa modelocked oscillator, pumped by a Nd:YAG solid state laser at a wavelength of 532 nm with a power of 1.3 W and of a regenerative amplifier system which is also pumped by a Nd:YAG solid state laser at a wavelength of 532 nm with a power of 10 W. The low energy pulses of the oscillator are injected into the amplifier cavity with an acousto-optic cavity dumper. Here, the pulses run about 25 times through the Ti:Sa crystal and are thereby amplified. A second cavity dumper extracts single pulses with an energy of 6 microjoules at a wavelength of 800 nm, which are afterwards compressed to a pulse length of about 70 fs. This particular laser system allows adjustment of the repetition rate between single shot and 250 kHz. The outcoupled pulses are sufficiently intense to allow the generation of pulses in the wavelength region between 420 nm and 750 nm by optical parametric amplification. The pulse energies of the OPA signal are high enough to be converted to pulses in the ultraviolet wavelength region by second harmonic generation, which are then used as the excitation source for blue-emitting molecules.

Nitrogen laser: For most photoluminescence experiments we used a nitrogen laser as the excitation source, emitting pulses with a wavelength of 337 nm, a maximum energy of 20 μJ and a pulse width of 500 ps. The repetition rate can be adjusted between 1 and 50 Hz. Typically, our measurements were performed at low excitation powers (0.1 μJ - 0.5 μJ) and in the absence of high excitation densities thus avoiding quenching processes.

3.3.2   Single molecule photoluminescence spectroscopy

Optical detection and spectroscopy of single molecules started 1989 with the observation of the absorption spectrum of single pentacene molecules by Moerner and Kador at IBM research laboratory [137]. During the years the field of single molecule detection grew rapidly and new experimental methods like scanning force microscopy or scanning tunneling microscopy were developed [138, 139]. Nowadays, detection of single molecules plays a major role in the development of research areas like lifescience or biomedical science [140, 141, 142, 143]. The experimental technique used in this work is based on single molecule photoluminescence spectroscopy. As discussed below, the main requirement for this method is a suitable sample preparation.

Sample preparation

To detect single emitters sufficient spatial separation between single molecules in the sample is necessary. This can be achieved by a high dilution of emitter molecules in a solvent. Before spincoating, the concentration of emitters is typically in the range of 10^{-6} - 10^{-8} mg/ml. Very important for the detection of single phosphorescent emitters is to minimize the background signal of the sample. A single emitter with a spatial extension in the nanometer range is confronted with a much higher surrounding area due to the resolution limitation of the optical instruments. Therefore, for single molecule experiments we used only ultrapure solvents, very clean substrates (section 3.2) and host materials. As substrates we employed silicon wafers, which are covered with a 200 nm thick thermal oxid layer.

In order to create a protective layer for the emitter molecules and thereby protect them from oxygen or water, they are dissolved in toluene to a concentration of about 10^{-5} mg/ml and then dissolved again in a solution consisting of a mixture of toluene (*Merk, Uvasol*) and Zeonex (*Zeon Corporation, Zeonex 480R*). Before a small amount of such a solution (30 μl) is spincoated at 5000 rpm onto a silicon substrate, the substrate is cleaned for 10 minutes in a plasma cleaner. The thickness of the produced layers is in the range of 30 nm, determined by a DekTak profilometer.

Experimental setup

Figure 3.10 shows the home-built wide-field emission microscope used for single molecule detection. As the excitation source we used a Ti:Sa laser (*Spectra Physics, Tsunami*)
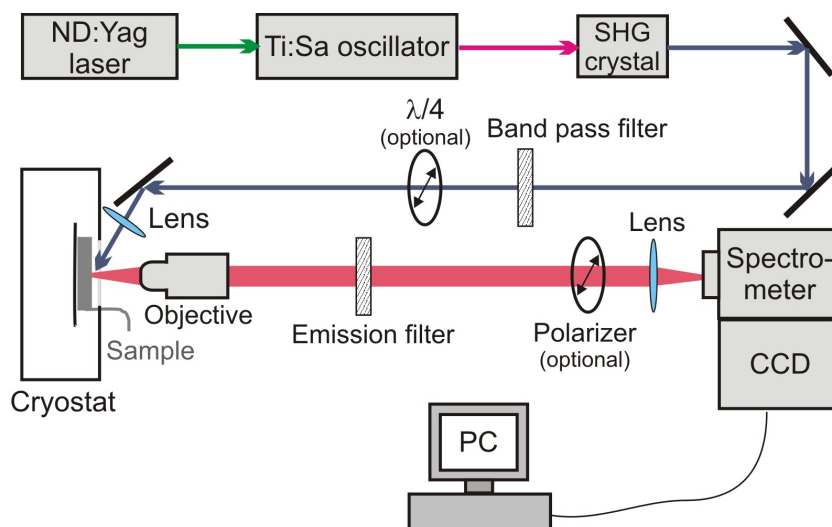
Figure 3.10: *Schematic illustration of the setup used for detection and spectroscopy of single molecules at temperatures down to 5 K.*

with a repetition rate of 80 MHz and a pulse width of < 100 fs. By second harmonic generation pulses with a wavelength between 370 nm and 450 nm with a power of 20 mW are produced. The excitation wavelength selection is carried out by a narrowband interference filter. By inserting a $\lambda/4$-plate in the beam path, circularly polarized excitation light can be generated. Before hitting the sample, the beam is directed onto a mirror and then focused by a lens to a circular point. By variation of the mirror position, the focus point on the sample can be shifted, in order to achieve an overlap with the focus of the objective. The sample is mounted in a helium-flow cryostat (*Cryovac, Konti-Cryostat-Mikro*), which allows experiments in a temperature range from 5 - 300 K in vacuum. For low temperature experiments a good thermal contact between the sample and the cryostat finger is crucial. The emission of the sample is collected with a microscope objective (*Olympus PlanFC*), which has a magnification of 40 and a numeric aperture (NA) of 0.55. An emission filter in the light path filters out the scattered laser light, so that only light emitted by the investigated material arrives at the spectrometer (*Chromex 250*). Additionally, to investigate the plane and degree of polarization of photoluminescence, an electrically controlled polarization filter ($\lambda/2$-plate) can be used. The spectrometer is equipped with a mirror and two different gratings (300 and 1200 lines/mm). The best achievable spectral resolution of this setup is 0.1 nm. The detection of single molecule photoluminescence is accomplished with a high efficiency front-illuminated CCD camera (*PCO AG, Sensicam QE*). By using the

mirror of the spectrometer it is also possible to obtain a space-resolved luminescence picture of the sample surface (resolution $\approx 0.6\,\mu$m) (x-y).

Detection efficiency

A critical factor for detecting single molecule emission, especially emission from a long-living triplet state, is the detection efficiency. Hereby, the microscope objective is the limiting element, since it can only capture a small fraction of the solid angle of emission. Due to the use of a cryostat the working distance is limited to at least 8 mm. This long distance limits the choice of the objective. In this setup the NA of the objective is 0.55. According to reference [144], the detection efficiency of the objective η_{obj} is given by

$$\eta_{obj} = \frac{1}{2}\left(1 - \sqrt{1 - \left(\frac{NA}{n}\right)^2}\right) = 0.08, \tag{3.1}$$

where n is the refractive index of air. Assuming an isotropic emission of the molecule, only 8% of the emitted light can be detected. If one takes into account losses caused by the optical components, the detection efficiency of the camera ($\eta_{camera} \approx 60\%$ at 500 nm) and the diffraction efficiency of the spectrometer ($\eta_{spectr} \approx 70\%$ at 500 nm), the detection efficiency of the hole setup η_{setup} in spectral mode is only about 2 %. However, as will be shown in chapter 5, this efficiency is still high enough to detect single phosphorescent molecules.

The maximum number of emitted photons from a molecule is determined by the radiative rate k_R of the excited state and by the excitation power. The radiative lifetime of the investigated molecule is in the μs range. As the repetition rate of the used laser is 80 MHz, meaning that every 12 ns a pulse is sent out, the molecules are quasi-continuously excited by the Ti:Sa laser. Assuming a quantum efficiency of 100% and a radiative rate of 10^6 μs^{-1} for emitter of interest, the maximum counting rate of the CCD detector is

$$k_{count} = k_R\eta_{setup} = 2\cdot 10^4 s^{-1}. \tag{3.2}$$

Compared to fluorescent emitters, the counting rate is 1-3 order of magnitudes smaller. Therefore, studies on single phosphorescent emitters are challenging and require long integration times.

Chapter 4

Controlling the radiative rate of blue organometallic complexes

In this chapter we start presenting the optical properties of a novel series of deep-blue organometallic complexes. Then we discuss the role of spin-orbit coupling and singlet-triplet splitting in controlling the radiative rate of phosphorescence. This is done for complexes with well defined variation in the molecular structure involving the metal ions and the organic ligands. By time gated photoluminescence spectroscopy we are able to observe fluorescence from the perturbing singlet states, which allows us to extract the singlet-triplet splitting ΔE_{ST}. This experimentally determined value was compared with calculated ones showing a remarkable agreement. The determined splittings show a strong correlation with the radiative rate suggesting a new approach in obtaining efficient and fast phosphorescence emission. The exchange interaction which determines the singlet-triplet splitting scales according to the electron-hole wave function overlap inferred from the intramolecular charge transfer character of the emitting state.

4.1 Photophysical properties

Figure 4.1 shows the absorption and emission spectra at room temperature of a series of deep-blue emitters, where only the metal ion is changed and the ligand structure is similar. The classification of the transitions observed in absorption for the compounds, rhodium tris(1-cyanophenyl-3-methylimidazolin-2-ylidene-C,C$^{2'}$) (Rh(cnpmic)$_3$) (panel a), iridium tris(1-cyanophenyl-3-methylimidazolin-2-ylidene-C,C$^{2'}$) (Ir(cnpmic)$_3$) (panel
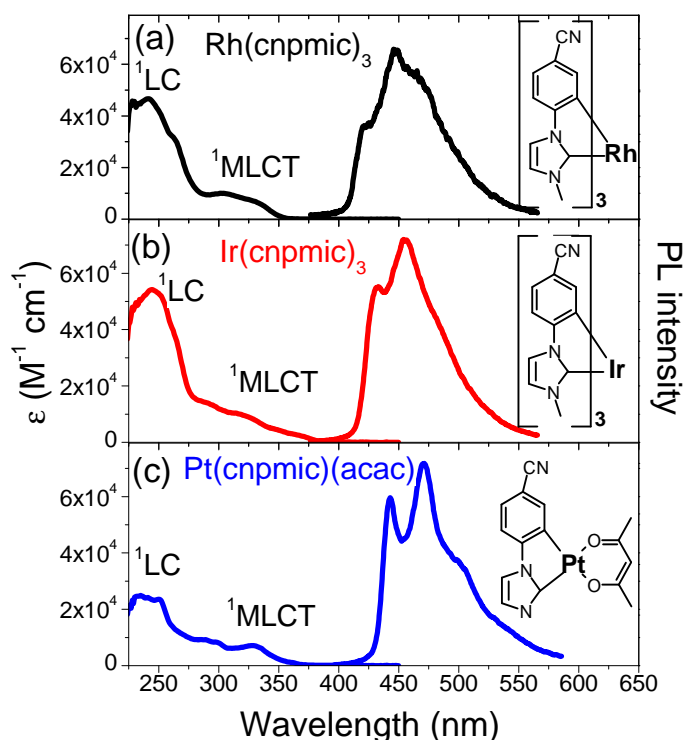
Figure 4.1: *Absorption and emission spectra of three organometallic complexes, where the metal ion is changed, while the ligand structure is retained. The strong transitions with a maximum at around 250 nm can be attributed to ^1LC excitations. The shoulders between 275 nm and 350 nm result from ^1MLCT states. All complexes show efficient room temperature emission in the deep-blue spectral region, where the emission maximum is between 440 nm and 460 nm. The insets show the chemical structure of the respective complex.*

b), and platinum (1-cyanophenyl-3-methylimidazolin-2-ylidene-C,C$^{2`}$) (acetylacetonate) (Pt(cnpmic)(acac)) (panel c), is carried out in agreement with literature assignments and in accordance to section 3.1 [63, 128]. The strong transitions with a maximum at around 250 nm can be attributed to ligand-centered ($S_0 \rightarrow {}^1LC$) transitions. The shoulders between 275 nm and 350 nm result from ^1MLCT states. A weak shoulder caused by absorption to the triplet state is expected at wavelength higher than 350 nm, but due to its low extinction coefficient it is not observable in figure 4.1. The absorption spectra of the three complexes are quite similar with the only difference that Pt(cnpmic)(acac) has in general a weaker extinction coefficient ϵ due to the lower number of organic ligands, one instead of three.

All complexes show efficient room temperature phosphorescence in the deep-blue spectral region ($\lambda_{emission} < 450$ nm). The Commission internationale de l´eclairage (CIE) coordinates are (0.15/0.11), (0.15/0.10), and (0.16/0.19) for Rh(cnpmic)$_3$,
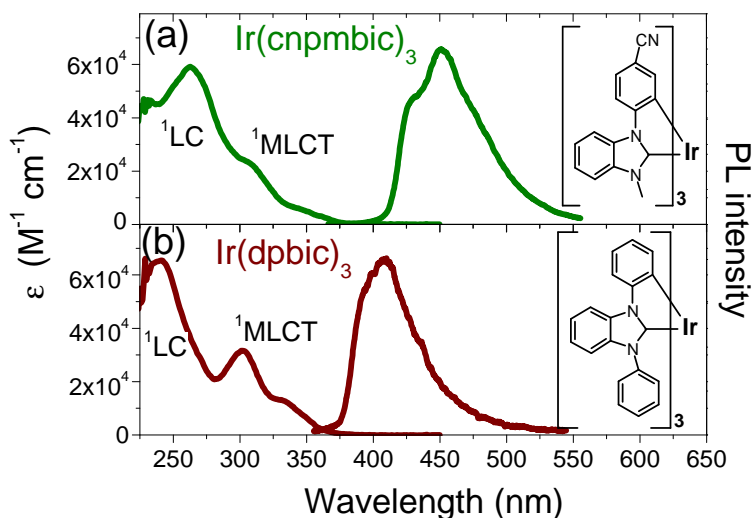
Figure 4.2: *Steady state spectra are performed on iridium complexes where the ligand structure was modified to tailor the electronic properties. The assignment of transitions for the first complex, Ir(cnpmbic)$_3$ (panel a) are in accordance to the complexes reported above. We note that the compound Ir(dpbic)$_3$ (panel b) shows more pronounced ^{1}MLCT absorption shoulders compared to the other complexes with maxima at 300 nm and 330 nm. The phosphorescence spectrum of Ir(dpbic)$_3$ peaks in the UV-region at 400 nm and shows no pronounced vibrational satellites. The insets show the respective chemical structure.*

Ir(cnpmic)$_3$, and Pt(cnpmic)(acac), respectively. The insets of figure 4.1 show the respective chemical structure. The emission spectrum of Pt(cnpmic)(acac) shows more pronounced vibrational satellites than the other compounds, indicating a less pronounced metal participation in the emissive state [63].

The same optical characterization is performed on iridium complexes where the ligand structure was modified to tailor their electronic properties (figure 4.2). The insets show the corresponding chemical structure. The assignment of transitions for the first complex, Ir(cnpmbic)$_3$ are in accordance to the complexes reported above. The compound iridium tris(1-phenyl-3-phenylbenzimidazolin-2-yilidene-C,C$^{2`}$ (Ir(dpbic)$_3$) shown in panel (b) has more pronounced ^{1}MLCT shoulders compared to the other complexes with maxima at 300 nm and 330 nm. The phosphorescence spectrum is blue-shifted compared to the complexes reported above. It peaks in the UV-region at 400 nm and shows no pronounced vibrational satellites, only a broad emission and unstructured phosphorescence is visible.

Figure 4.3 (a) shows time resolved phosphorescence at room temperature for all complexes presented above. While the decay time constant for most is in the range
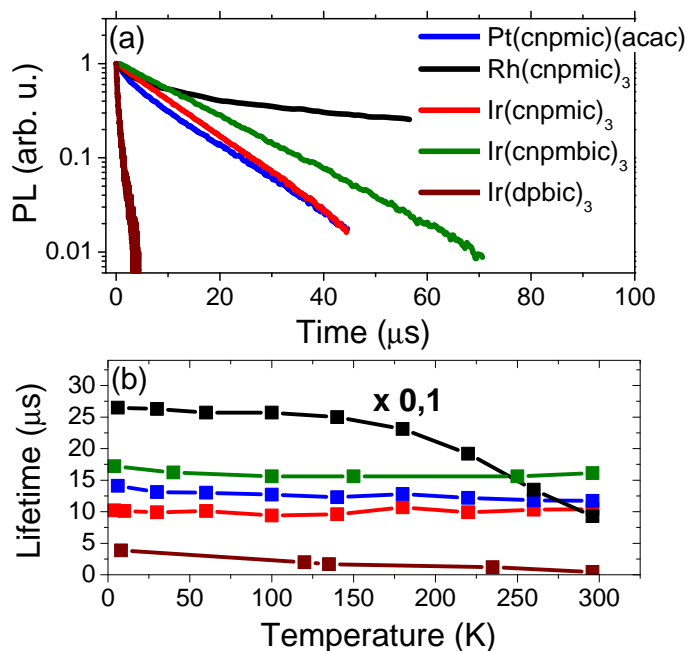
Figure 4.3: *(a) Time decay of a series of carbene complexes at room temperature. The emitters are doped in low concentration in a PMMA host (conc. 2%w/w). Excitation wavelength was 337 nm. (b) Lifetime of the first excited triplet state of the molecules of interest as a function of the temperature.*

of $10\,\mu$s, Rh(cnpmic)$_3$ (black curve) has a decay constant of about $100\,\mu$s. Due to the low atomic number of rhodium, spin-orbit coupling (SOC) is much weaker and therefore the phosphorescence lifetime is longer when compared with the other compounds. The large SOC of organometallic complexes which employ the metal atoms iridium or platinum makes them more interesting for applications in OLEDs. Ir(dpbic)$_3$ has the fastest lifetime of all complexes. However, it has a relative low quantum yield at room temperature of $\Phi_{PL} = 19\,\%$ (table 4.1). Figure 4.3 (b) shows how the lifetimes are changing as a function of temperature. In accordance with the presence of non-radiative channels, Ir(dpbic)$_3$ shows larger lifetimes at low temperature. Apart from Ir(dpbic)$_3$ and Rh(cnpmic)$_3$, the other compounds show no temperature activated non-radiative losses, reflecting the potential of carbene based complexes to achieve efficient deep-blue emission.

In table 4.1 the photoluminescence quantum yield Φ_{PL} and the lifetime of the triplet state τ_T are summarized for all investigated complexes. As mentioned, the low Φ_{PL} of Ir(dpbic)$_3$ is due to non-radiative channels, while the one of Rh(cnpmic)$_3$ to the low radiative rate of the emitting state.

|	$\Phi_{PL}(\%)$	τ_T (μs)
Ir(cnpmic)$_3$	78	12
Ir(cnpmbic)$_3$	78	16
Ir(dpbic)$_3$	19	1
Pt(cnpmic)acac	39	12
Rh(cnpmic)$_3$	12	100

Table 4.1: *Phosphorescence quantum yield Φ_{PL} and lifetime τ_T of deep-blue emitting carbene complexes at room temperature [34]. Measurements were performed on thin films, where the carbene emitters are doped at low concentration in a PMMA host (conc. 2%w/w).*

4.2 Determination of the singlet-triplet splitting

As described in chapter 2.4, OLEDs benefit from a shorter phosphorescence lifetime, eventually approaching the sub-microsecond time regime. A shorter phosphorescence lifetime decreases not only the residence time of potentially unstable excited states, but also processes detrimental to the efficiency, such as exciton charge-carrier quenching or triplet-triplet annihilation, could be strongly reduced with a faster exciton recombination (section 2.4.2). To decrease the phosphorescence lifetime while maintaining high quantum efficiencies a large radiative rate is required. This rate is directly proportional to the SOC matrix element involving the emitting triplet and the perturbing singlet state and inversely proportional to the degree of mixing between them, i.e., the singlet-triplet splitting ΔE_{ST} (section 2.2.2, equation 2.16). Photophysical studies on the role of SOC and ΔE_{ST} in tuning the radiative rate are still sparse, mainly because of the large intersystem-crossing (ISC) times of such phosphors, which makes estimations of SOC and detection ΔE_{ST} rather challenging [60].

Because of the large SOC, fluorescence from the S$_1$ is expected to be short living. We have tackled this experimental challenge by using time-gated spectroscopy which offers a time resolution of 2 ns after the laser pulse and a high dynamic range, necessary for the expected weak fluorescence. Figure 4.4 shows the detection scheme. The detection window is marked in light blue, the laser pulse purple and the fluorescence and phosphorescence intensities in time yellow and gray, respectively. The width of the detection window can be chosen from 20 ns to a few ms. The time delay between the laser pulse and the excitation pulse can be modified down to 2 ns. As we will demonstrate later on, by choosing a very small temporal detection window of 20 ns and moving the window immediately to the laser excitation, we are able to detect prompt emission spectra, which are blue-shifted compared to the phosphorescence and
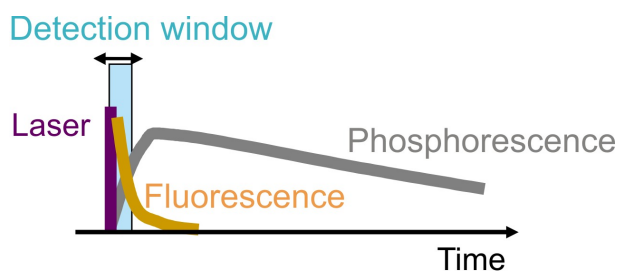
Figure 4.4: *Detection scheme for measurements of fluorescence and phosphorescence of organometallic complexes. By moving the detection window to the initial laser emission we are able to detect prompt emission, which is expected to be blue-shifted compared to the long-lasting phosphorescence. The minimal temporal width of detection is 20 ns and can be shifted by 2 ns.*

are assigned to fluorescence emission ($S_0 \rightarrow S_1$).

4.2.1 Complexes with different metal ions

Figure 4.5 shows prompt (solid lines) and delayed (dashed lines) PL spectra at 5 K for the complexes, Rh(cnpmic)$_3$ (panel a), Ir(cnpmic)$_3$ (panel b) and Pt(cnpmic)(acac) (panel c) recorded in a time window of 20 ns either ending immediately after (1 ns delay) the excitation event or starting 20 ns after it, respectively. For maximum clarity of the emission spectral features, the PL of the rhodium complex is given on a linear scale and that of the iridium and platinum complexes on a logarithmic scale. The observation of emission bands below 400 nm in the prompt PL clearly demonstrates the presence of a bright emitting state at higher energy with respect to the long-lived phosphorescence, peaking in the range 420 - 440 nm for all of the complexes. The short-lived nature of these blue-shifted emission bands is unequivocally demonstrated by the delayed spectra. As the detection window is shifted by 20 ns, the high energy emission diminishes below the sensitivity detection limit of our CCD for Ir(cnpmic)$_3$ and Pt(cnpmic)(acac). Interestingly, we observe that the relative intensity of these high energy bands with respect to their phosphorescence scales according to the respective metal-ion atomic number ($Z_{Rh} = 45$, $Z_{Ir} = 77$, $Z_{Pt} = 78$). According to the fourth power relation between Z and the SOC (section 2.2.2), this observation suggests a fluorescent singlet state at the origin of the blue emission bands seen from these nominal triplet emitters [38, 64, 70].

For the rhodium complex, the high energy band amounts to almost 1 % of the total steady-state emission spectrum (not shown) and clearly has the longest lifetime, since emission is still detected in the delayed spectrum. We propose that this short-
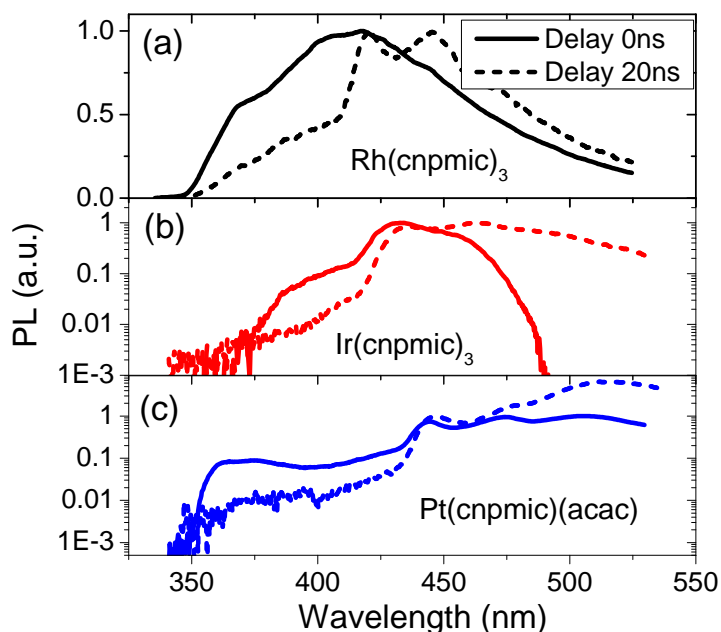
Figure 4.5: *Low temperature (T = 5 K) transient photoluminescence spectra of the three complexes detected in a temporal window of 20 ns, closing immediately after excitation, (prompt PL, solid line) and delayed 20 ns after the excitation event (dashed line). Spectra are normalized to the phosphorescence maximum. All plots are semilogarithmic except for Rh(cnpmic)$_3$, for maximum clarity of the spectral features. Pulsed excitation was performed at 337 nm.*

lived high-energy emission is due to prompt fluorescence from a bright singlet state. Support for this assignment is given by the decrease of the high energy band intensity as the temperature is increased. Figure 4.6 reports the normalized intensity ratio between singlets and triplets in the prompt (zero delay) spectrum of Rh(cnpmic)$_3$, Ir(cnpmic)$_3$ and Pt(cnpmic)(acac), illustrating a higher intensity for fluorescence at low temperature. These thermochromic effects can either originate from a decreased ISC rate due to a reduced Franck-Condon integral with decreasing temperature; or from an increase in non-radiative decay of the singlet at elevated temperatures [70]. Regardless of the exact origin of the intensity variation with temperature, this result is in agreement with our assignment of the high energy bands to fluorescence [38]. Low-temperature time-gated PL spectroscopy therefore provides a facile way of accessing the singlet energy levels of a phosphorescent compound.
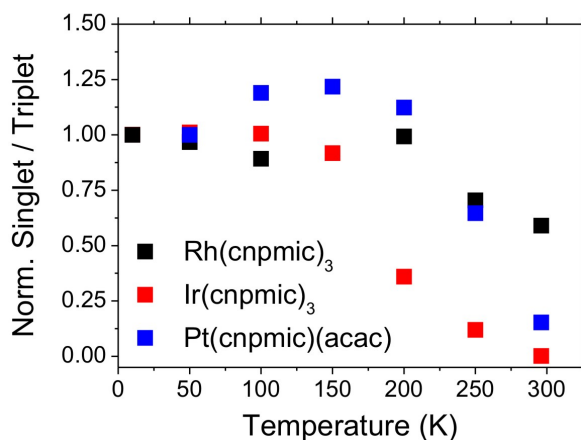
Figure 4.6: *Dependence of the normalized singlet to triplet intensity ratio in the prompt emission on temperature.*

4.2.2   Complexes with modified ligand structure

We performed the same type of low-temperature experiments described above on iridium complexes where the ligand structure was modified to tailor the electronic properties. In Figure 4.7 we report the prompt (solid line) and delayed (dashed line) PL spectra of the organometallic complexes Ir(cnpmbic)$_3$ and Ir(dpbic)$_3$. While the singlet transition energy can be obtained for Ir(cnpmbic)$_3$ as clearly seen from the broad maximum centered at 380nm in the prompt PL spectrum (solid line in Fig. 2b), no emission was detected on the high energy side of the Ir(dpbic)$_3$ phosphorescence: the delayed and prompt spectra are identical, the slight shoulder on the high energy side of the spectrum being a characteristic of the triplet. A very small ΔE_{ST} or a much faster ISC with respect to the other complexes are probably at the origin of the fluorescence not being detectable in the latter case.

Detection of singlet emission in phosphorescent complexes is often a challenge due to the large SOC and consequently the fast ISC. To date, only a few reports have demonstrated the detection of light emission from higher-lying singlet states [132, 145, 146]. The present experiments differ from previous report on delayed fluorescence, in the sense that singlet emission is now detected only in a window closing one nanosecond after the laser excitation, symptomatic of prompt rather than delayed fluorescence. In Table 4.2 we compare the experimentally determined splittings (ΔE_{ST}^{exp}) from the fluorescence emission peaks of figures 4.5 and 4.7 with the values obtained from TD-DFT calculations (ΔE_{ST}^{calc}) performed on the optimized triplet geometries with a triple zeta valence basis set [110]. The remarkable agreement between the calculated and experimental values further supports our assignment of the spectral features to a simple
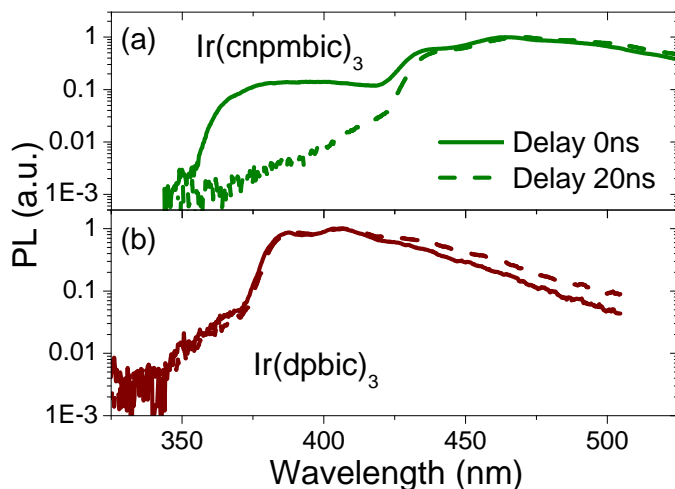
Figure 4.7: *Low temperature (5 K) transient photoluminescence spectra of Ir(cnpmbic)₃ (panel a) and Ir(dpbic)₃ (panel b). The same experimental configuration as for the spectra of figure 4.4 was used, with the solid line representing the prompt spectra and the dashed line the PL 20 ns after excitation. Excitation was performed at 337 and 300 nm for Ir(cnpmbic)₃ and Ir(dpbic)₃, respectively.*

three level system. Interestingly, the lowest ΔE_{ST}^{exp} value is obtained for Ir(dpbic)$_3$, for which no singlet emission could be observed.

Before discussing the role of the splitting in tuning the phosphorescence radiative rate, we briefly comment on the other photophysical parameter reported in Table 4.2. By comparing the measured phosphorescence radiative rates k_r of the complexes differing by the metal ion (rows 1 to 3), the increase of k_r by an order of magnitude with Z^4 is apparent. This increase is reflected in the term containing the SOC matrix element. For Ir- and Pt-complexes the trend seems to be determined by the ΔE_{ST}.

|	ΔE_{ST}^{exp} [exp] (eV)	ΔE_{ST}^{calc} (eV)	k_r ($10^4 s^{-1}$)	Z^4 10^6
Rh(cnpmic)$_3$	0,37	0,36	0,129	4,1
Ir(cnpmic)$_3$	0,19	0,16	7,5	35,2
Pt(cnpmic)(acac)	0,57	0,6	3,33	37
Ir(cnpmbic)$_3$	0,31	0,19	4,9	35,2
Ir(dpbic)$_3$	-	0,04	50	35,2

Table 4.2: *Photophysical properties of deep-blue emitting carbene complexes. The experimentally determined (ΔE_{ST}^{exp}) and the theoretically calculated (ΔE_{ST}^{calc}) singlet-triplet splittings, the phosphorescence radiative rate (k_r) and the metal ion atomic order numbers (Z^4) are summarized in the table. All the energy values are in eV.*

4.3 Correlation between radiative rate and singlet-triplet splitting

Having demonstrated the possibility of experimentally determine the splitting ΔE_{ST} and knowing k_r, which is extracted from the phosphorescence lifetimes and the quantum yields, enables us to make considerations on the role of ΔE_{ST} in controlling k_r. Taking into account only the lowest excited singlet and triplet state, the radiative rate for the emitting triplet state can be approximated by (section 2.2.2)

$$k_r = const \cdot E_{em}^3 \left| \frac{\langle \Phi_{S_1} |H_{SO}| \Phi_{T_0} \rangle}{\Delta E_{ST}} \mu_{S_1} \right|^2 . \tag{4.1}$$

Although the relative fluorescence intensity shows a modulation with temperature (see figure 4.6), the energetic position of the singlet emission does not exhibit any detectable variation with temperature, which means that ΔE_{ST} shows a negligible dependence on temperature. This observation allows the use of equation 4.1 without considering explicitly any temperature sensitive parameter.
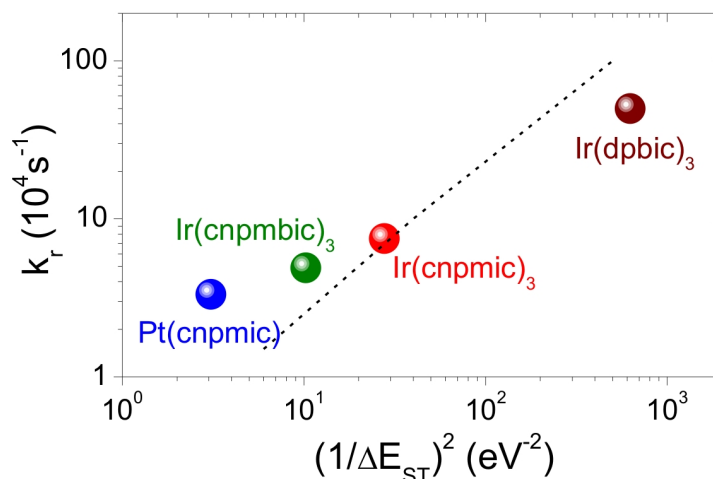
Figure 4.8: *Phosphorescence radiative rate as a function of the experimentally measured singlet-triplet splitting for the complexes investigated. In the case of Ir(dpbic)₃ the ΔE_{ST} obtained from the TD-DFT calculations is plotted, rather than the experimental value. The dashes line reflects the linear dependence of the two plotted parameters.*

Figure 4.8 summarizes the dependence of the measured k_r on the splitting ΔE_{ST}. For a better visualization of the effect of ΔE_{ST} we considered here only complexes with a comparable Z number (note that for Ir(dpbic)₃ ΔE_{ST}^{exp} is not measured and the

value from DFT calculations is considered). Smaller splittings are generally observed for the iridium complexes, where the decreasing splitting leads to the highest radiative rates. These materials are clearly most suited for device applications. The importance of a low ΔE_{ST} in enhancing the radiative rate is clearly emphasized by the correlation observed in the iridium complexes with different ligands. Although the data points in figure 4.8 give a qualitative trend, the significance of ΔE_{ST} in controlling the radiative rate for these phosphorescent complexes is apparent and suggests a new approach in the design of electroluminescent materials based on triplet emitters.
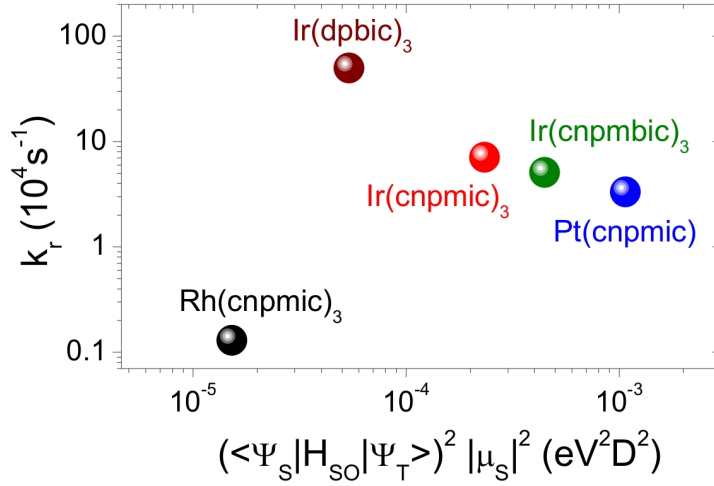
Figure 4.9: *Influence of spin-orbit coupling on the phosphorescence radiative rate. k_r is plotted against $|\langle \Psi_S | H_{SO} | \Psi_T \rangle|^2 \mu_{S_1}^2$.*

Equation 4.1 can also provide an estimation of the SOC matrix element in the numerator, since the other quantities apart from μ_{S_1} are experimentally determined. Figure 4.9 shows extracted SOC matrix element $|\langle \Psi_S | H_{SO} | \Psi_T \rangle|^2$ multiplied by the singlet transition dipole $\mu_{S_1}^2$ in eV^{2}D^2 as a function of the radiative rate k_r as obtained from equation (4.1). The qualitative trend in figure 4.9 is expected considering the atomic number order of the metal ions. Thus, platinum has the largest SOC contribution. However, its high ΔE_{ST} does not allow to reach high radiative rates. This observation clarifies that high SOC do not necessarily result in high phosphorescence radiative rates, if the resonance condition, i.e. a low ΔE_{ST} is not met.

4.4   Exchange interaction and electronic delocalization

In fluorescent organic materials such as conjugated polymers or oligomers, ΔE_{ST} is of the order of $0.8\,\mathrm{eV}$ and depends on the large exchange interaction which is characteristic of strongly bound electron-hole pairs such as Frenkel excitons (section 2.1.2) [39, 41, 147, 148]. As a consequence, more delocalized charge transfer states such as polaron-pairs show a reduced singlet-triplet splitting [11, 149]. While in conjugated molecules such states are usually ascribed to intermolecular excitations, in organometallic complexes they can have an intramolecular nature, due to the peculiar transitions involving the d- and π-orbitals of the metal and the ligands, respectively [11, 39, 150]. The degree of d-orbitals participation in the transition is usually referred as MLCT character (section 2.2). Considering Ir(dpbic)$_3$, which shows the largest k_r, the molecular origin of this enhanced charge transfer character and consequently lower exchange interaction (negligible ΔE_{ST}), can be related to the slightly increased π-conjugation in the ligands and to a larger contribution of d-orbitals to the transition. Therefore, enhancing the MLCT character in the corresponding wave function reduces ΔE_{ST}.

Several studies have demonstrated how the room temperature vibronic structure of the emission spectra can provide qualitative information on the MLCT character of the emitting triplet state [80, 151]. As a general rule, the more resolved the vibronic progression of the spectrum is, the lower the MLCT character is. The iridium complexes show different levels of resolution in the vibronic satellites (see figure 4.2) with a less-resolved structure in the case of Ir(dpbic)$_3$. This underlines a pronounced MLCT character in the emissive triplet state of Ir(dpbic)$_3$ and speaks in favor of an important role of the d-orbitals in engineering the exchange interaction in organometallic complexes.

We therefore confirm our hypothesis that the MLCT character influences the splitting ΔE_{ST}, which in turn controls the radiative rate of the complexes. The increase in the π-conjugation of the ligands is also expected to play a role in tuning the splitting. Since absorption determine the probability of a transition and the radiative rate is a direct measure of this, it is not surprising that Ir(dpbic)$_3$ shows the most pronounced triplet absorption bands. Although this complex shows the highest radiative rate among the complexes presented, its poor emission efficiency (Table 4.2) is mainly determined by a competing non-radiative channel, most probably related to the tor-
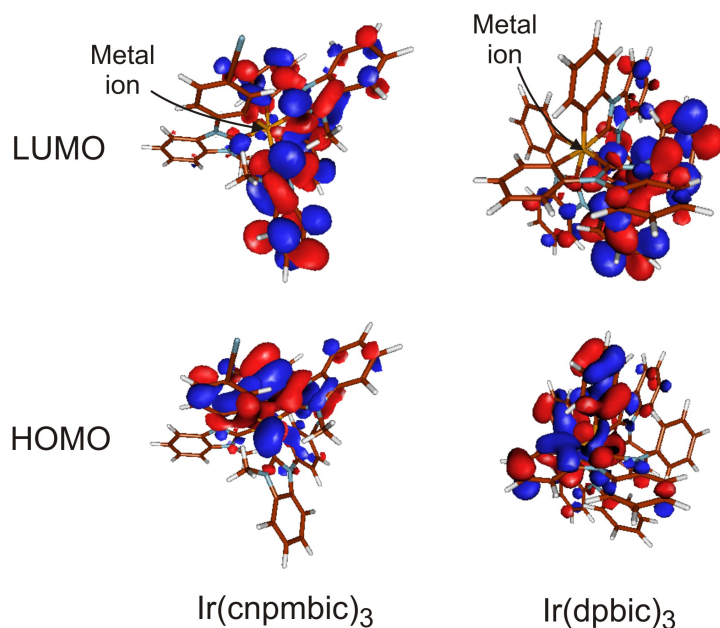
Figure 4.10: *Contour plots of the electron density of HOMO and LUMO for the complexes Ir(cnpmbic)₃ and Ir(dpbic)₃. Additionally, their geometrical structure is depicted. The metal ion is surrounded by three organic ligands. For details see text.*

sional degree of freedom of the phenyl group linked to the carbene moiety. Moreover, the large optical gap in this complex (3.23 eV) may facilitate the population of high-lying non-radiative states via thermal activation [115]. As a consequence, engineering of ΔE_{ST} for high phosphorescence radiative rates also necessitates the prediction of possible non-radiative channels.

We discuss now the MLCT character of the lowest emitting triplet state with the help of contour plots of HOMO and LUMO. Figure 4.10 show contour plots of the electron density of HOMO and LUMO for Ir(cnpmbic)₃ and Ir(dpbic)₃. Besides, their geometrical structure is depicted. The metal ion is centered in the middle and surrounded by three organic ligands. For both molecules the LUMO is delocalized over the carbene ligands. The HOMO instead considers both orbitals from the metal and the ligands. This orbital representation helps in visualizing the nature of MLCT transitions. For Ir(dpbic)₃ the electron density is more located on the centric metal atom compared to Ir(cnpmbic)₃ and the HOMO LUMO orbitals are well separated in the molecular framework with a low overlap. Therefore, the fraction of d-electrons taking part in the transition from the ground state to the lowest excited triplet state is for Ir(dpbic)₃ higher than for Ir(cnpmbic)₃. The calculated contribution of d-electrons in this transition is 47 % and 31 % for Ir(dpbic)₃ and Ir(cnpmbic)₃, respectively. As

mentioned above, the pronounced contribution of d-orbital electrons from the iridium atom is significant for the photophysical properties. In general, the higher the MLCT character of a transition, the higher the radiative rate is expected to be.

4.5   Summary

In this chapter, we have analyzed the physical parameters which control the radiative rate in phosphorescent organometallic complexes emitting in the deep-blue. The experimental results reveal the importance of ΔE_{ST} in controlling the phosphorescence radiative rate. Complexes with very small values of ΔE_{ST} exhibit the highest radiative rates. Differences in the exchange interaction cause a variation of the electronic delocalization of the corresponding wave functions, which depends on the contribution of d-metal orbitals. A more pronounces MLCT character leads to an increased delocalization of the emitting exciton and therefore to a reduced singlet-triplet splitting. Our experimental values of ΔE_{ST} show a remarkable agreement with calculated ones, obtained from TD-DFT calculations. Due to the high phosphorescence quantum yields, these materials are promising dopants in all triplet-emitting OLEDs to create white light in combination with green and red phosphorescent emitters. Additionally, we note that exciton formation in a working OLED proceeds by opposite charge injection in the HOMO and LUMO of the emitting molecule, followed by thermalization to the emitting triplet state. As a consequence, a lowering of the ΔE_{ST} will also optimize the power conversion efficiency and minimize waste heat in working devices.

Chapter 5

Single molecule spectroscopy of organometallic complexes

Organic molecules with iridium atoms built into the structure are very efficient phosphorescence emitters. The high spin orbit coupling provided by the central heavy metal atom allows the observation of intense phosphorescence. While detecting phosphorescence in single molecule spectroscopy remains challenging, due to the long lifetime (ms) of the triplet excited state, iridium complexes can overcome this problem. The large spin orbit coupling is responsible for an enhancement of the phosphorescence radiative rate, enabling lifetimes in the sub-microsecond time regime. Therefore, the number of photons emitted per second by a single molecule is sufficient to detect emission spectra from single phosphorescent complexes. The successful spectroscopical observation of single organometallic complexes can give important insight into the electronic structure of single emitters in the absence of inhomogeneous spectral broadening of the ensemble. In this chapter not only do we demonstrate the detection of phosphorescence from single molecules, but we report on the observation of the zero-field splitting of the triplet manifold. Interestingly, the zero-field splitting shows spectral diffusion, which is ascribed to modifications in the molecular geometry following the photoexcitation process and to fluctuations in the local environment of single molecules in the host. These results show the importance of structural modifications involving molecular excited states in the spectral diffusion of single molecules.

5.1   Detection of single phosphorescent molecules

Single molecule spectroscopy (SMS) is a powerful technique for studying the behavior of single molecules at the nanoscale. It has been successfully applied to reveal the fundamental properties of many nanosystems such as conjugated polymers, carbon nanotubes, quantum dots and proteins [141, 152]. This method removes the ensemble averaging and therefore new insight into the complex electronic structures of individual emitters can be gained. For example Schindler et al. demonstrated that structure property correlations in conjugated polymers derive mainly from chain morphology rather than from the polymer units [17]. Becker et al. reported that much of the spectral complexity associated with conjugated polymers may arise from the chromophores themselves and not from interactions between chromophores typically found in ensemble [153, 154]. Furthermore, other more general phenomena like spectral diffusion or emission blinking of fluorescent organic materials and quantum dots has been observed exclusively by SMS [155, 156, 157].

Although SMS has been an established technique for many years, there are only few spectroscopic reports on the emission properties of single phosphorescent molecules. These compounds are commonly used as emitters in OLEDs (section 2.4). However, many unresolved issues are the subject of current research into attaining better emitters. Especially the long-term stability of phosphorescent materials and photophysical parameters, which control among other things the radiative rate in these compounds, are under intense investigations [34, 92, 151, 158]. The use of SMS can potentially resolve many of these issues. Furthermore, a direct study of the triplet state at the single molecule level, SMS can deliver new understanding of different physical effects. It is possible for example to study the blinking behavior of the triplet state, which has been considered for decades to be the origin of blinking in fluorescent molecules. Because of the efficient phosphorescence the triplet state of organometallic complexes cannot be considered dark and the observation of blinking in this class of molecules must be ascribed to other phenomena. High resolution SMS at cryogenic temperatures has the potential to shed light on details of the electronic structure of these molecules, such as the zero-field splitting (ZFS) of the triplet manifold.

In organometallic complexes the radiative rate of the triplet state is enhanced by spin-orbit coupling (SOC) and the radiative lifetime of the emissive triplet state is shortened from the second to the microsecond time regime [64]. The amount of photons emitted per second is still low compared to what is observed in fluorescent transitions

and therefore there are only sparse studies on single organometallic compounds. Mei et. al studied phosphorescence quenching of single organometallic complexes by molecular oxygen at room temperature [130]. Another group reported on the observation of simultaneous two-photon excited fluorescence and one-photon excited phosphorescence from single Ir(ppy)$_3$ molecules, but without showing spectra of the single emitters [132]. In this work, we will show for the first time that it is possible to detect spectra of individual organometallic compounds at low temperatures and that SMS gives unique insight into complex phenomena that are usually hidden in the ensemble emission of phosphorescent molecules.

We performed our studies on Ir(piq)$_3$, which emits in the red part of the spectrum with a peak wavelength at around 615 nm (see section 3.1.2). While most of this thesis deals with blue emitters we have chosen a red one for these investigations, since background scattering from the substrate on the matrix in which the emitters are dispersed is less severe in the red part of the visible spectrum. We excited the sample at the maximum of the ^{1}MLCT band at 425 nm. The triplet state is then reached by a very fast intersystem-crossing (ISC), which is in the femtosecond time range. Ir(piq)$_3$ has a phosphorescence quantum yield of 26 % and an emission lifetime of the lowest triplet state of 1.1 μs at room temperature [107].

To perform imaging and spectroscopy of single molecules, a home-built wide-field photoluminescence microscope was used as described in section 3.3.2. Ir(piq)$_3$ was dispersed in toluene and then in a highly transparent matrix (Zeonex) at a concentration of 10^{-6} - 10^{-8} mg/ml. The solution was spin-coated at 5000 rpm on a SiO$_2$ covered Silicon wafer, resulting in layer thicknesses of 20 - 50 nm. The sample was then mounted on the cold finger of a helium cryostat.

First, we will demonstrate the detection of individual emitters, which is experimentally challenging due to several reasons. The average number of photons emitted per second is comparable to the noise count rate of the detection. This requires long integration times during which the background noise accumulates and masks the signal. Furthermore, triplet states are known to interact with oxygen resulting in an energy transfer to the triplet state of oxygen and consequently quenching. Experimental proofs of single molecule detection can be obtained by studying images of the sample at different concentrations, e.g. bright spots with a density scaling with concentration. A random succession of bright (emitting) and dark (non-emitting) periods in the PL intensity, the so-called blinking, can be considered as another hint for single molecule

detection [155, 159, 160]. Further characteristics of single molecule emission, e.g. spectral diffusion and polarization anisotropy, shown in section 5.2 and 5.3, confirm our assignment.

5.1.1 Single molecule detection

Figure 5.1 (a) shows a phosphorescence image of a single molecule sample at $5\,\mathrm{K}$. The spin-coated concentration of emitter molecules was 10^{-7} mg/ml. One can clearly
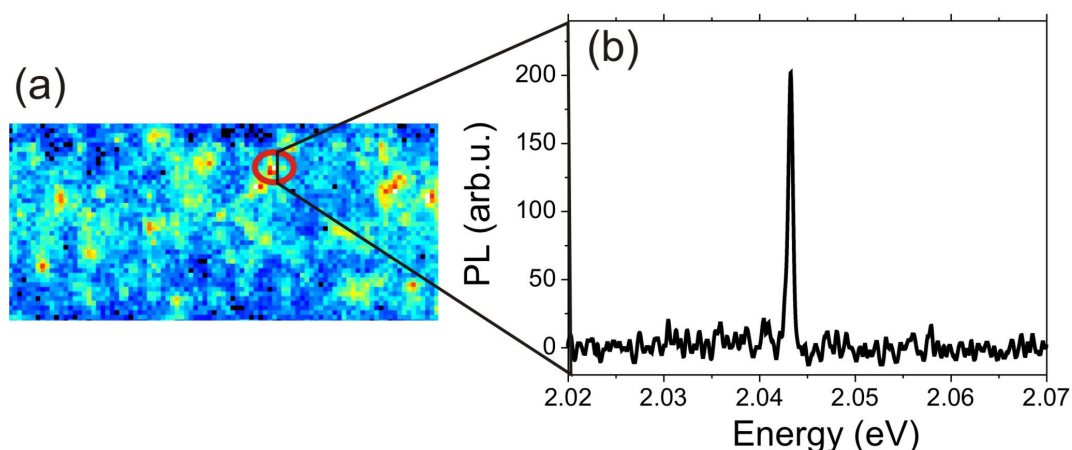
Figure 5.1: *(a) Photoluminescence of single phosphorescent molecules at 5 K. The bright, red spots originate from emission of single compounds. The integration time is 3 s. (b) PL-spectrum of a single spot. The spin-coated concentration of emitter molecules is 10^{-7} mg/ml. The excitation wavelength is 425 nm, detection is accomplished with an integration time of 61 s.*

observe single luminescent points in the image. To further confirm that these emission points originate from single organometallic molecules and not from scattered laser light or impurities, we plot the spectrum of a single spot in figure 5.1 (b). The linewidth of the zero phonon line (ZPL) is below $0.5\,\mathrm{meV}$. Such narrow lines have usually been observed in single molecule experiments where the spectral inhomogeneous broadening could be overcome. For comparison Schindler et al. reported a linewidth of $2.6\,\mathrm{meV}$ and $4.6\,\mathrm{meV}$ at $5\,\mathrm{K}$ for the polymers MEH-PPV and MeLPPP, respectively [161]. In the following chapter we will comment more in detail on the spectral properties of single molecules. Due to the small linewidth and similar intensities of the single spots, we can exclude that this is emission from a cluster of molecules.

5.1.2 Phosphorescence blinking

Blinking of single emitters is characterized by the random succession of emitting and non-emitting periods. Fluctuations in the luminescence intensity with time result from transfer to levels from which the excited electron returns to the ground state without emitting a photon. One well-studied cause of the blinking phenomena in common fluorescent molecules is the ISC from the singlet excited state to the triplet state, which is typically a dark state [155, 159]. As long as the excited triplet state remains occupied, fluorescence does not occur and is interrupted temporarily. Only after decaying from the excited triplet state to the ground state, can the molecule start to absorb and fluorescence again. Therefore, the time constants of the dark periods reflect the lifetime of this state, lying typically in the ms range [155, 157]. Besides fast blinking, so-called long-lived non-emitting periods with off-times on the second timescale have been reported [162]. In the case of fluorescent organic molecules, these long-lived non-emitting periods are mainly explained by reversible formation of non-fluorescent photo-oxidation products, chemical transformation or rearrangements of the molecules and formation of radical anions or cations by electron tunneling from the emitter triplet state to an acceptor level usually in the polymer matrix [130, 156].

With the use of phosphors we can now make the triplet state visible and attain new insights into the blinking of molecules. When investigating emission from the excited triplet state, we expect to only observe a blinking of the emitter intensity on the long-time scale. Unfortunately, due to the long integration time of $3\,\mathrm{s}$, it is not possible to detect potentially fast blinking on the millisecond timescale.

Figure 5.2 shows the phosphorescence intensity of two $\mathrm{Ir(piq)_3}$ molecules (A and B) as a function of the illumination time. The integration time is $3\,\mathrm{s}$ for one spectrum with a total time trace of $300\,\mathrm{s}$. One can clearly observe a random succession of bright and dark periods for both molecules. As mentioned before, blinking of the PL intensity is an intrinsic feature of single molecule emission. The off-times of emission vary for both emitters in the range of $3\,\mathrm{s}$ to $30\,\mathrm{s}$ and on-times from $3\,\mathrm{s}$ to $40\,\mathrm{s}$.

The sudden end of the photoluminescence emission of molecule B can be ascribed to irreversible photobleaching and is a consequence of a photochemical reaction. This effect has been reported also for single fluorescent molecules [157, 163].

The observation of a blinking behavior of phosphorescence intensity confirms that the detected emitting spots can be assigned to the emission of single molecules. In
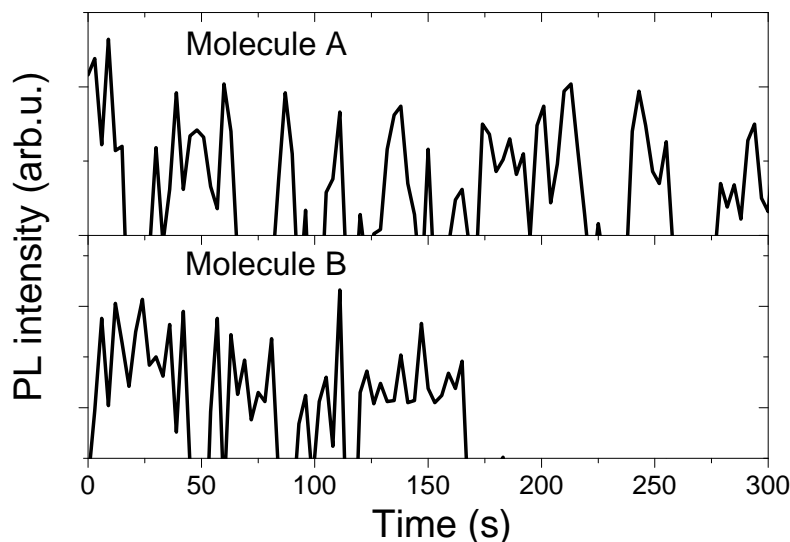
Figure 5.2: *Phosphorescence intensity of two single Ir(piq)₃ molecules (A and B) as a function of the illumination time. The integration time is 3 s.*

ensemble emission one detects a vast number of single emitters and it is improbable that all emitters show a non-emitting period at the same time. In the next section we will take a closer look at the electronic structure of these molecules by high resolution low temperature SMS.

5.2   Phosphorescence spectroscopy of single molecules

In the previous section, we demonstrated the direct observation of single phosphorescent molecules. Here, we take a closer look at the spectral properties of single $Ir(piq)_3$ molecules at 5 K. We report very narrow linewidths of 0.3 meV of single molecule spectra. Summation of these spectra leads to a spectrum comparable to the ensemble emission. In addition, polarization dependent measurements show linearly polarized emission, which further confirms our claim of single molecule detection.

5.2.1   Spectra of single molecules

Figure 5.3 shows the spectrum of a single $Ir(piq)_3$ molecule at a temperature of 5 K, compared with its ensemble spectrum at the same temperature. One can clearly ob-

serve a much smaller linewidth of the single molecule ZPL with respect to that of the ensemble, reflecting the advantage of SMS.
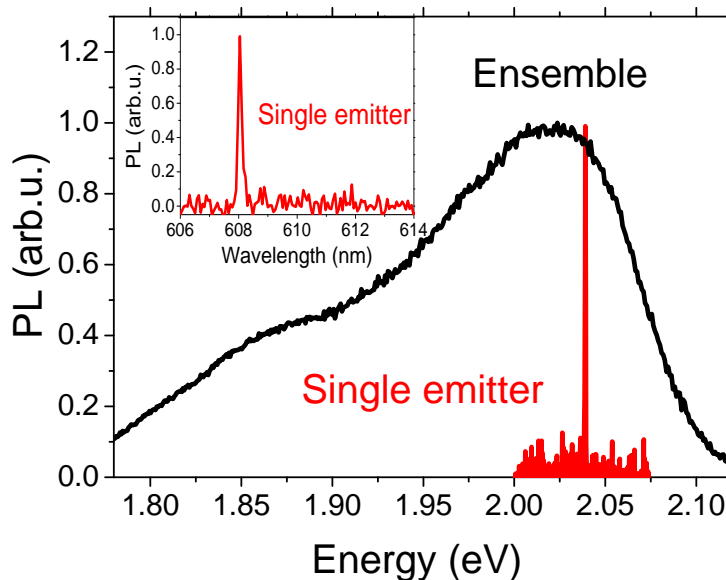
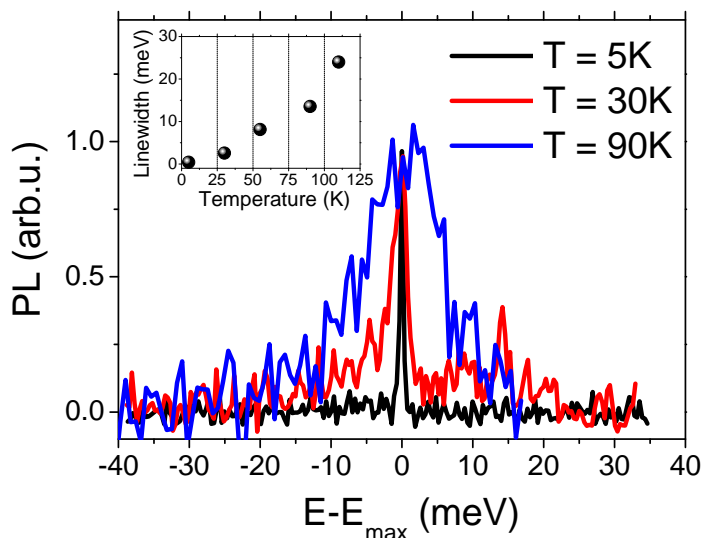**Figure 5.3:** *Phosphorescence spectrum of a single phosphorescent complex compared to an ensemble emission spectrum at a temperature of 5 K. The investigated material is Ir(piq)$_3$. The inset shows the spectrum of the same single emitter on a smaller spectral interval.*

In principle, the homogeneous linewidth Γ_{hom} of the ZPL should reflect the dephasing time, T_2, of the excitation in the molecule that is being observed. The lifetime of Ir(piq)$_3$ is 1.1 μs, which according to equation $\Gamma_{hom} \geq 2\hbar/T_2$ should result in a linewidth of 1 neV. The larger linewidth observed in our experiment, though much smaller than the one observed in colloidal quantum dots or conjugated polymers, is broadened by spectral diffusion. Spectral diffusion will be discussed in section 5.3.2. In this phenomenon the energy of the transition fluctuates in time resulting in a broadened transition after the spectrum acquisition time. For comparison the 0.3 meV linewidth of Ir(piq)$_3$ is almost an order of magnitude smaller than in MEH-PPV ($\approx$ 2.6 meV), even though the acquisition integration time is longer [97]. Additionally, single organometallic complexes should be considered as a more ordered system than polymers. This is expected because of the smaller size of these molecules, which prevents many and extended interactions with the environment [164].

At higher temperatures the homogeneous linewidth increases significantly due to the interaction with phonons. In particular, the overall dephasing time decreases dramat-

Figure 5.4: *Phosphorescence spectra of single molecules at different temperatures, where the spectral position relative to the maximum of the ZPL E_{max} is plotted. The inset shows the temperature dependence of the linewidth.*

ically and additionally, spectral diffusion phenomena are expected to increase, resulting in an increase in the linewidth. While at a temperature of $T = 5\,K$ we measure a linewidth of $0.3\,meV$, this is increased to $24\,meV$ at $T = 110\,K$ (figure 5.4). For temperatures above $110\,K$ the signal-noise ratio is too small to obtain reliable measurements of the linewidth.

5.2.2 Statistics on single molecule spectra

As discussed in the previous paragraph, SMS can overcome the problem of inhomogeneous broadening. This is demonstrated again in the histogram of figure 5.5. Superimposed as a black line is the spectrum of the ensemble recorded for the same experimental conditions as the single molecule sample. The shape of histogram for spectra of single emitters show a blue-shifted maximum compared to the ensemble spectrum. This is caused by the fact that in ensemble the excitation is transferred within the Gaussian density of states to molecules on the low energy side. Single molecules are isolated from each other and therefore, the excitation is localized on the molecule and cannot be transfered. The energetic distribution of the histogram is narrower with respect to the full width at half maximum (FWHM) of the ensemble spectrum. This can be caused by aggregation effects and/or interaction of emitters in the ensemble. These effects are not present in the case of single emitter. The disorder of the sum of the ZPL is smaller for phosphorescent complexes than for isolated polymer chains [17]. Small molecules are a more defined system than for example polymers and therefore
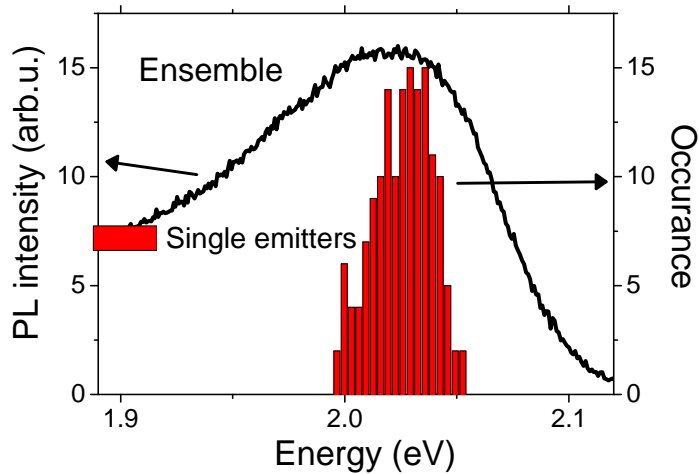
Figure 5.5: *Comparison of the sum of the ZPL of about 130 single molecule spectra with the spectrum of an ensemble measurement of Ir(piq)$_3$ at 5 K.*

do not show pronounced torsion and folding as do polymers. The fluctuation of the ZPL originates from a slightly different dielectric environment of each single molecule, which results in different emission energies. Another possible reason could be small variations in the structure.

5.2.3 Polarization anisotropy of emission

Most single molecules have a transition dipole which is oriented in a specific direction in the molecular structure. The orientation is mainly determined by the electronic structure and the symmetry of the orbitals involved in the transition. For a fixed single molecule it is possible to observe a $\cos^2(\vartheta)$ modulation in the PL intensity as a function of rotation between the polarizing element and the transition dipole moment. As a consequence, polarization dependent measurements can be used to determine the relative position and orientation of the transition dipole moment of single emitters [144, 165]. For that purpose, one defines the polarization anisotropy P as

$$P = \frac{I_{max} - I_{min}}{I_{max} + I_{min}}, \tag{5.1}$$

where I_{max} and I_{min} are maximum and minimum PL intensity extracted by a complete rotation of the emission polarization angle ϑ. P can adopt values between 0 and 1, where 0 corresponds to an isotropic emission and 1 to a linearly polarized emission.

Figure 5.6 (a) shows a sequence of single molecule spectra at different emission polarization angles of a single Ir(piq)$_3$ molecule. The x-axis corresponds to the polarization
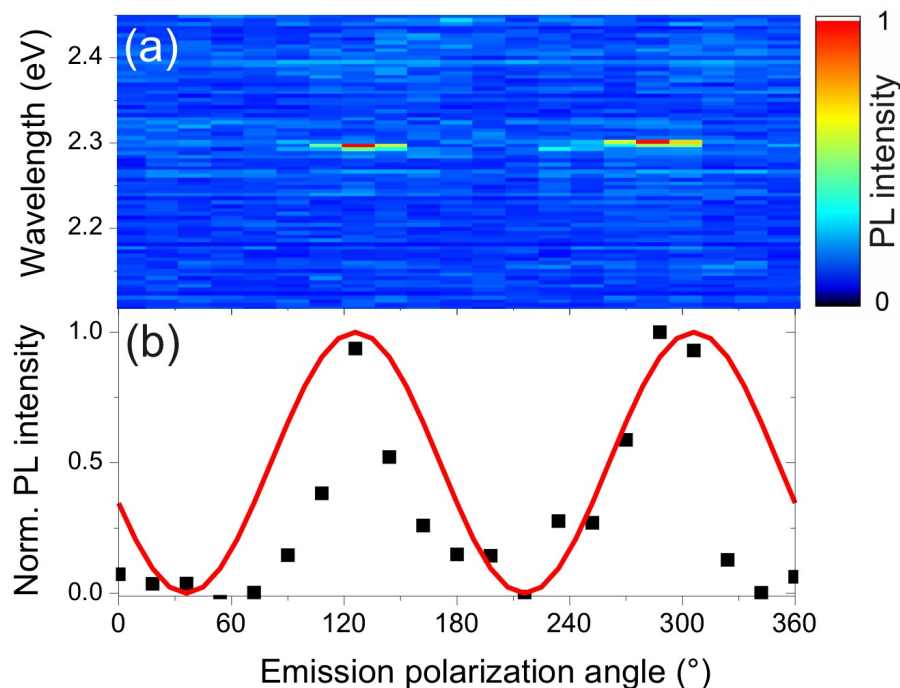
Figure 5.6: *(a) Sequence of single molecule spectra at different emission polarization angles of a single Ir(piq)$_3$ molecule. The x-axis corresponds to the polarization angles, the y-axis to the wavelength and the color to the PL intensity. The integration time per spectrum was 33 seconds at a temperature of 5 K. (b) Linearly polarized emission with a high degree of polarization anisotropy P, reaching 1. The red curve is a fit according to a $\cos^2(\vartheta)$-function.*

angles, the y-axis to the wavelength and the color to the PL intensity. In the detection path we used an electrically controlled polarizer, which is rotated in discrete steps from 0° to 360°. Excitation with circularly light was obtained by inserting a $\lambda/4$-plate in the beam path of the excitation laser. One can clearly observe a dependence of the phosphorescence intensity on the emission polarization angle. In figure 5.6 (b) the integrated PL intensity is plotted against the emission polarization angle. The data can be fitted with a $\cos^2(\vartheta)$-function, describing a vectorial coupling. For a single Ir(piq)$_3$ molecule we report a linearly polarized emission (P $\approx$ 1), which is typical for single isolated small molecules [164]. The non perfect matching between the fitting curve and our data is presumably due to fluctuations in the emission intensity in time (blinking).

In ensemble emission such a polarization dependence is not observable, since each molecule has a different orientation, resulting in a constant PL intensity as a function of emission polarization angle. Thus, a linearly polarized emission is a strong criterion for a single emitter [165].

Summarizing, in this section we have shown that we can detect single phosphorescent emitters. This is proven by the observation of very narrow spectral linewidths with respect to the ensemble and the polarization dependent measurements. In the next section, we will show that we can observe emission from two states for some single molecules. We will ascribe this effect to the emission from triplet substates.

5.3 Probing the zero-field splitting in single organic molecules

We report the observation of spectral diffusion in the ZFS of an iridium complex by low temperature SMS. The ZFS is observed by monitoring the emission lines of two energetically separated triplet sublevels. This allows us to deduce a histogram for the amount of ZFS for different single emitters. Interestingly, the ZFS shows spectral diffusion, a phenomenon never observed so far.

5.3.1 Detection of the zero-field splitting

Figures 5.7 (a) and (b) show the PL spectra of two single Ir(piq)$_3$ molecules at 5 K. In contrast to the single molecule spectra reported above, we observe two peaks for these molecules. Out of these more than 400 molecules that we observed 5 - 10% of them showed these emission features. The energetic separation of the two peaks varies between 1.40 meV and 2.12 meV. Interestingly, the relative intensity of these peaks fluctuates, e.g. in figure 5.7 (b) the peak at lower energy is higher in intensity. This rules out the possibility of it being a vibronic progression of the peak at higher energy. We attribute the two features to emission from different substates of the excited triplet state. Experiments shown in the following further affirm our assignment.

Each triplet state splits up into three substates (I, II and III), which differ from each other by their relative spin orientations. The energetic separation of the triplet sublevels in the absence of an external magnetic field is termed ZFS. As described in section 2.2.3, in organometallic complexes the amount of ZFS depends mainly on the magnitude of SOC of the emitting triplet state to higher lying states. Yersin et al. showed for a series of organometallic complexes that the ZFS represents a valuable parameter for predicting their important physical properties [64]. Thereby, a high magnitude of ZFS of the emitting triplet state corresponds to an effective SOC and
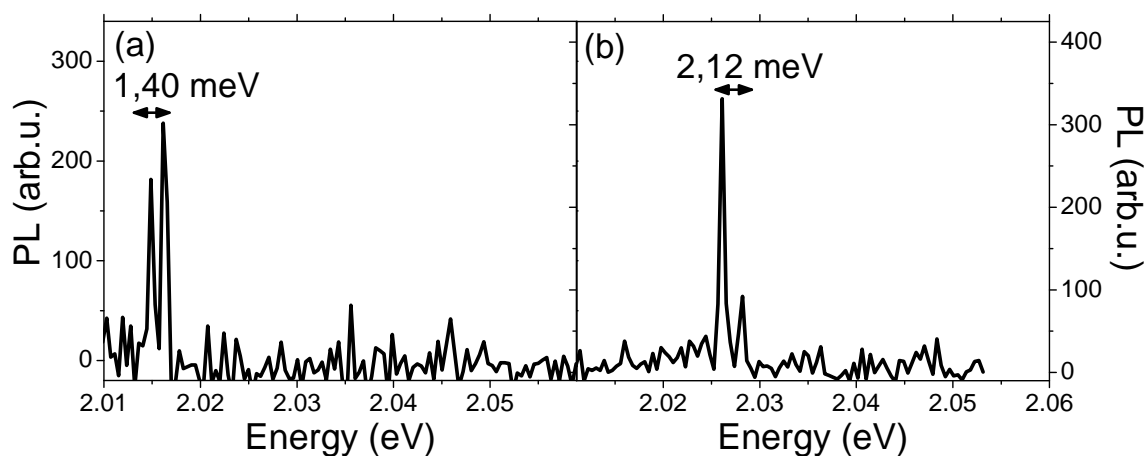
Figure 5.7: *Single molecule spectra of two emitters showing two emission peaks, originating from two different substates of the lowest triplet state. Measurements were performed at a temperature of $T = 5\,K$. While in (a) the intensity of the peak at higher energy is higher, we detect in spectrum (b) the opposite case.*

a high radiative rate. The values reported for the ZFS are between $0.01\,meV$ and $26.16\,meV$ [63, 64, 80, 166].

The photophysical properties of the three individual substates, like the radiative decay rate, population and relaxation dynamics can differ dramatically from each other. By site-selective spectroscopy and TD-DFT calculations it was shown that the low energetic triplet substate I is typically a relatively pure triplet state and the transition from this substate to the ground state is largely forbidden [80, 166, 168, 167]. For example, for the green emitter $Ir(ppy)_3$ a nearly three orders of magnitude longer radiative lifetime of the lowest substate compared to the energetic highest one is reported (section 2.2.3). Due to this long lifetime, we presumably observe only emission from the energeticly higher substates II and III, which typically have comparable radiative
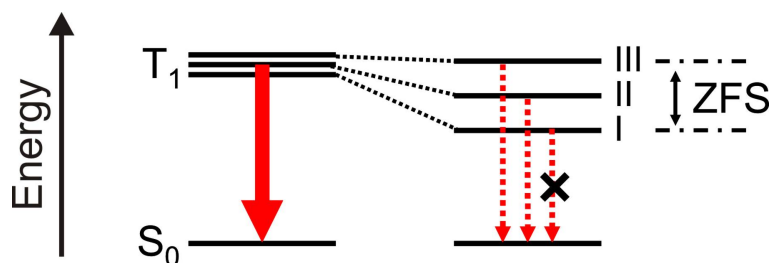

Figure 5.8: *Each triplet state splits up into three substates, which differ from each other mainly by their relative spin orientations. Typically, the transition from lowest energetic substate I to the ground state is largely forbidden [80, 167].*

rates.

5.3.2   Spectral diffusion of the zero-field splitting

Spectral diffusion of single isolated chromophores is a universal feature in several molecular and atomic systems. It has been observed in organic molecules, quantum dots, conjugated polymers, carbon nanotubes and proteins [152, 163, 169]. Spectral diffusion becomes critical when studying dephasing phenomena of excitons and in understanding the energy transfer of single multichromophoric systems. The origin of spectral diffusion has been so far ascribed to extrinsic effects originating from fluctuations in the surrounding of the chromophore or on its surface in the case of quantum dots. Indeed, single molecules in well ordered crystalline matrices or quantum dots in a defect-free wetting layer show transition linewidths approaching the intrinsic dephasing time of the exciton. Dynamic fluctuations in the configuration of the nuclei constituting the molecular entity are potentially present upon photoexcitation. However, the role of these fluctuations in determining the extent of spectral diffusion is difficult to estimate and discern from the extrinsic phenomena mentioned above. Here, we report the first observation of spectral diffusion in the ZFS of an iridium complex by low temperature SMS. The ZFS is observed by monitoring the phosphorescence lines of two energetically separated triplet sublevels.

For investigations of the time evolution of the ZFS we collect a sequence of single molecule spectra at a time resolution of 30 seconds. Figure 5.9 (a) shows such a sequence for a single $Ir(piq)_3$ molecule at a temperature of $T = 5\,K$. The x-axis corresponds to the time, the y-axis to the wavelength and the color to the PL intensity. In (b) the single emission spectra of the trace are summed into a single spectrum. The overall trace time is 12 minutes. Besides variations in the intensity of the two peaks, we observe spectral diffusion of the two phosphorescence peaks at the same time, another strong indication that they originate from one single emitter. In general, spectral diffusion effects have been seen before in SMS of organic molecules at low temperature [152]. Schindler et al. performed a detailed study of spectral diffusion effects in polymers [17]. They showed that theses fluctuations arise from exciton migration between chromophores on a single chain and from the jitter of the single chromophore unit itself, which might be linked to the presence of charges on and around the polymer chain or from slight structural rearrangements of the polymer chain or side groups. Besides the well known spectral diffusion of optical transitions, we demonstrate here spectral diffusion in the ZFS of a
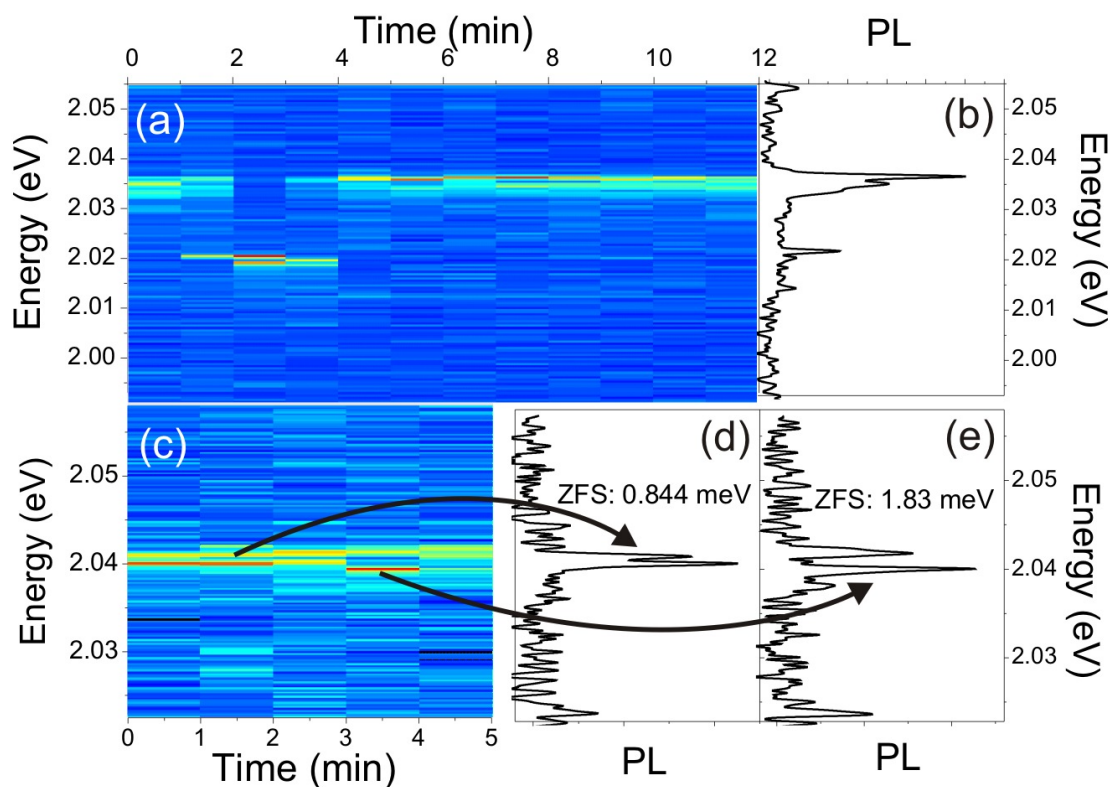
Figure 5.9: *(a) Sequence of PL spectra of single molecules at a time resolution of 30 seconds for a single Ir(piq)$_3$ molecule at a temperature of T = 5 K. The x-axis corresponds to the time, the y-axis to the wavelength and the color to the PL intensity. (b) Sum of the single spectra shown in (a). (c) Sequence of PL spectra of single molecules at a time resolution of 30 seconds for a single Ir(piq)$_3$ molecule. We observe variations of the amount of the ZFS during the measurement, which are shown in the emission spectra in figure (d) and (e).*

single phosphorescent molecule. In figure 5.9 (c) we plot a sequence of PL spectra of single molecules with a time resolution of 30 seconds. We clearly observe a change in the ZFS during the measurement (spectra (d) and (e)). In the first spectrum the ZFS is 0.84 meV, and it changes after a few minutes to a value of 1.83 meV. Therefore, the ZFS of the emitting triplet state of single organometallic complexes is not a constant in time.

We have studied more than 60 single molecules showing a ZFS and plotted the distribution of their ZFS in figure 5.10. The distribution shows a maximum at 1 meV and a maximum value of 2.4 meV. Such values are consistent with optical experiments on organometallic complexes dispersed in crystalline matrices [63, 72, 166]. Yersin et al. measured by site-selective spectroscopy a value of nearly 4 meV for an Ir(piq)$_3$ ensemble sample, higher than the maximum value we detected in SMS [64]. This
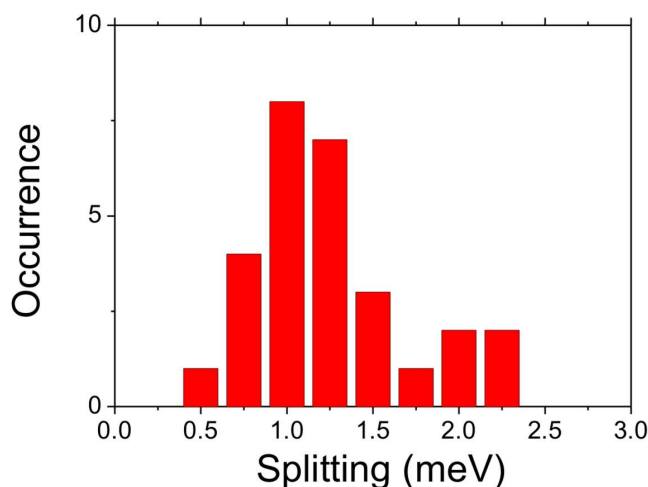
Figure 5.10: *Histogram of the energetic distribution of the ZFS for about 60 single Ir(piq)$_3$ molecules.*

discrepancy between the single molecule and the ensemble data can have following possible explanations: firstly, while in ensemble it is likely that one observes all the three triplet substates, we detect only two substates. Since the splitting between I - II and II - III is different, because of asymmetry, single values might differ. Secondly, the employed matrix material can have an influence on the amount of ZFS as recently revealed by Rausch et al. [158].

To discuss the fluctuations and energetic distribution in the ZFS it is necessary to recall the physical parameters causing the splitting and its magnitude. As mentioned above, in the absence of an external magnetic field the separation of triplet substates is determined by the effectiveness of SOC to higher lying states (equation 2.18). Therefore, fluctuations in the ZFS are caused by variations of the effectiveness of SOC. One should note that variations in the magnitude of the ZFS can also occur for one single emitter during the measurement (figure 5.9 (c)). The SOC Hamiltonian H_{SO} has a strong dependence on the distance between the excited electron and the nucleus (equation 2.17). We expect that fluctuations of this distance, probably as a consequence of small changes in the molecular geometry induced by the environment or the excited state, cause the observed energetic distribution the ZFS.

In an alternative explanation, the amount of ZFS can also be correlated to the MLCT character of the emitting triplet substate, where the MLCT character reflects the d-orbital contribution to the transition (chapter 2.2). It is known in literature that MLCT states are typically more sensitive to environmental fluctuations than ligand-

centered states [58, 170]. Therefore, slight changes in the local environment of a single emitter presumably lead to shifts in the energies and splitting of the metal d-orbitals. This might induce changes in the MLCT character and therefore the strength of SOC to the emissive triplet state. These changes are correlated with fluctuations in the ZFS (section 2.2.2). Recently Rausch et al. demonstrated by site-selective, high-resolution spectroscopy the observation of different photophysical properties of molecules located at different sites [158]. Their investigations show that the properties of triplet emitters can indeed be affected by differences in the local environments.

Fluctuations in the ZFS of single emitters are exclusively detected by SMS, showing the importance of modifications in the SOC. According to our results, the photophysical properties of the individual substates of a triplet state can differ from molecule to molecule. We expect that decay rates and emission quantum yields also show strong fluctuations on the single molecule level. Variations in the intensity ratio of the emission peaks (figure 5.7) can be caused by different effects: changes in the spin-lattice relaxation between the substates, which can lead to changes in the occupation probability; fluctuations of the effectiveness of SOC to the individual substates; and temperature fluctuations in the sample.

These findings are of particular interest for the design of phosphorescent complexes. Optimizing the effectiveness of SOC together with the ΔE_{ST} discussed in chapter 4 in such compounds can lead to higher radiative rates of the emitting triplet state. A shorter phosphorescence lifetime can help to decrease the residence time of potentially unstable excited states and to reduce processes detrimental to the efficiency of an OLED, such as exciton charge-carrier quenching or triplet-triplet annihilation [105, 34]. However, for a complete understanding of the parameters which influence the radiative rate in phosphorescent complexes, additional studies on the single molecule level, possibly including time resolved measurements, are needed.

5.4   Summary

In summary, we report on the first observation of PL spectra of single phosphorescent complexes at cryogenic temperatures, providing new insight into the complex structure of these molecules. We detect narrow linewidths of only 0.3 meV and additionally a blinking behavior of single luminescent spots. Polarization dependent measurements confirm the detection of spectral features of single organometallic complexes. Further-

more, we report the occurrence of two peaks representing the ZFS of two emitting triplet substates. Remarkably, the emission of these two substates shows spectral diffusion in the splitting. The spectral diffusion of this intrinsic molecular property is ascribed to modifications in the molecular geometry or fluctuations in the local environment of the emitter. Furthermore, we detect fluctuations in the energetic distribution of the ZFS, which are expected to be caused by variations of the effectiveness of SOC to the emitting triplet state. These findings are of general importance for the understanding of the nature of the excited triplet state and pave the way to the application of SMS in studying phosphorescent molecules for OLEDs.

Chapter 6

Triplet exciton dissociation in the presence of an electric field

In the previous chapters we analyzed the parameters influencing the radiative rate of phosphorescence in organometallic complexes. The final aim of that study is to achieve fast emitters, where recombination competes with the rates of exciton charge-carrier or triplet-triplet annihilation. In this chapter, we present a study of the electric field induced quenching on the phosphorescence intensity of a deep-blue triplet emitter dispersed in different host materials. In other words, we show the importance of emitter/host combination and not only the emitter itself. While other quenching processes occurring in OLEDs, like triplet-triplet exciton annihilation and triplet-polaron quenching, are well documented, electric field induced quenching has been only partially investigated, sometimes with diverse conclusions. Such an effect appears to be significant for deep-blue emitters, where operating voltages are higher than for green and red. In this chapter we will first investigate the steady state electric field induced quenching in host/guest systems. The hosts are characterized by a higher triplet excitonic level with respect to the emitter, ensuring efficient energy transfer and exciton confinement, whereas they differ in the HOMO alignment, forming type I and type II host/emitter heterostructures. Additional, we study the effect of the emitter concentration on the quenching behavior. To clarify the mechanism involved in the emitter PL quenching we perform time resolved measurements, in the presence and absence of the field.

6.1 Steady state electric field induced quenching

In the previous chapters we mainly discussed the properties of the emitter molecules. However, in OLEDs the emission layer typically consists of a host/guest system, where the emitter is doped into a host material (see section 2.4). In the following we present a study of the electric field induced quenching on the phosphorescence intensity of a deep-blue triplet emitter dispersed in different host materials and of thin films of the pure emitter.

6.1.1 Quenching in host/guest systems

When organic molecules or polymers are used as hosts, the large exchange interaction ($\approx 0.8\,\mathrm{eV}$) typical of these materials [39, 171, 172], requires high bandgaps ($> 3.6\,\mathrm{eV}$) to assure triplet exciton confinement on blue phosphors (emission energy $\approx 2.8\,\mathrm{eV}$). Such large bandgaps can necessitate high operating voltages, in order to reach the current densities ensuring high external efficiencies. A second viable approach considers the use of molecules with an energy gap similar to the emitter. This could lead to a good matching of levels with the HOMO and LUMO of the p-type and n-type transport layers (see section 2.4). However, the triplet excitonic level needs still to be maintained high to effectively confine triplet excitons on the emitter molecule.

An elegant way for obtaining hosts with such characteristics is the use of organometallic molecules, where the mixing of singlet and triplet states lead to a decreased exchange interaction [34, 64]. In this situation, triplet confinement can be reached without the need for a wide electronic bandgap. Such an approach has been recently exploited for red emitting OLEDs resulting in lower turn on voltages and higher efficiencies at low current densities [134]. However, in contrast to this beneficial effect the use of host molecules with a narrower HOMO-LUMO gap can lead to type II energy level configurations between the emitter and the host, potentially impacting the radiative recombination of excitons during device operation at high brightness [134, 173]. We remind that type I, type II terminology, originally introduced for inorganic semiconductor heterostructures, refers to molecular heterojunctions, differing in the alignment of HOMOs and LUMOs. In the case of both the HOMO and LUMO of one material lying inside the ones of the other, one has a type I system. In type II, both the HOMO and LUMO are at higher energy with respect to the corresponding orbitals of the other material.
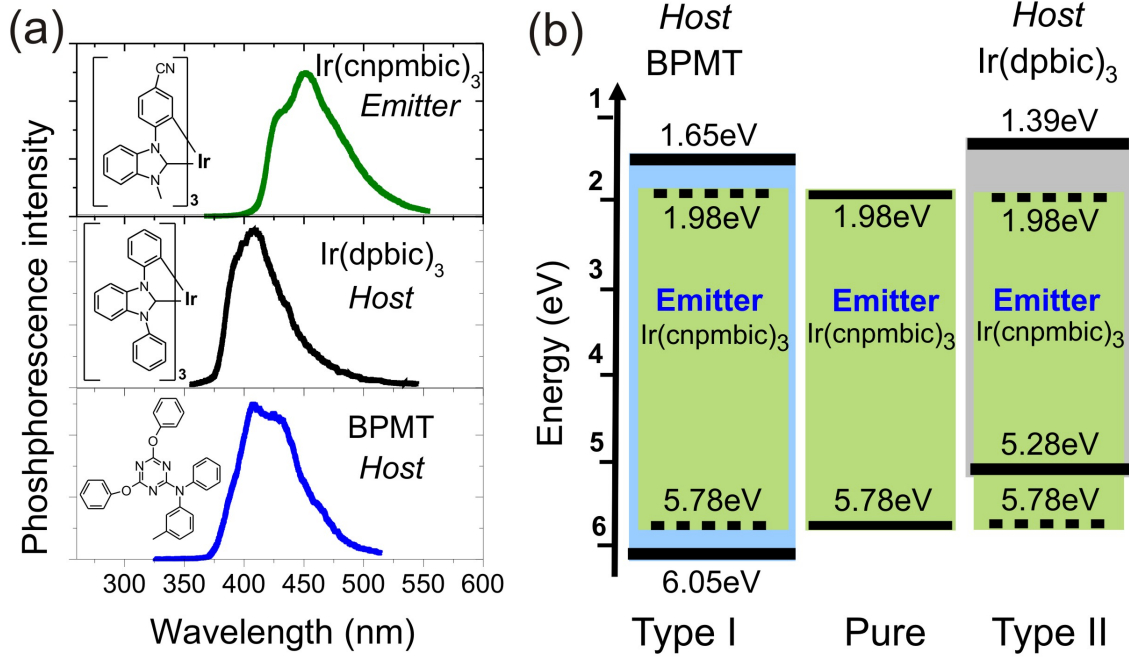
Figure 6.1: *(a) Phosphorescence spectra of the emitter Ir(cnpmbic)₃ and the two hosts Ir(dpbic)₃ and BPMT. All the spectra were obtained with the molecules dispersed in a thin film of PMMA. While the spectra of Ir(cnpmbic)₃ and Ir(dpbic)₃ were recorded at room temperature, the one of BPMT at T = 5K. Excitation was performed at 337 nm. The insets show the chemical structures of the compounds. (b) Energy level diagram of the samples used to investigate electric field quenching. The HOMO and LUMO levels for the different materials are indicated. Solid lines are for the host, the dashed lines represent the levels of the dispersed emitter molecules. When the emitter molecule Ir(cnpmbic)₃ is dispersed in the host BPMT a type I heterostructure is formed. In the case of the pure emitter film molecules with the same HOMO and LUMO are closed packed. For Ir(cnpmbic)₃ in Ir(dpbic)₃ a type II heterojunction is formed. The HOMO and LUMO levels were extracted from DFT calculations.*

Here, we present a new series of molecular hosts with the goal in mind of under-standing the influence of type I and type II host/emitter energy level alignment on the electric field induced quenching. Figure 6.1 (a) shows the phosphorescence spec-tra of the three molecular compounds considered in our experiments, together with the chemical structures in the respective insets. In the top panel the spectrum of the iridium complex Ir(cnpmbic)₃ shows emission in the deep-blue region of the visible spectrum peaking at 450 nm. As mentioned above, the high quantum efficiency ($\Phi_{PL} \approx$ 80%) and short phosphorescence lifetime ($\tau_T < 10\,\mu$s) make this material an ideal emit-ter in the deep-blue [34]. Ir(cnpmbic)₃ will be hereafter referred as emitter and dis-persed at low concentration (7 % w/w) in various hosts. The host materials Ir(dpbic)₃ and 2,4-Bis(phenoxy)-6-(3-methyldiphenylamino)-1,3,5-triazine (BPMT) are reported in the middle and lower panel of Figure 6.1 (a), respectively. The phosphorescence

spectrum of BPMT, a namely fluorescent compound, was observed exclusively by low temperature time-gated spectroscopy (section 3.3.1). While both the energy levels of host triplet excitons are higher with respect to the one of the emitter (Fig. 6.1 (a)), the alignment of the HOMO levels differs, creating type I and type II configurations in the case of BPMT and Ir(dpbic)$_3$, respectively as seen from the spectra. Our material combinations are, therefore, ideal for efficient triplet exciton transfer and confinement on the emitter, while potentially showing diverse behaviours for the dynamics of one type of charge carriers, i.e. holes. The exciton confinement is verified by the detection of exclusively emitter PL, upon excitation of the host/emitter films. This demonstrates that despite the type II configuration, excitons on the emitter are capable of emitting light, being Coulomb stabilized by the strong binding energy in the triplet exciton. Figure 6.1 (b) shows in addition the energy levels for a sample made of only Ir(cnpmbic)$_3$ molecules, in which the emitter can be considered as its own host.

In order to study the modulation of the emitter phosphorescence intensity upon the application of an electric field, we prepared sandwich structures, where the emitter is dispersed in the hosts at low concentration (7 % w/w). The sample preparation is described in detail in section 3.2.2. The SiOx layers and a reverse bias configuration assured a low current density, not exceeding $1\,A/m^2$ at $2\,MV/cm$. This was necessary to study the effect of the electric field in the absence of carrier injection and therefore exciton-polaron quenching. This value of the current density can be compared with several reports that show how exciton-polaron quenching starts to be relevant for larger currents [105, 135]. In addition to the two host/emitter samples (type I, type II), thin films of pure and dispersed in polymethylmethacrylate (PMMA) were studied, for a total of four samples. Note that PMMA represents an isolating host material with a
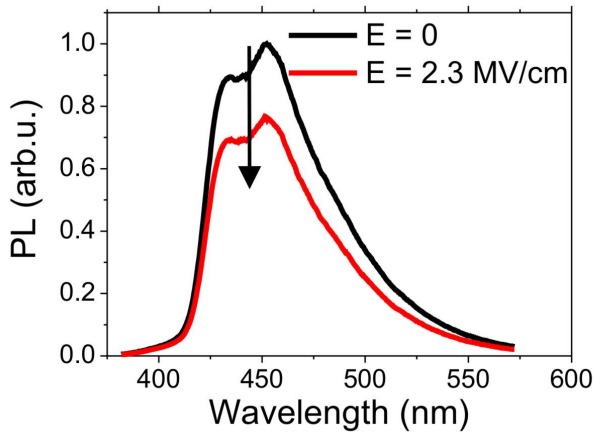
Figure 6.2: *PL spectra of Ir(cnpmbic)$_3$ doped in Ir(dpbic)$_3$ in the presence (red solid line) and absence (black solid line) of an external electric field of 2.3 MV/cm. Excitation is performed at 337 nm.*
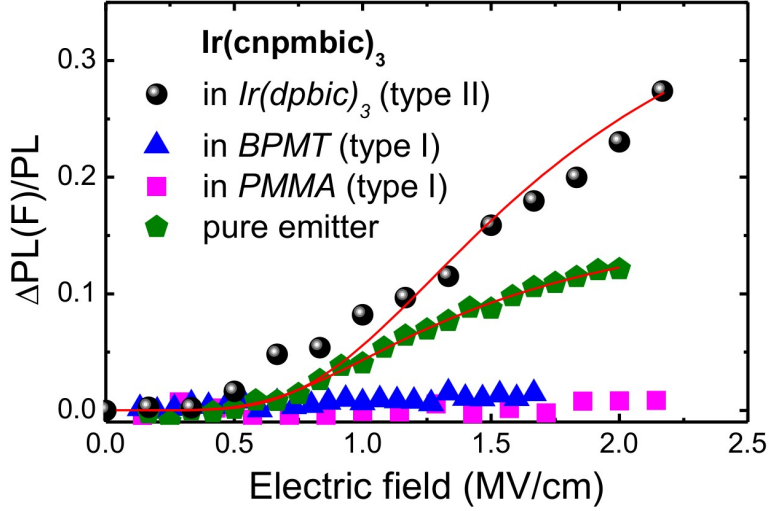
Figure 6.3: *Field induced relative quenching (Δ PL(F)/PL) plotted as a function of the applied electric field. The data points are obtained integrating on the PL spectrum of the emitter molecule (Ir(cnpmbic)$_3$). Four different samples are reported in which Ir(cnpmbic)$_3$ is dispersed in: PMMA (type I (magenta squares)), BPMT (type I (blue triangles)), Ir(cnpmbic)$_3$ (pure emitter (green hexagons)) and Ir(dpbic)$_3$ (type II (black dots)). The red solid line represents a fit according to the Onsager model. See text for details.*

very large bandgap and therefore creating a type I alignment.

Figure 6.2 shows an example of PL spectra for the type II combination, in the presence (red line) and absence (black line) of the external electric field. It is possible to clearly distinguish a reduction of the PL intensity upon application of the electric field.

In figure 6.3 the relative field induced changes in the Ir(cnpmbic)$_3$ PL intensity ([PL-PL(F)]/PL $= \Delta$ PL(F)/PL, excited at 337 nm, as a function of the electric field amplitude, F, is shown. The relative changes were calculated integrating the intensity on the overall emitter PL spectrum. The data points summarize the experiments for the four previously described samples.

While a negligible quenching (ΔPL(F)/PL $< 2\%$) is observed for the type I configuration (blue triangles), a quenching up to 25% is observed for the type II (black dots) at 2 MV/cm. This apparently high electric field corresponds to an applied voltage of 25 V on a ≈ 125 nm thin film, an experimental configuration potentially reached in OLEDs when operated at high brightness [64], or in the presence of charge accumulation at the interfaces of thin emitting layers [123]. The red lines in figure 6.3 represent

fits according to the Onsager model. This modeling will be discussed below.

6.1.2 Effect of emitter concentration

The thin films obtained from the pristine emitter (green hexagons in figure 6.3) shows a pronounced quenching up to 12% at $2\,MV/cm$. This result is similar to what is observed in films of pristine conjugated polymers, where intrachain excitons can be separated in electrons and holes localized onto two adjacent conjugated segments [122, 174]. An exciton separation is promoted by the close contacts of molecules as the absence of PL quenching in the curve of the sample $Ir(cnpmbic)_3$/PMMA (pink squares) suggests. To address further this issue, we produced structures containing a different amount of $Ir(cnpmbic)_3$ in PMMA. Figure 6.4 shows the concentration dependence of the electric field induced quenching for these different samples. The data show a clear trend between the amount of quenched PL and the emitter concentration. Effective quenching starts at concentrations beyond 20%. Therefore, emitter molecules which are close packed or aggregated give rise to exciton separation and PL quenching in the presence of an external electric field.
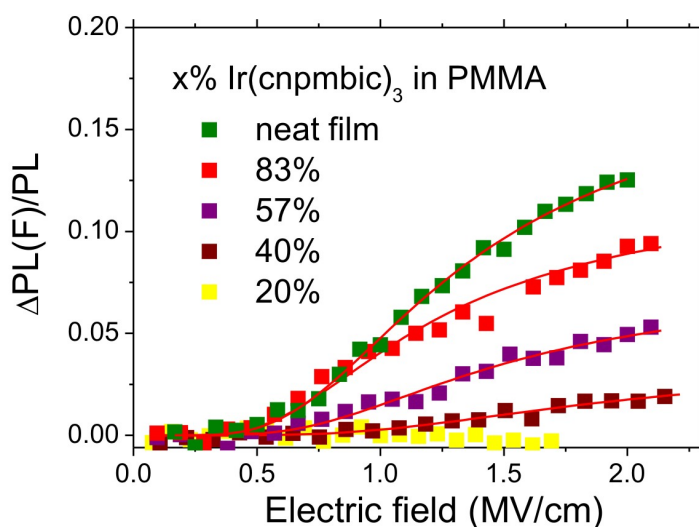
Figure 6.4: *Electric field induced quenching for Ir(cnpmbic)$_3$ dispersed in PMMA. Different weight ratios were investigated. 20 % (yellow), 40 % (brown), 57 % (purple), 83 % (red) and 100% (green). The red line represents the fit to the data according to the Onsager model.*

At this point we want to remind that exciton dissociation is usually described by a two-step process (section 2.1.2). The first step is the initial separation of the electron and hole resulting in the formation of polaron pairs (PPs) and the subsequent generation of free polarons [175]. The first is limited by the exciton binding energy which

is in the range of 0.3 - 1 eV for organic molecules [24, 25]. In the presence of loosely bound PPs (pristine emitter), the exciton dissociation is likely to be the limiting step.

The quenching curves in figure 6.4 have been modeled according to the Onsager model for the dissociation of Coulombically bound electron hole pairs (section 2.1.2, equation 2.10). The red curves superimposed on the data points show the results of the fitting. The data are well described by the Onsager model from which it is possible to extract the initial dissociation probability Φ_0 and the radius of weakly bound pairs r_0 (figure 6.4). The values obtained for the fit of the different samples are listed in table 6.1. Clearly, high emitter concentrations facilitate the initial probability of PPs formation whereas low concentrations hamper this process.

	$\Phi_0[\%]$	r_0 [nm]
40 % Emitter in PMMA	0.05	1.88
60 % Emitter in PMMA	0.06	2.51
80 % Emitter in PMMA	0.14	3.17
100 % Emitter	0.22	2.7

Table 6.1: *Values for the initial probability of formation of PPs, Φ_0, and for the distance of the PPs, r_0, obtained for fitting the experimental data to the Onsager model using the dielectric constant $\epsilon_r = 3.5$ and a temperature of $T = 296\,K$.*

We note that the relative quenching observed in figure 6.3 and 6.4 is not linear with the applied field but tends to saturate at 1.75 MV/cm for pure emitter and type II. While the absence of a linear behaviour excludes space charge effects, the saturation is a typical feature explained by the Onsager model, which occurs when nearly all PPs are separated. We also have fitted the quenching for type II extracting an average value for the PPs radius of 2.16 nm (figure 6.3). This value of the radius and the ones presented in table 6.1 are consistent with electron and holes localized onto two adjacent molecules. For Φ_0 we obtain a value of 0.54 for type II exceeding the one of the neat film.

The results of figure 6.3 and 6.4 have clear implications for the design of OLEDs based on deep-blue emitters operating at high voltages. A major consequence is the choice of host materials with a type I alignment with respect to the emitter HOMO and LUMO, beside the established guideline of higher triplet energy levels [176]. More importantly, focusing on the behaviour of the pure emitter, we note that aggregated molecules can have an important role in the electric field quenching phenomena.
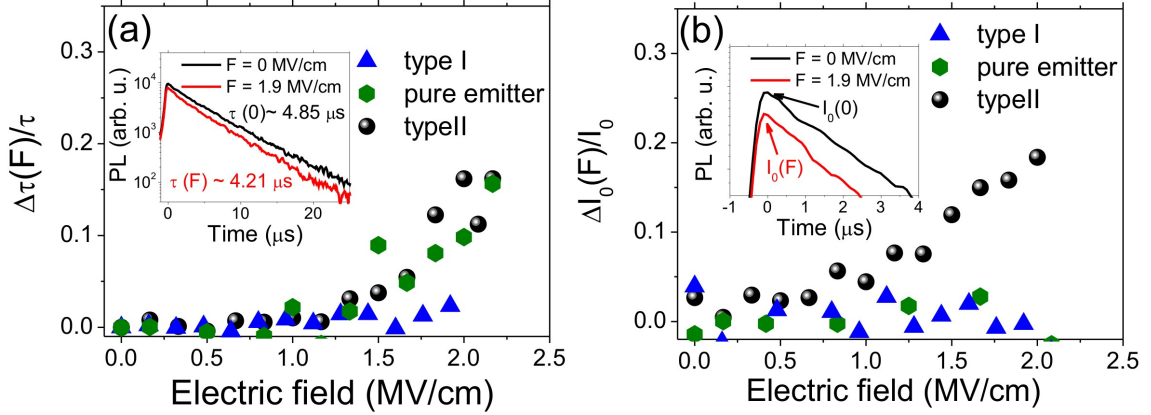
Figure 6.5: *(a) Relative change in the emitter PL lifetime $(\Delta\tau(F)/\tau)$ as a function of the applied electric field in type II (black dots), pure emitter (green hexagons) and type I (blue triangles). The inset shows two decay curves in the presence (red line) and absence (black line) of the external field for the type II sample. (b) Relative change in the intensity of PL at zero delay time $\Delta I_0(F)/I_0$ (amplitude quenching) for the same three samples of (a). The inset shows an example of quenching in the intensity at zero delay for the type II sample, the black line represents data at zero applied field while the red at $1.9\,MV/cm$.*

6.2   Dynamics of exciton dissociation

We now turn our attention on the mechanism of field induced quenching. In all the experiments reported in figure 6.3 excitons were created preferentially on the emitter molecules but also on the host material. As a consequence, the phosphorescence quenching could originate both from excitons dissociating in highly excited states before relaxation to the emitting level and from dissociation of thermalized emitter excitons. To clarify the mechanism involved in the emitter PL quenching, we have analyzed the time resolved decays of the PL, in the presence and absence of the field. The inset of figure 6.5 (a) shows the effect of the field on the decay curves for the type II sample $(Ir(cnpmbic)_3$ in $Ir(dpbic)_3)$. Upon application of the electric field both the PL lifetime τ and the signal amplitude at zero delay time I_0 are influenced. The change in amplitude can be better observed by focusing on the shorter time scale displayed in the inset of figure 6.5 (b). Amplitude quenching suggests the dissociation of a part of the excitons, during the thermalization process, while the shortening of the lifetime is witnessing exciton dissociation once thermalization to the emitting level is complete. We performed this kind of experiment also for the pure emitter and for the emitter in the type I configuration and plotted the relative variation of the lifetime $(\Delta\tau(F)/\tau)$ and amplitude $(\Delta I_0(F)/I_0)$ as a function of the applied field in figure 6.5 (a) and (b),

respectively. For the type I configuration the variation in lifetime and amplitude intensity is negligible. This is consistent with the steady state measurements of figure 6.3. In contrast, the type II structure shows large changes (black dots). We observe a decrease in the amplitude I_0 suggesting a separation of excitons precursors. In addition, the shortening of the emitter lifetime is a clear indication of exciton separation after thermalization. The data points for the pure emitter are shown as green hexagons. For low values of the electric field ($< 1\,\text{MV/cm}$), $\Delta I_0(F)/I_0$ shows a small change which saturates at about $2\,\%$ (figure 6.5 (b)). The $\Delta \tau(F)/\tau$ is increasing after $1.2\,\text{MV/cm}$ (figure 6.5 (a)).

6.3 Discussion

The results reported in figure 6.3 clarify the role of energy level alignment in controlling the electric field induced quenching of phosphorescent emitters. While this issue has been addressed in many experiments on different structures [45, 105, 120], our results demonstrate that the quenching is strongly dependent on the host/emitter energy level alignment and field amplitude. Both the type II and the pure emitter configurations lead to a strong quenching, which is likely due to exciton dissociation. This is supported by observing a lower PL quantum yield for the type II structure ($\Phi_{PL} = 50\,\%$) when compared to the type I ($\Phi_{PL} = 80\,\%$), in the absence of the external field at room temperature. This is probably due to a certain probability of exciton dissociation in the initial non-thermalized state, i.e. before relaxation to the emitting level and formation of Coulomb stabilized excitons. Therefore, our results should be interpreted according to the differences in host/emitter energy level alignment in the presence of the field at different stages of exciton relaxation.

Field induced quenching of luminescence has been extensively studied in thin films of pristine and dispersed conjugated polymers [122, 177]. In such fluorescent materials the lifetime of singlet excitons is typically in the sub-nanosecond time range much faster with respect to the phosphorescence processes investigated here. To explain the quenching phenomena with magnitudes up to $30\,\%$ for those fluorescent materials, a fast dissociation ($\approx 10\,\text{ps}$) was invoked. In contrast to polymers, triplet emitters show microsecond recombination times for the spin-forbidden phosphorescent transitions. Assuming a similar time scale for field induced quenching, it should be possible to dissociate very efficiently the long lived excitons populating the triplet state. Our data
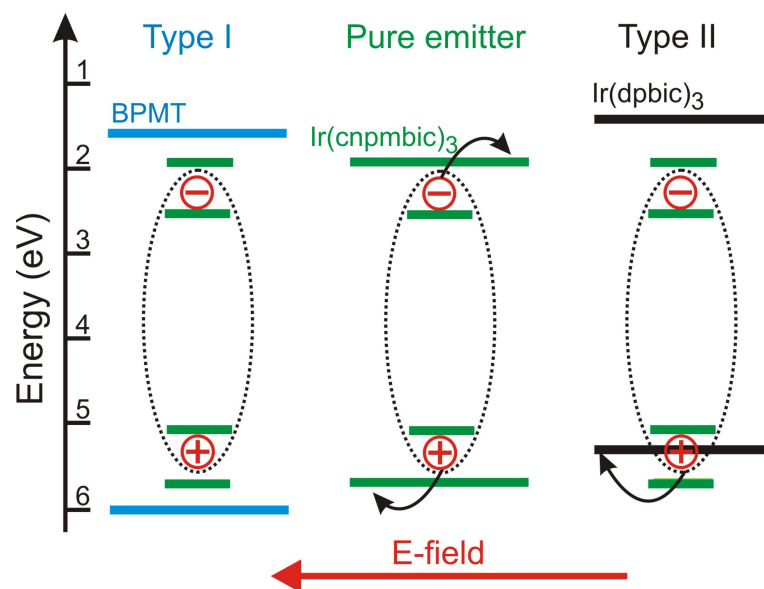
Figure 6.6: *Schematic representation of the energy levels for the different host/emitter combinations. The HOMO and LUMO levels of the hosts and emitter are shown together with the excitonic levels. These levels are inside the black dotted circle indicating their excitonic nature. Their closed spacing with respect to the HOMO and LUMO of the emitter is due to the binding energy. The curved arrows show possible exciton separation processes upon application of the external electric field. This results in the transfer of an electron or a hole to the surrounding molecules that constitute the host material. In the type I system the absence of accepting levels prevents exciton dissociation. In the pure emitter both the HOMO and LUMO of the surrounding emitter molecules provide a density of states for charge separation. The type II structure promotes exciton dissociation by hole transfer.*

on the pure and type II sample show, however, comparable or lower quenching magnitudes with respect to conjugated polymers. To understand this issue and interpret the origin of the significant differences reported in our experiments, we have considered the energy level configurations of the different samples and interpreted the results.

6.3.1   Microscopic interpretation

Figure 6.6 shows a simplified scheme in a one-particle picture, for the energy of an electron and a hole building an exciton on the emitter molecule in the three most relevant samples. To consider non-thermalized states we have drawn two levels for the hole and the electron, respectively. The closest ones are stabilized by the Coulomb interaction (here schematically shown as a black dotted line) and correspond to the emitting triplet exciton. The exciton binding energy was estimated subtracting the emission energy from the HOMO and LUMO gap of figure 6.1. We start by considering the type I configuration, where the HOMO and LUMO of the emitter (green levels)

are within the ones of BPMT (blue levels). The effect of the external electric field is to modify the Coulomb potential profile destabilizing the excitonic levels [22]. In this situation the exciton can dissociate, provided that a density of states for charge transfer is available in the surrounding of the emitter molecule. This last condition is not satisfied for the type I alignment. Therefore, the absence of available states for electron or hole escape, both in the non-thermalized and in the excitonic level, results in a negligible quenching for the field strengths investigated in our experiments.

We turn now to the case of the film formed exclusively by emitter molecules (pure emitter). From the energy scheme we identify two possibilities for charge separation in the pristine emitter film, i.e. hole as well as electron transfer to the surrounding acceptor molecules. In a similar way to conjugated polymers the charge separation may be promoted by energetic disorder in the system [174]. We have indeed observed a red shifted component in the PL spectrum of this film, witnessing the presence of low energy sites. Such low energy states might facilitate charge separation in the presence of the field. The limited zero-time amplitude quenching reported in figure 6.5 is correlated to a more pronounced exciton separation in the emitting state.

A specific scheme describes the type II material combination. The host HOMO (black solid line) is at higher energy with respect to the one of the emitter, while the excitonic levels keep the exciton bound. Therefore, the external field by destabilizing the exciton promotes the separation with hole transfer to the host (curved arrow). As indicated in the figure and confirmed by the time resolved experiments (figure 6.5), the transfer can occur both in the emitting and in the precursor states. From an energetic point of view, the type II structure increases the density of available states for the hole to escape from the emitter. The larger contribution of amplitude quenching at low fields is confirmed in our picture since non-thermalized states require only a small field for the separation to occur. We stress that the quenching in the type II combination, where electrons remain trapped on the emitter molecule and only holes have available states for the separation may differ from the pure emitter. In the latter case exciton dissociation should generate both electrons and holes, which are free to drift by hopping among the different molecular sites. Summarizing the mechanism reported in figure 6.6, we note that electric field induced quenching strongly depends on the density of available states for charge separation. Because of the peculiar energy alignment this makes exciton dissociation very probable for type II and pure emitter structures.

6.3.2   Products of exciton dissociation

To further investigate the products resulting from exciton separation, we performed quenching measurements in the presence of a pulsed electric field. Such a technique
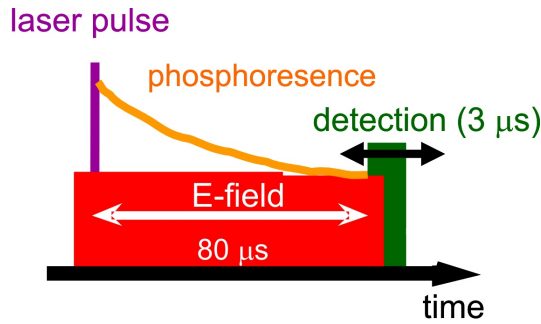
Figure 6.7: *Timing scheme for the experiments to investigate the products resulting from exciton separation. The laser pulse is indicated as a violet line, the red box indicates the electric field pulse duration and the green box the detection window. The temporal width of the boxes sketched in the inset is not in scale.*

proved to be sensitive to the formation of PPs or free polarons, according to the recovery of PL intensity after the field pulse. In the case of field stabilized PPs, excitons should be regenerated after the release of the field and part of the quenched PL intensity is recovered in a PL burst [174, 11]. Figure 6.7 shows a timing scheme for such kind of transient experiment. In brief, the field is applied during the photoexcitation event and turned off after $80\,\mu$s. A scanning gated detection of $3\,\mu$s (green box) is shifted in time to record point by point the PL intensity from the emitter. In the figure 6.8
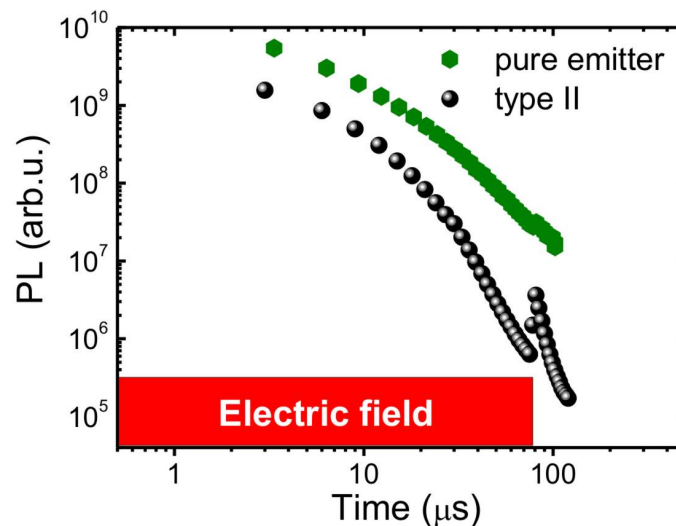
Figure 6.8: *PL decay in the presence of an electric field pulse for the pure emitter (green hexagons) and the type II structure (black dots). The field pulse is applied for $80\,\mu$s starting in correspondence of the laser pulse. The detection window ($3\,\mu$s) is moved at different delays with respect to the laser pulse during the field pulse and after its turning off.*

we present typical data for the type II combination Ir(cnpmbic)$_3$ in Ir(dpbic)$_3$ (black dots). Corresponding to the instant in which the electric field pulse ends (80 μs) a burst in the PL intensity is observed. This result implies the creation of PPs partially stabilized by a Coulomb potential. The pairs appear as a burst of emission due to the regeneration of triplet excitons, once the electric field is turned off. For the type II structure shown here, it is conceivable that holes are trapped in the Ir(dpbic)$_3$ HOMO levels, while the electrons remain localized on the emitter molecule (see energy scheme in figure 6.6). In contrast to this behaviour, the pure emitter sample shows an almost undetectable PL burst. From these results we infer that PP states are much less stable in this sample. Interestingly, this correlates with the larger values of the PP radius we reported above, extracted from the Onsager fit. Apparently the presence of localization sites for at least one type of charge carrier is a necessary condition to observe PPs.

6.3.3 Escape rate of dissociation

We discuss now the discrepancy between the fast exciton dissociation (ps-timescale) observed in conjugated polymers and the comparable quenching, though with three orders of magnitude longer exciton lifetimes, observed here in a triplet emitter. As mentioned above, the first step of exciton dissociation is limited by the exciton binding energy which is about 0.4 eV for most studied conjugated polymers [24, 25]. For small molecules the exciton binding energy is larger than this value (section 2.1.2). For Ir(cnpmbic)$_3$ the HOMO LUMO difference predicts an electronic bandgap of 3.8 eV (figure 6.1 (b)). By considering the optical gap of the emitting state (2.90 eV from figure 6.1 (a)) we can estimate an exciton binding energy of about 0.9 eV. This relatively large value should influence the rate of escape of charge carriers from the mutual Coulomb potential in the excitonic level (figure 6.6)). Figure 6.9 shows the escape rate k$_e$(F) as a function of the electric field for the pure emitter and the type II. The rate has been evaluated considering that the exciton recombination rate is described by the following equation:

$$k(F) = k_r + k_{nr} + k_e(F), \tag{6.1}$$

where k$_r$ and k$_{nr}$ are the radiative and non radiative rate, respectively. In this equation all the values apart from the escape rate are known, with the reasonable assumption that k$_r$ and k$_{nr}$ are not influenced by the field amplitudes considered in our experiments. Such an assumption is supported by the negligible quenching of the emitter
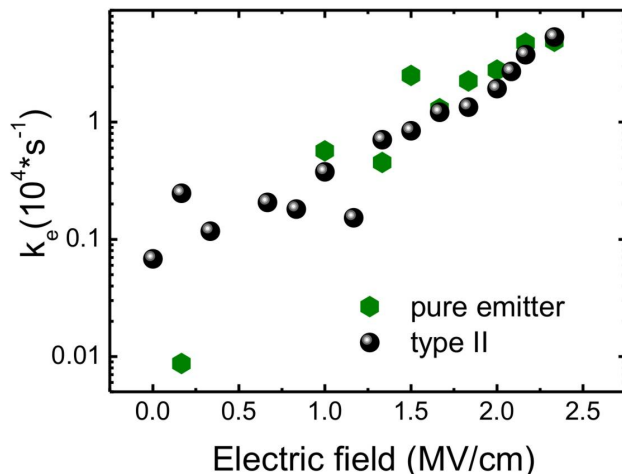
Figure 6.9: *Escape rate k_e as a function of the external electric field. Data points were obtained from equation 6.1). Green hexagons indicate data for the pure emitter and black dots for the type II structure.*

in PMMA (figure 6.3). The escape rates reported in figure 6.9 are of the same order of magnitude with respect to the recombination rate (for the investigated emitter molecules $\approx 10^5 \, \mathrm{s}^{-1}$). It is not surprising that the quenching is similar or lower to the one observed in polymers, though the recombination rate is at least four orders of magnitude longer (phosphorescence). The long escape rate of our blue emitter can be interpreted taking into account the high binding energy. Since an exponential dependence of the escape rate on the binding energy has to be expected, a factor of two in the binding energy, readily results in a difference of seven orders of magnitude in the escape rate between polymers and small molecules [54].

6.4   Implications for quenching in OLEDs

In this chapter we have the studied electric field induced quenching on the phosphorescence intensity of different host/guest systems. According to our results, the electric field induced quenching can be very sensitive to the emitter concentration and host/emitter combination, an issue which was not systematically discussed in previous reports [45, 105, 120, 178]. We stress that the modeling of the quenching phenomena contributing to the efficiency roll-off of electroluminescence in devices, should also consider exciton-exciton (TTA) and exciton-polaron annihilation (TPA) phenomena as discussed in chapter 2.4.2.

TTA was studied by analyzing the PL transients. For this kind of investigations, we excite thin organic films, containing different host/emitter systems, by a short laser pulse. By increasing the excitation density, an initial faster decay appears in the time decay of the emitter PL, which is attributed to TTA (figure 6.10 (a)). The overall decay can be fitted according to equation 2.30. Assuming the initial exciton concentration $[T_1(0)]$ and the experimentally determined the lifetime τ_T, the TTA rate constant (k_{TTA}) can be derived (section 2.4.2). In figure 6.10 (b) k_{TTA} is plotted against
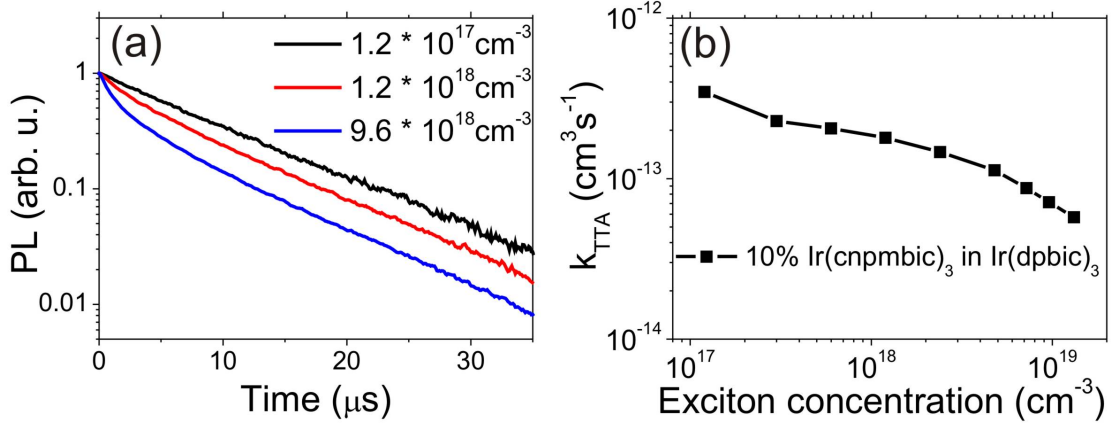
Figure 6.10: (a) PL decay of 10 % Ir(cnpmbic)₃ in Ir(dpbic)₃ at different inital exciton concentrations $[T_1]$. (b) The TTA rate, k_{TTA}, is plotted against exciton concentrations for PL transient measurements.

the exciton concentration $[T_1(0)]$ for PL transient measurements. The investigated film consists of 10 % Ir(cnpmbic)₃ doped in the host material Ir(dpbic)₃. The mean value of k_{TTA} is $1.6 \cdot 10^{-13}$ cm³s⁻¹. In other reports k_{TTA} is in the same range of magnitude or slightly higher [61, 105, 179]. The obtained parameter is used to fit the roll-off of the external quantum efficiency of an OLED, which employ this host/guest system as emission layer. According to Baldo et al., the external quantum efficiency η_{ext} of an OLED can be expressed by

$$\frac{\eta_{ext}}{\eta_0} = \frac{J_0}{4J}\left(\sqrt{1 + 8\frac{J}{J_0}} - 1\right),$$
(6.2)

where η_0 is the external quantum efficiency in the absence of TTA, and

$$J_0 = \frac{4ed}{k_{TTA}\tau_T^2}$$
(6.3)

the onset current density at $\eta_{ext} = \eta_0/2$ [61].
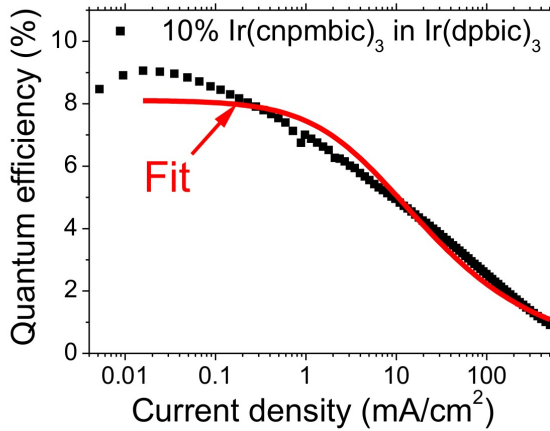
Figure 6.11: *External quantum efficiency as a function of the current density for a device setup with 10 % Ir(cnpmbic)$_3$ in Ir(dpbic)$_3$ as EML. The red solid line represents the model calculation according to equation 6.2.*

Figure 6.11 shows the roll-off of the multilayer OLED introduced in section 2.4. Equation 6.2 is used to fit the external quantum efficiency. One obtains from the data points a value for J_0 of about 20.7 mA/cm^2, which is slightly below the value calculated from equation 6.3 with the values obtained from the PL time decay measurements ($J_0^{PL} = 32$ mA/cm^2). This means that considering TTA only the current necessary to have half of the external quantum efficiency is higher than what experimentally observed in a device. A deviation of the fit from the experimental data is apparent. Therefore we conclude, that not only TTA, but also TPA and according to our reported results, electric field induced quenching has to be taken into account. While triplet-polaron quenching has been recognized as less critical in explaining the roll-off of the electroluminescence efficiency with respect to TTA, it can be more pronounced especially for devices employing a type II emitting layer. Preliminary results regarding this subject have shown, that quenching of emitter excitons in type II structures is more pronounced for those charges which are transported by the emitter molecule itself. However, further investigations are necessary to reveal the influence of host/emitter alignment in TPA processes.

6.5 Summary

In conclusion, we have investigated the electric field induced quenching in the PL intensity of the deep-blue emitter Ir(cnpmbic)$_3$ in combination with several host materials building type I and type II molecular heterostructures. We report a strong field dependent quenching of the phosphorescence for thin films of the pure emitter and the type

II heterostructure. Besides to the well-known guideline of a higher triplet level, these results highlight the importance of energy level alignment of the chosen host/guest system. By time resolving the PL in the presence of the field we provide useful insights in the quenching mechanism. In particular, we demonstrated that dissociation occurs preferentially for Coulomb stabilized excitons, when the external field overcomes the binding energy and accepting states are available for charge transfer. Additionally, we report a long lasting formation of PPs, if one of the two charge carriers forming the exciton remains trapped on the emitter. The phosphorescence quenching has immediate consequences for the optimization of deep-blue-emitting OLEDs. While several aspects contribute to the efficiency of electroluminescence, such as charge injection, carrier balance, triplet-polaron quenching [105, 135], and exciton annihilation [61, 105], electric field induced quenching becomes critical when large local fields are building up at interfaces [122] and for particular HOMO-LUMO alignment between emitter and host, as demonstrated in this study. For deep-blue emitters the design of interfaces becomes critical as a consequence of high bandgap materials. While triplet-polaron quenching and TTA has been recognized as main quenching mechanism in red and green OLEDs, this might not hold true for deep-blue emitters where charge accumulation at organic heterojunctions or high driving voltages could result in high fields.

We conclude that type I structures can reduce substantially the quenching for fields up to $2\,\mathrm{MV/cm}$. On the contrary an effect can be observed at relatively low driving voltages ($6.25\,\mathrm{V} = 0.5\,\mathrm{MV/cm}$) in the case of type II configurations. These experiments should provide valuable insights for the design of blue electrophosphorescent OLEDs and more generally other organic electroluminescent devices, where large driving electric fields are involved and high electroluminescence efficiencies are critical [180, 181].

Chapter 7

Conclusions and outlook

The aim of this work was to understand the photophysics in novel organic semiconductors used for deep-blue emitting organic light-emitting diodes (OLEDs). In particular, the investigation of the electronic structure, the resulting physical properties and loss channels in host/guest systems were in the main focus. By steady-state, time-resolved and single molecule spectroscopy we were able to address these subjects and provide useful information for the advancement of this technology.

First, we analyzed the physical parameters which control the radiative rate in a series of phosphorescent organometallic complexes emitting in the deep-blue. Higher radiative rates decrease the residence time of potentially unstable excited states improving the efficiency and long term stability. For these investigations we produced thin films of deep-blue phosphorescent molecules, which were doped in an isolating host material. Despite the very high intersystem crossing rates from the excited singlet to the triplet state, we demonstrated the possibility to observe fluorescent emission of organometallic complexes by low temperature time-gated spectroscopy. This was used to experimentally determine the singlet-triplet splitting ΔE_{ST}. For highly efficient iridium complexes we showed how ΔE_{ST} can be tuned according to the ligand structure. Therefore, we could extract values of ΔE_{ST} and reveal the importance of this parameter for controlling the phosphorescence radiative rate. We compared the experimentally determined ΔE_{ST} values with predictions from time-dependent density functional theory calculations and found a remarkable agreement. Our findings are of particular interest for the design of phosphorescent complexes. Processes detrimental to the efficiency, such as exciton-polaron quenching or triplet-triplet annihilation, could be strongly reduced with a faster exciton recombination. Additionally, we note that

exciton formation in a working OLED proceeds by opposite charge injection in the HOMO and LUMO of the emitting molecule, followed by thermalization to the emitting triplet state. As a consequence, low values of ΔE_{ST} will be beneficial in optimizing the power conversion efficiency and minimizing wasted heat in working devices.

To further reveal the complex electronic structure of organometallic complexes, we employed single molecule spectroscopy at cryogenic temperatures. Although single molecule spectroscopy has been an established technique for many years, there are only few spectroscopic reports on the emission properties of single phosphorescent molecules. In this work we could demonstrate for the first time that it is possible to detect the phosphorescence spectrum of individual organometallic compounds at low temperatures and that single molecule spectroscopy gives unique insights into the fine electronic structure that is usually hidden in ensemble spectroscopy. While most of this thesis deals with blue emitters we chose for this study a red one, since background scattering from the substrate and the matrix in which emitters are dispersed is less severe in the red part of the visible spectrum. The molecules were dispersed in toluene and then in a highly transparent matrix at a concentration in the range of 10^{-6} - 10^{-8} mg/ml. We first demonstrated the detection of individual emitters, which is experimentally challenging due to the low average number of photons emitted per second. Experimental proof of single molecule detection is obtained by observing very narrow linewidths of only 0.3 meV. Such narrow lines have usually been reported in single molecule experiments, where the spectral inhomogeneous broadening can be overcome. Additionally, we reported on the observation of a blinking behavior of phosphorescence intensity and of linearly polarized emission, both confirming the detection of spectral features of single organometallic complexes. Furthermore, we observed the occurrence of two peaks representing the zero-field splitting of two bright emitting triplet substates. Remarkably, the zero-field splitting shows spectral diffusion. The spectral diffusion of this intrinsic molecular property is ascribed to modifications in the molecular geometry or fluctuations in the local environment of the emitter. We also detected fluctuations in the energetic distribution of the zero-field splitting, which are expected to be caused by variations of the effectiveness of spin-orbit coupling to the emitting triplet state. Our findings are of general importance for the understanding of the nature of the excited triplet state and pave the way to the application of single molecule spectroscopy in studying phosphorescent molecules for OLEDs.

In addition, we studied loss processes of host/emitter systems, which are used as

emission layers in OLEDs. In particular, the effect of an electric field on the phosphorescence intensity of a deep-blue triplet emitter dispersed in different host materials was investigated in detail. As the emitter material we employed the deep-blue emitter Ir(cnpmbic)$_3$, which shows efficient phosphorescence emission at room temperature. While the hosts are characterized by a higher triplet excitonic level with respect to the emitter, ensuring efficient energy transfer and exciton confinement, they differ in the highest occupied molecular orbital alignment, forming type I and type II host/guest heterostructures. We reported a strong field dependent quenching of the phosphorescence for thin films of the pure emitter and of the type II heterostructure. These results highlight the importance of energy level alignment in the choice of suitable matrix materials for hosting deep-blue phosphors, in addition to the well-known guideline of a higher triplet level. By time resolving the photoluminescence in the presence of the field we provided useful insights into this quenching mechanism. In particular, we demonstrated that dissociation occurs preferentially for Coulomb stabilized excitons, when the external field overcomes the binding energy and accepting states are available for charge transfer. In addition, we reported a long lasting formation of polaron pairs, if one of the two charge carriers forming the exciton remains trapped on the emitter.

The phosphorescence quenching has immediate consequences for the optimization of deep-blue emitting OLEDs. While several aspects contribute to the efficiency of electroluminescence, such as charge injection, carrier balance, triplet-polaron quenching and exciton annihilation, electric field induced quenching becomes critical when large local fields are present at interfaces and for particular orbital alignments between emitter and host. For deep-blue emitters the design of interfaces becomes critical as a consequence of high bandgap materials. While triplet-polaron quenching has been recognized as less critical in explaining the roll-off of the electroluminescence efficiency than triplet-triplet annihilation, this might not hold true for deep-blue emitters. Here, charge accumulation at organic heterojunctions or high driving voltages could result in high fields. We conclude that type I structures can substantially reduce the quenching for fields up to $2\,\mathrm{MV/cm}$. On the contrary an effect can be observed at relatively low driving voltages in the case of type II configurations. These experiments should provide valuable insights for the design of blue electrophosphorescent OLEDs.

Organometallic complexes with carbene ligands are promising dopants in all triplet-emitting OLEDs for creating efficient white light in combination with green and red phosphorescent emitters. White light-emitting OLEDs are considered as the next gen-

eration of light sources. During this work the stability of OLEDs has indeed increased dramatically by employing emitters with very high radiative rates, approaching the sub-microsecond time regime. Before such devices can enter the consumer market for white light generation their stability has to be improved further and their low output coupling efficiency and relatively high manufacturing costs have to be addressed. However, due to their outstanding properties, OLEDs have the potential to outshine their solid state lighting competition in the future.

Abbreviations

CCD:	Charge-coupled device
CIE:	Commission internationale de l´eclairage
DFT:	Density functional theory
DOS:	Density of states
EML:	Emitting layer
FWHM:	Full width at half maximum
HBL:	Hole blocking layer
HOMO:	Highest occupied molecular orbital
HTL:	Hole transporting layer
ETL:	Electron transporting layer
IEPS:	Inverse electron photoemission spectroscopy
ISC:	Intersystem crossing
ITO:	Indium tin oxide
LC:	Ligand-centered
LCAO:	Linear combination of atomic orbitals
LUMO:	Lowest unoccupied molecular orbital
MCP:	Micro channel plate
MLCT:	Metal to ligand charge transfer
NA:	Numeric aperture
Nd:YAG:	Neodymium-doped yttrium aluminum garnet
OLED:	Organic light emitting diode
OPA:	Optical parametric amplifier
PL:	Photoluminescence
PP:	Polaron-pair
SLR:	Spin-lattice relaxation
SMS:	Single molecule spectroscopy
SOC:	Spin-orbit coupling
SSI:	Spin-spin-interaction
TD-DFT:	Time-dependent density functional theory
Ti:Sa:	Titanium-sapphire
TPA:	Triplet-polaron annihilation
TTA:	Triplet-triplet annihilation
UPS:	Ultraviolet photoelectron spectroscopy
UV:	Ultraviolet
ZFS:	Zero-field splitting
ZPL:	Zero phonon line

Bibliography

[1] C. K. Chiang, C. R. Fincher, Y. W. Park, A. J. Heeger, H. Shirakawa, E. J. Louis, S. C. Gau, and A. G. Macdiarmid. *Electrical-conductivity in doped polyacetylene*. Physical Review Letters, **39** (17), 1098 (1977).

[2] A. J. Heeger. *Nobel lecture: Semiconducting and metallic polymers: The fourth generation of polymeric materials*. Reviews of Modern Physics, **73** (3), 681 (2001).

[3] M. Pope, P. Magnante, and H. P. Kallmann. *Electroluminescence in organic crystals*. Journal of Chemical Physics, **38** (8), 2042 (1963).

[4] W. Helfrich and W. Schneide. *Recombination radiation in anthracene crystals*. Physical Review Letters, **14** (7), 229 (1965).

[5] M. Pope and C. E. Swenberg. *Electronic Processes in Organic Crystals and Polymers (2nd Edition)*. Oxford University Press, New York (1999).

[6] C. W. Tang and S. A. Vanslyke. *Organic electroluminescent diodes*. Applied Physics Letters, **51** (12), 913 (1987).

[7] J. H. Burroughes, D. D. C. Bradley, A. R. Brown, R. N. Marks, K. Mackay, R. H. Friend, P. L. Burns, and A. B. Holmes. *Light-emitting-diodes based on conjugated polymers*. Nature, **347** (6293), 539 (1990).

[8] R. H. Friend, R. W. Gymer, A. B. Holmes, J. H. Burroughes, R. N. Marks, C. Taliani, D. D. C. Bradley, D. A. Dos Santos, J. L. Bredas, M. Logdlund, and W. R. Salaneck. *Electroluminescence in conjugated polymers*. Nature, **397** (6715), 121 (1999).

[9] P. Semenza. *Can anything catch TFT LCDs?*. Nature Photonics, **1** (5), 267 (2007).

[10] M. A. Baldo, D. F. O'Brien, Y. You, A. Shoustikov, S. Sibley, M. E. Thompson, and S. R. Forrest. *Highly efficient phosphorescent emission from organic electroluminescent devices*. Nature, **395** (6698), 151 (1998).

[11] M. Reufer, M. J. Walter, P. G. Lagoudakis, B. Hummel, J. S. Kolb, H. G. Roskos, U. Scherf, and J. M. Lupton. *Spin-conserving carrier recombination in conjugated polymers*. Nature Materials, **4** (4), 340 (2005).

[12] C. Adachi, M. A. Baldo, M. E. Thompson, and S. R. Forrest. *Nearly 100% internal phosphorescence efficiency in an organic light-emitting device*. Journal of Applied Physics, **90** (10), 5048 (2001).

[13] C. Adachi, M. A. Baldo, S. R. Forrest, and M. E. Thompson. *High-efficiency organic electrophosphorescent devices with tris(2-phenylpyridine)iridium doped into electron-transporting materials*. Applied Physics Letters, **77** (6), 904 (2000).

[14] C. Adachi, M. A. Baldo, S. R. Forrest, S. Lamansky, M. E. Thompson, and R. C. Kwong. *High-efficiency red electrophosphorescence devices*. Applied Physics Letters, **78** (11), 1622 (2001).

[15] A. Bergh, G. Craford, A. Duggal, and R. Haitz. *The promise and challenge of solid-state lighting*. Physics Today, **54** (12), 42 (2001).

[16] I. Akasaki and H. Amano. *Crystal growth and conductivity control of group III nitride semiconductors and their application to short wavelength light emitters*. Japanese Journal of Applied Physics Part 1-Regular Papers Short Notes and Review Papers, **36** (9A), 5393 (1997).

[17] F. Schindler, J. M. Lupton, J. Feldmann, and U. Scherf. *A universal picture of chromophores in π-conjugated polymers derived from single-molecule spectroscopy*. Proceedings of the National Academy of Sciences of the United States of America, **101** (41), 14695 (2004).

[18] D. H. Hu, J. Yu, and P. F. Barbara. *Single-molecule spectroscopy of the conjugated polymer MEH-PPV*. Journal of the American Chemical Society, **121** (29), 6936 (1999).

[19] H. Haken and H. C. Wolf. *Molekühlphysik und Quantenchemie: Einführung in die experimentellen und theoretischen Grundlagen*. Springer-Verlag, Berlin-Heidelberg (1992).

[20] R. Peierls. *Quantum Theory of Solids*. Oxford University Press, Oxford (1955).

[21] W. P. Su, J. R. Schrieffer, and A. J. Heeger. *Solitons in polyacetylene*. Physical Review Letters, **42** (25), 1698 (1979).

[22] M. Schwoerer and H. C. Wolf. *Organische molekulare Festkörper*. Wiley-VCH Verlag GmbH and Co., Weinheim (2005).

[23] S. Haneder, E. Da Como, J. Feldmann, M. M. Rothmann, P. Strohriegl, C. Lennartz, O. Molt, I. Munster, C. Schildknecht, and G. Wagenblast. *Effect of electric field on coulomb-stabilized excitons in host/guest systems for deep-blue electrophosphorescence*. Advanced Functional Materials, **19** (15), 2416 (2009).

[24] S. F. Alvarado, P. F. Seidler, D. G. Lidzey, and D. D. C. Bradley. *Direct determination of the exciton binding energy of conjugated polymers using a scanning tunneling microscope*. Physical Review Letters, **81** (5), 1082 (1998).

[25] S. Barth and H. Bässler. *Intrinsic photoconduction in PPV-type conjugated polymers*. Physical Review Letters, **79** (22), 4445 (1997).

[26] M. Thompson. *The evolution of organometallic complexes in organic light - emitting devices*. Mrs Bulletin, **32** (9), 694 (2007).

[27] W. Kohn. *Nobel lecture: Electronic structure of matter-wave functions and density functionals*. Reviews of Modern Physics, **71** (5), 1253 (1999).

[28] A. J. Heeger, S. Kivelson, J. R. Schrieffer, and W. P. Su. *Solitons in conducting polymers*. Reviews of Modern Physics, **60** (3), 781 (1988).

[29] P. Hohenberg and W. Kohn. *Inhomogeneous electron gas*. Physical Review B, **136** (3B), B864 (1964).

[30] M. A. L. Marques and E. K. U. Gross. *Time-dependent density functional theory*. Annual Review of Physical Chemistry, **55**, 427 (2004).

[31] W. Kohn and L. J. Sham. *Self-consistent equations including exchange and correlation effects*. Physical Review, **140** (4A), 1133 (1965).

[32] E. Runge and E. K. U. Gross. *Density-functional theory for time-dependent systems*. Physical Review Letters, **52** (12), 997 (1984).

[33] P. J. Hay. *Theoretical studies of the ground and excited electronic states in cyclometalated phenylpyridine Ir(III) complexes using density functional theory*. Journal of Physical Chemistry A, **106** (8), 1634 (2002).

[34] S. Haneder, E. Da Como, J. Feldmann, J. M. Lupton, C. Lennartz, P. Erk, E. Fuchs, O. Molt, I. Munster, C. Schildknecht, and G. Wagenblast. *Controlling the radiative rate of deep-blue electrophosphorescent organometallic complexes by singlet-triplet gap engineering*. Advanced Materials, **20** (17), 3325 (2008).

[35] N. G. Park, G. C. Choi, J. E. Lee, and Y. S. Kim. *Theoretical studies of cyclometalated phenylpyrazol Ir(III) complex using density functional theory*. Current Applied Physics, **5** (1), 79 (2005).

[36] J. Gierschner, H. G. Mack, L. Luer, and D. Oelkrug. *Fluorescence and absorption spectra of oligophenylenevinylenes: Vibronic coupling, band shapes, and solvatochromism*. Journal of Chemical Physics, **116** (19), 8596 (2002).

[37] J. R. Lakowicz. *Principles of Fluorescence Spectroscopy (Second Edition)*. Kluwer, New York (1999).

[38] N. Turro. *Modern Molecular Photochemistry*. University Science Books, Sausalito, California (1991).

[39] Y. V. Romanovskii, A. Gerhard, B. Schweitzer, U. Scherf, R. I. Personov, and H. Bässler. *Phosphorescence of π-conjugated oligomers and polymers*. Physical Review Letters, **84** (5), 1027 (2000).

[40] A. Kohler and D. Beljonne. *The singlet-triplet exchange energy in conjugated polymers*. Advanced Functional Materials, **14** (1), 11 (2004).

[41] J. M. Lupton, A. Pogantsch, T. Piok, E. J. W. List, S. Patil, and U. Scherf. *Intrinsic room-temperature electrophosphorescence from a π-conjugated polymer*. Physical Review Letters, **89** (16), (2002).

[42] C. Rothe, S. M. King, and A. P. Monkman. *Electric-field-induced singlet and triplet exciton quenching in films of the conjugated polymer polyspirobifluorene*. Physical Review B, **72** (8), 085220 (2005).

[43] H. Bässler, V. I. Arkhipov, E. V. Emelianova, A. Gerhard, A. Hayer, C. Im, and J. Rissler. *Excitons in π-conjugated polymers*. Synthetic Metals, **135** (1-3), 377 (2003).

[44] C. Kittel. *Einführung in die Festkörperphysik*. R.Oldenbourg Verlag, München, Wien (1989).

[45] J. Kalinowski, W. Stampor, J. Szmytkowski, D. Virgili, M. Cocchi, V. Fattori, and C. Sabatini. *Coexistence of dissociation and annihilation of excitons on charge carriers in organic phosphorescent emitters*. Physical Review B, **74** (8), (2006).

[46] M. Pope and J. Burgos. *Charge-transfer exciton state and ionic energy levels in anthracene crystal*. Molecular Crystals, **1** (3), 395 (1966).

[47] M. Hallermann, S. Haneder, and E. Da Como. *Charge-transfer states in conjugated polymer/fullerene blends: Below-gap weakly bound excitons for polymer photovoltaics*. Applied Physics Letters, **93** (5), 3 (2008).

[48] S. Barth, D. Hertel, Y. H. Tak, H. Bässler, and H. H. Horhold. *Geminate pair dissociation in random organic systems*. Chemical Physics Letters, **274** (1-3), 165 (1997).

[49] D. Hertel, E. V. Soh, H. Bässler, and L. J. Rothberg. *Electric field dependent generation of geminate electron-hole pairs in a ladder-type π-conjugated polymer probed by fluorescence quenching and delayed field collection of charge carriers*. Chemical Physics Letters, **361** (1-2), 99 (2002).

[50] V. Gulbinas, Y. Zaushitsyn, V. Sundstrom, D. Hertel, H. Bässler, and A. Yartsev. *Dynamics of the electric field-assisted charge carrier photogeneration in ladder-type poly(para-phenylene) at a low excitation intensity*. Physical Review Letters, **89** (10), 107401 (2002).

[51] L. Onsager. *Initial recombination of ions*. Physical Review, **54** (8), 554 (1938).

[52] J. Noolandi and K. M. Hong. *Theory of photogeneration and fluorescence quenching*. Journal of Chemical Physics, **70** (7), 3230 (1979).

[53] E. A. Silinsh and H. Inokuchi. *On charge carrier photogeneration mechanisms in organic molecular-crystals*. Chemical Physics, **149** (3), 373 (1991).

[54] C. L. Braun. *Electric-field assisted dissociation of charge-transfer states as a mechanism of photocarrier production*. Journal of Chemical Physics, **80** (9), 4157 (1984).

[55] P. M. Borsenberger and A. I. Ateya. *Hole photogeneration in poly(n-vinylcarbazole)*. Journal of Applied Physics, **49** (7), 4035 (1978).

[56] J. Jung, I. Glowacki, and J. Ulanski. *Analysis of electric-field assisted photogeneration in polyparacyclophane doped with 2,4,7-trinitrofluorenone*. Journal of Chemical Physics, **110** (14), 7000 (1999).

[57] E. Riedel. *Allgemeine und Anorganische Chemie*. Walter de Gruyter, Berlin, New York (2008).

[58] M. G. Colombo, A. Hauser, and H. U. Gudel. *Evidence for strong mixing between the LC and MLCT excited-states in bis(2-phenylpyridinato-C2,N') (2,2'-bipyridine) iridium(III)*. Inorganic Chemistry, **32** (14), 3088 (1993).

[59] S. Lamansky, P. Djurovich, D. Murphy, F. Abdel-Razzaq, H. E. Lee, C. Adachi, P. E. Burrows, S. R. Forrest, and M. E. Thompson. *Highly phosphorescent bis-cyclometalated iridium complexes: Synthesis, photophysical characterization, and use in organic light emitting diodes*. Journal of the American Chemical Society, **123** (18), 4304 (2001).

[60] N. H. Damrauer, G. Cerullo, A. Yeh, T. R. Boussie, C. V. Shank, and J. K. McCusker. *Femtosecond dynamics of excited-state evolution in [Ru(bpy)(3)]$^{2+}$*. Science, **275** (5296), 54 (1997).

[61] M. A. Baldo, C. Adachi, and S. R. Forrest. *Transient analysis of organic electrophosphorescence: II. transient analysis of triplet-triplet annihilation*. Physical Review B, **62** (16), 10967 (2000).

[62] F. W. M. Vanhelmont, H. U. Gudel, M. Fortsch, and H. B. Burgi. *Synthesis, crystal structure, high-resolution optical spectroscopy, and extended Huckel calculations for [Re(CO)$_4$(thpy)] (thpy$^-$ = 2-(2-thienyl)pyridinate). Comparison with related cyclometalated complexes*. Inorganic Chemistry, **36** (24), 5512 (1997).

[63] W. J. Finkenzeller, P. Stossel, and H. Yersin. *Emission and absorption of Ir(ppy)$_2$(CO)(Cl) - temperature dependence, phosphorescence decay dynamics, and assignment of excited states*. Chemical Physics Letters, **397** (4-6), 289 (2004).

[64] H. Yersin. *Highly efficient OLEDs with phosphorescent materials*. Wiley-VCH. Weinheim, Germany (2008).

[65] X. Y. Wang, A. Del Guerzo, and R. H. Schmehl. *Photophysical behavior of transition metal complexes having interacting ligand localized and metal-to-ligand charge transfer states*. Journal of Photochemistry and Photobiology C-Photochemistry Reviews, **5** (1), 55 (2004).

[66] C. Cohen-Tannoudji, B. Diu, and F. Laloe. *Quantum Mechanics*. John Wiley, Paris (1977).

[67] J. Li, P. I. Djurovich, B. D. Alleyne, I. Tsyba, N. N. Ho, R. Bau, and M. E. Thompson. *Synthesis and characterization of cyclometalated Ir(III) complexes with pyrazolyl ancillary ligands*. Polyhedron, **23** (2-3), 419 (2004).

[68] S. Obara, M. Itabashi, F. Okuda, S. Tamaki, Y. Tanabe, Y. Ishii, K. Nozaki, and M. Haga. *Highly phosphorescent iridium complexes containing both tridentate bis(benzimidazolyl)-benzene or -pyridine and bidentate phenylpyridine: Synthesis, photophysical properties, and theoretical study of ir-bis(benzimidazolyl) benzene complex*. Inorganic Chemistry, **45** (22), 8907 (2006).

[69] P. W. Atkins and R. S. Friedman. *Molecular Quantum Mechanics*. Oxford University Press, New York (1997).

[70] D. Beljonne, Z. Shuai, G. Pourtois, and J. L. Bredas. *Spin-orbit coupling and intersystem crossing in conjugated polymers: A configuration interaction description*. Journal of Physical Chemistry A, **105** (15), 3899 (2001).

[71] C. A. Masmanidis, H. H. Jaffe, and R. L. Ellis. *Spin-orbit-coupling in organic-molecules*. Journal of Physical Chemistry, **79** (19), 2052 (1975).

[72] Y. Komada, S. Yamauchi, and N. Hirota. *Phosphorescence and zero-field optically detected magnetic-resonance studies of the lowest excited triplet-states of organometallic diimine complexes .1. [Rh(Bpy)$_3$]$^{3+}$ and [Rh(Phen)$_3$]$^{3+}$*. Journal of Physical Chemistry, **90** (24), 6425 (1986).

[73] M. S. Hisayuki Miki, J. A. B. Tohru Azumi', and G. A. Crosby'. *Effect of the ligand-field strength on the radiative properties of the ligand-localized $^3\pi\pi*$ state of rhodium complexes with 1,10-phenanthroline. proposed role of dd states*. Journal of Physical Chemistry (1993).

[74] T. Azumi and H. Miki. *Spectroscopy of the spin sublevels of transition metal complexes*. Electronic and Vibronic Spectra of Transition Metal Complexes II, **191**, 1 (1997).

[75] H. Yersin and D. Donges. *Low-lying electronic states and photophysical properties of organometallic Pd(II) and Pt(II) compounds. Modern research trends presented in detailed case studies*. Transition Metal and Rare Earth Compounds: Excited States, Transitions, Interactions Ii, **214**, 81 (2001).

[76] Y. M. Cheng, Y. S. Yeh, M. L. Ho, P. T. Chou, P. S. Chen, and Y. Chi. *Dual room-temperature fluorescent and phosphorescent emission in 8-quinolinolate osmium(II) carbonyl complexes: Rationalization and generalization of intersystem crossing dynamics*. Inorganic Chemistry, **44** (13), 4594 (2005).

[77] K. C. Tang, K. L. Liu, and I. C. Chen. *Rapid intersystem crossing in highly phosphorescent iridium complexes*. Chemical Physics Letters, **386** (4-6), 437 (2004).

[78] G. J. Hedley, A. Ruseckas, and I. D. W. Samuel. *Ultrafast luminescence in Ir(ppy)₃*. Chemical Physics Letters, **450** (4-6), 292 (2008).

[79] A. L. Kamyshny, A. P. Suisalu, and L. A. Aslanov. *ODMR spectroscopy of coordination-compounds*. Coordination Chemistry Reviews, **117**, 1 (1992).

[80] W. J. Finkenzeller and H. Yersin. *Emission of Ir(ppy)₃. Temperature dependence, decay dynamics, and magnetic field properties*. Chemical Physics Letters, **377** (3-4), 299 (2003).

[81] K. Fesser, A. R. Bishop, and D. K. Campbell. *Optical-absorption from polarons in a model of polyacetylene*. Physical Review B, **27** (8), 4804 (1983).

[82] R. Osterbacka, C. P. An, X. M. Jiang, and Z. V. Vardeny. *Two-dimensional electronic excitations in self-assembled conjugated polymer nanocrystals*. Science, **287** (5454), 839 (2000).

[83] C. X. Sheng, M. Tong, S. Singh, and Z. V. Vardeny. *Experimental determination of the charge/neutral branching ratio eta in the photoexcitation of π-conjugated polymers by broadband ultrafast spectroscopy*. Physical Review B, **75** (8), 085206 (2007).

[84] H. Bässler. *Charge transport in disordered organic photoconductors a monte carlo simulation study*. physica status solidi (b), **175** (1), 15 (1993).

[85] P. W. M. Blom, M. J. M. de Jong, and M. G. van Munster. *Electric-field and temperature dependence of the hole mobility in poly(p-phenylene vinylene)*. Physical Review B, **55** (2), R656 (1997).

[86] P. W. M. Blom, M. J. M. de Jong, and J. J. M. Vleggaar. *Electron and hole transport in poly(p-phenylene vinylene) devices*. Applied Physics Letters, **68** (23), 3308 (1996).

[87] J. G. Müller, U. Lemmer, G. Raschke, M. Anni, U. Scherf, J. M. Lupton, and J. Feldmann. *Linewidth-limited energy transfer in single conjugated polymer molecules*. Physical Review Letters, **91** (26), (2003).

[88] W. Staroske, M. Pfeiffer, K. Leo, and M. Hoffmann. *Single-step triplet-triplet annihilation: An intrinsic limit for the high brightness efficiency of phosphorescent organic light emitting diodes*. Physical Review Letters, **98** (19), 4 (2007).

[89] J. C. Ribierre, A. Ruseckas, K. Knights, S. V. Staton, N. Cumpstey, P. L. Burn, and I. D. W. Samuel. *Triplet exciton diffusion and phosphorescence quenching in iridium(III)-centered dendrimers*. Physical Review Letters, **100** (1), 017402 (2008).

[90] Y. Kawamura, K. Goushi, J. Brooks, J. J. Brown, H. Sasabe, and C. Adachi. *100% phosphorescence quantum efficiency of ir(III) complexes in organic semiconductor films*. Applied Physics Letters, **86** (7), 3 (2005).

[91] S. C. Chang, G. He, F. C. Chen, T. F. Guo, and Y. Yang. *Degradation mechanism of phosphorescent-dye-doped polymer light-emitting diodes*. Applied Physics Letters, **79** (13), 2088 (2001).

[92] D. Y. Kondakov, W. C. Lenhart, and W. F. Nichols. *Operational degradation of organic light-emitting diodes: Mechanism and identification of chemical products*. Journal of Applied Physics, **101** (2), 7 (2007).

[93] N. C. Giebink, B. W. D'Andrade, M. S. Weaver, P. B. Mackenzie, J. J. Brown, M. E. Thompson, and S. R. Forrest. *Intrinsic luminance loss in phosphorescent small-molecule organic light emitting devices due to bimolecular annihilation reactions*. Journal of Applied Physics, **103** (4), 9 (2008).

[94] T. Förster. *Zwischenmolekulare Energiewanderung und Fluoreszenz*. Annalen der Physik, **2** (1-2), 55 (1948).

[95] T. Förster. *Experimentelle und theoretische Untersuchung des zwischenmolekularen Übergangs von Elektronenanregungsenergie*. Zeitschrift Fur Naturforschung Section a-a Journal of Physical Sciences, **4** (5), 321 (1949).

[96] D. L. Dexter. *A theory of sensitized luminescence in solids*. Journal of Chemical Physics, **21** (5), 836 (1953).

[97] C. Schildknecht. *Iridium-Carben-Komplexe als Farbstoffe für tiefblaue organische Leuchtdioden*. Dissertation, Technische Universtät Carolo-Wilhelmina zu Braunschweig (2006).

[98] M. A. Baldo and S. R. Forrest. *Transient analysis of organic electrophosphorescence: I. transient analysis of triplet energy transfer*. Physical Review B, **62** (16), 10958 (2000).

[99] S. Reineke, F. Lindner, G. Schwartz, N. Seidler, K. Walzer, B. Lussem, and K. Leo. *White organic light-emitting diodes with fluorescent tube efficiency*. Nature, **459** (7244), 234 (2009).

[100] H. Ishii, K. Sugiyama, E. Ito, and K. Seki. *Energy level alignment and interfacial electronic structures at organic metal and organic organic interfaces*. Advanced Materials, **11** (8), 605 (1999).

[101] M. A. Baldo and S. R. Forrest. *Interface-limited injection in amorphous organic semiconductors*. Physical Review B, **6408** (8), (2001).

[102] M. A. Baldo, D. F. O'Brien, M. E. Thompson, and S. R. Forrest. *Excitonic singlet-triplet ratio in a semiconducting organic thin film*. Physical Review B, **60** (20), 14422 (1999).

[103] M. A. Baldo, S. Lamansky, P. E. Burrows, M. E. Thompson, and S. R. Forrest. *Very high-efficiency green organic light-emitting devices based on electrophosphorescence*. Applied Physics Letters, **75** (1), 4 (1999).

[104] D. F. O'Brien, M. A. Baldo, M. E. Thompson, and S. R. Forrest. *Improved energy transfer in electrophosphorescent devices*. Applied Physics Letters, **74** (3), 442 (1999).

[105] S. Reineke, K. Walzer, and K. Leo. *Triplet-exciton quenching in organic phosphorescent light-emitting diodes with Ir-based emitters*. Physical Review B, **75** (12), 125328 (2007).

[106] G. F. He, O. Schneider, D. S. Qin, X. Zhou, M. Pfeiffer, and K. Leo. *Very high-efficiency and low voltage phosphorescent organic light-emitting diodes based on a p-i-n junction*. Journal of Applied Physics, **95** (10), 5773 (2004).

[107] A. Tsuboyama, H. Iwawaki, M. Furugori, T. Mukaide, J. Kamatani, S. Igawa, T. Moriyama, S. Miura, T. Takiguchi, S. Okada, M. Hoshino, and K. Ueno. *Homoleptic cyclometalated iridium complexes with highly efficient red phosphorescence and application to organic light-emitting diode*. Journal of the American Chemical Society, **125** (42), 12971 (2003).

[108] A. D. Becke. *Density-functional exchange-energy approximation with correct asymptotic-behavior*. Physical Review A, **38** (6), 3098 (1988).

[109] J. P. Perdew. *Density-functional approximation for the correlation-energy of the inhomogeneous electron-gas*. Physical Review B, **33** (12), 8822 (1986).

[110] A. Schäfer, C. Huber, and R. Ahlrichs. *Fully optimized contracted gaussian-basis set of triple zeat valence quality for atoms Li to Kr*. Journal of Chemical Physics, **100** (8), 5829 (1994).

[111] A. Klamt. *Conductor-like screening model for real solvents - a new approach to the quantitative calculation of solvation phenomena.* Journal of Physical Chemistry, **99** (7), 2224 (1995).

[112] R. Ahlrichs, M. Bar, M. Haser, H. Horn, and C. Kolmel. *Electronic-structure calculations on workstation computers - the program system turbomole.* Chemical Physics Letters, **162** (3), 165 (1989).

[113] Y. R. Sun, N. C. Giebink, H. Kanno, B. W. Ma, M. E. Thompson, and S. R. Forrest. *Management of singlet and triplet excitons for efficient white organic light-emitting devices.* Nature, **440** (7086), 908 (2006).

[114] H. B. Wu, J. H. Zou, F. Liu, L. Wang, A. Mikhailovsky, G. C. Bazan, W. Yang, and Y. Cao. *Efficient single active layer electrophosphorescent white polymer light-emitting diodes.* Advanced Materials, **20** (4), 696 (2008).

[115] T. Sajoto, P. I. Djurovich, A. Tamayo, M. Yousufuddin, R. Bau, M. E. Thompson, R. J. Holmes, and S. R. Forrest. *Blue and near-UV phosphorescence from iridium complexes with cyclometalated pyrazolyl or N-heterocyclic carbene ligands.* Inorganic Chemistry, **44** (22), 7992 (2005).

[116] S. J. Yeh, M. F. Wu, C. T. Chen, Y. H. Song, Y. Chi, M. H. Ho, S. F. Hsu, and C. H. Chen. *New dopant and host materials for blue-light-emitting phosphorescent organic electroluminescent devices.* Advanced Materials, **17** (3), 285 (2005).

[117] F. C. Chen, G. F. He, and Y. Yang. *Triplet exciton confinement in phosphorescent polymer light-emitting diodes.* Applied Physics Letters, **82** (7), 1006 (2003).

[118] S. R. Forrest, D. D. C. Bradley, and M. E. Thompson. *Measuring the efficiency of organic light-emitting devices.* Advanced Materials, **15** (13), 1043 (2003).

[119] Y. Sun and S. R. Forrest. *Enhanced light out-coupling of organic light-emitting devices using embedded low-index grids.* Nature Photonics, **2** (8), 483 (2008).

[120] J. Kalinowski, W. Stampor, J. Mezyk, M. Cocchi, D. Virgili, V. Fattori, and P. Di Marco. *Quenching effects in organic electrophosphorescence.* Physical Review B, **66** (23), 15 (2002).

[121] R. J. Holmes, S. R. Forrest, T. Sajoto, A. Tamayo, P. I. Djurovich, and M. E. Thompson. *Reduced geminate recombination in iridium-based electrophosphorescent materials.* Organic Electronics, **7** (3), 163 (2006).

[122] R. Kersting, U. Lemmer, M. Deussen, H. J. Bakker, R. F. Mahrt, H. Kurz, V. I. Arkhipov, H. Bässler, and E. O. Gobel. *Ultrafast field-induced dissociation of excitons in conjugated polymers.* Physical Review Letters, **73** (10), 1440 (1994).

[123] B. Ruhstaller, S. A. Carter, S. Barth, H. Riel, W. Riess, and J. C. Scott. *Transient and steady-state behavior of space charges in multilayer organic light-emitting diodes*. Journal of Applied Physics, **89** (8), 4575 (2001).

[124] C. Adachi, R. C. Kwong, P. Djurovich, V. Adamovich, M. A. Baldo, M. E. Thompson, and S. R. Forrest. *Endothermic energy transfer: A mechanism for generating very efficient high-energy phosphorescent emission in organic materials*. Applied Physics Letters, **79** (13), 2082 (2001).

[125] R. J. Holmes, S. R. Forrest, Y. J. Tung, R. C. Kwong, J. J. Brown, S. Garon, and M. E. Thompson. *Blue organic electrophosphorescence using exothermic host-guest energy transfer*. Applied Physics Letters, **82** (15), 2422 (2003).

[126] S. Tokito, T. Iijima, Y. Suzuri, H. Kita, T. Tsuzuki, and F. Sato. *Confinement of triplet energy on phosphorescent molecules for highly-efficient organic blue-light-emitting devices*. Applied Physics Letters, **83** (3), 569 (2003).

[127] T. Sajoto, A. B. Tamayo, P. I. Djurovich, M. Yousufuddin, R. Bau, M. E. Thompson, R. J. Holmes, and S. R. Forrest. *Recent progress in blue phosphorescent iridium(III) complexes and their application to organic light emitting devices (OLEDs)*. Abstracts of Papers of the American Chemical Society, **229**, U1031 (2005).

[128] J. Li, P. I. Djurovich, B. D. Alleyne, M. Yousufuddin, N. N. Ho, J. C. Thomas, J. C. Peters, R. Bau, and M. E. Thompson. *Synthetic control of excited-state properties in cyclometalated Ir(III) complexes using ancillary ligands*. Inorganic Chemistry, **44** (6), 1713 (2005).

[129] P. Erk, M. Bold, M. Egen, E. Fuchs, T. Geß ner, K. Kahle, C. Lennartz, O. Molt, S. Nord, H. Reichelt, and C. Schildknecht. *Efficient deep blue triplet emitters for OLEDs*. PCT Patent Application WO (2006).

[130] E. W. Mei, S. Vinogradov, and R. M. Hochstrasser. *Direct observation of triplet state emission of single molecules: Single molecule phosphorescence quenching of metalloporphyrin and organometallic complexes by molecular oxygen and their quenching rate distributions*. Journal of the American Chemical Society, **125** (43), 13198 (2003).

[131] M. Vacha, Y. Koide, M. Kotani, and H. Sato. *Photobleaching and single molecule detection of a phosphorescent organometallic iridium(III) complex*. Journal of Luminescence, **107** (1-4), 51 (2004).

[132] Y. Koide, S. Takahashi, and M. Vacha. *Simultaneous two-photon excited fluorescence and one-photon excited phosphorescence from single molecules of an organometallic complex Ir(ppy)$_3$*. Journal of the American Chemical Society, **128** (34), 10990 (2006).

[133] B. Liang, C. Y. Jiang, Z. Chen, X. J. Zhang, H. H. Shi, and Y. Cao. *New iridium complex as high-efficiency red phosphorescent emitter in polymer light-emitting devices*. Journal of Materials Chemistry, **16** (13), 1281 (2006).

[134] T. Tsuzuki and S. Tokito. *Highly efficient, low-voltage phosphorescent organic light-emitting diodes using an iridium complex as the host material*. Advanced Materials, **19** (2), 276 (2007).

[135] D. Hertel and K. Meerholz. *Triplet-polaron quenching in conjugated polymers*. Journal of Physical Chemistry B, **111** (42), 12075 (2007).

[136] M. J. Walter. *Spinkorrelationen in polymerischen Halbleitern*. Diplomarbeit, (Ludwig-Maximilians-Universität München) (2005).

[137] W. E. Moerner and L. Kador. *Optical-detection and spectroscopy of single molecules in a solid*. Physical Review Letters, **62** (21), 2535 (1989).

[138] G. Binnig, C. F. Quate, and C. Gerber. *Atomic force microscope*. Physical Review Letters, **56** (9), 930 (1986).

[139] G. Binning, H. Rohrer, C. Gerber, and E. Weibel. *Surface studies by scanning tunneling microscopy*. Physical Review Letters, **49** (1), 57 (1982).

[140] S. Weiss. *Fluorescence spectroscopy of single biomolecules*. Science, **283** (5408), 1676 (1999).

[141] W. E. Moerner. *A dozen years of single-molecule spectroscopy in physics, chemistry, and biophysics*. Journal of Physical Chemistry B, **106** (5), 910 (2002).

[142] P. Tamarat, A. Maali, B. Lounis, and M. Orrit. *Ten years of single-molecule spectroscopy*. Journal of Physical Chemistry A, **104** (1), 1 (2000).

[143] P. Tinnefeld and M. Sauer. *Branching out of single-molecule fluorescence spectroscopy: Challenges for chemistry and influence on biology*. Angewandte Chemie-International Edition, **44** (18), 2642 (2005).

[144] J. Müller. *Exzitonentransfer und Dissoziationsdynamik in konjugierten Polymeren*. Dissertation, Ludwig-Maximilians-Universität München (2003).

[145] J. M. Lupton. *A molecular thermometer based on long-lived emission from platinum octaethyl porphyrin*. Applied Physics Letters, **81** (13), 2478 (2002).

[146] Y. Sheng, T. D. Nguyen, G. Veeraraghavan, O. Mermer, and M. Wohlgenannt. *Effect of spin-orbit coupling on magnetoresistance in organic semiconductors*. Physical Review B, **75** (3), 035202 (2007).

[147] D. Hertel, S. Setayesh, H. G. Nothofer, U. Scherf, K. Mullen, and H. Bässler. *Phosphorescence in conjugated poly(para-phenylene)-derivatives*. Advanced Materials, **13** (1), 65 (2001).

[148] J. S. Wilson, N. Chawdhury, M. R. A. Al-Mandhary, M. Younus, M. S. Khan, P. R. Raithby, A. Kohler, and R. H. Friend. *The energy gap law for triplet states in Pt-containing conjugated polymers and monomers*. Journal of the American Chemical Society, **123** (38), 9412 (2001).

[149] M. Segal, M. Singh, K. Rivoire, S. Difley, T. Van Voorhis, and M. A. Baldo. *Extrafluorescent electroluminescence in organic light-emitting devices*. Nature Materials, **6** (5), 374 (2007).

[150] G. D. Scholes and G. Rumbles. *Excitons in nanoscale systems*. Nature Materials, **5** (9), 683 (2006).

[151] W. J. Finkenzeller, M. E. Thompson, and H. Yersin. *Phosphorescence dynamics and spin-lattice relaxation of the OLED emitter Ir(btp)$_2$(acac)*. Chemical Physics Letters, **444** (4-6), 273 (2007).

[152] W. E. Moerner and M. Orrit. *Illuminating single molecules in condensed matter*. Science, **283** (5408), 1670 (1999).

[153] K. Becker, E. Da Como, J. Feldmann, F. Scheliga, E. T. Csanyi, S. Tretiak, and J. M. Lupton. *How chromophore shape determines the spectroscopy of phenylene-vinylenes: Origin of spectral broadening in the absence of aggregation*. Journal of Physical Chemistry B, **112** (16), 4859 (2008).

[154] B. J. Schwartz. *Conjugated polymers: What makes a chromophore?*. Nature Materials, **7** (6), 427 (2008).

[155] J. A. Veerman, M. F. Garcia-Parajo, L. Kuipers, and N. F. van Hulst. *Time-varying triplet state lifetimes of single molecules*. Physical Review Letters, **83** (11), 2155 (1999).

[156] R. Zondervan, F. Kulzer, S. B. Orlinskii, and M. Orrit. *Photoblinking of rhodamine 6G in poly(vinyl alcohol): Radical dark state formed through the triplet*. Journal of Physical Chemistry A, **107** (35), 6770 (2003).

[157] J. P. Hoogenboom, E. van Dijk, J. Hernando, N. F. van Hulst, and M. F. Garcia-Parajo. *Power-law-distributed dark states are the main pathway for photobleaching of single organic molecules*. Physical Review Letters, **95** (9), 4 (2005).

[158] A. F. Rausch, M. E. Thompson, and H. Yersin. *Matrix effects on the triplet state of the OLED emitter Ir(4,6-dFppy)$_2$(pic) (FIrpic): Investigations by high-resolution optical spectroscopy*. Inorganic chemistry, **48** (5), 1928 (2009).

[159] T. Basche, S. Kummer, and C. Brauchle. *Direct spectroscopic observation of quantum jumps of a single-molecule*. Nature, **373** (6510), 132 (1995).

[160] T. Guillet, J. Berrehar, R. Grousson, J. Kovensky, C. Lapersonne-Meyer, M. Schott, and V. Voliotis. *Emission of a single conjugated polymer chain isolated in its single crystal monomer matrix*. Physical Review Letters, **87** (8), 4 (2001).

[161] F. Schindler and J. M. Lupton. *Single chromophore spectroscopy of meh-ppv: Homing-in on the elementary emissive species in conjugated polymers*. ChemPhysChem, **6** (5), 926 (2005).

[162] P. Tinnefeld, J. Hofkens, D. P. Herten, S. Masuo, T. Vosch, M. Cotlet, S. Habuchi, K. Mullen, F. C. De Schryver, and M. Sauer. *Higher-excited-state photophysical pathways in multichromophoric systems revealed by single-molecule fluorescence spectroscopy*. ChemPhysChem, **5** (11), 1786 (2004).

[163] D. A. VandenBout, W. T. Yip, D. H. Hu, D. K. Fu, T. M. Swager, and P. F. Barbara. *Discrete intensity jumps and intramolecular electronic energy transfer in the spectroscopy of single conjugated polymer molecules*. Science, **277** (5329), 1074 (1997).

[164] E. Da Como, K. Becker, J. Feldmann, and J. M. Lupton. *How strain controls electronic linewidth in single beta-phase polyfluorene nanowires*. Nano Letters, **7** (10), 2993 (2007).

[165] K. Becker. *Kontrolle des Energietransfers in hybriden und π-konjugierten Systemen*. Dissertation, Ludwig-Maximilians-Universität München (2007).

[166] W. J. Finkenzeller, T. Hofbeck, M. E. Thompson, and H. Yersin. *Triplet state properties of the OLED emitter Ir(btp)$_2$(acac): Characterization by site-selective spectroscopy and application of high magnetic fields*. Inorganic Chemistry, **46** (12), 5076 (2007).

[167] B. Minaev, H. Agren, and F. De Angelis. *Theoretical design of phosphorescence parameters for organic electro-luminescence devices based on iridium complexes*. Chemical Physics, **358** (3), 245 (2009).

[168] R. Bauer, W. J. Finkenzeller, U. Bogner, M. E. Thompson, and H. Yersin. *Matrix influence on the oled emitter ir(btp)$_2$(acac) in polymeric host materials - studies by persistent spectral hole burning*. Organic Electronics, **9** (5), 641 (2008).

[169] P. D. Reilly and J. L. Skinner. *Spectral diffusion of single-molecule fluorescence - a probe of low-frequency localized excitations in disordered crystals*. Physical Review Letters, **71** (25), 4257 (1993).

[170] P. Y. Chen and T. J. Meyer. *Medium effects on charge transfer in metal complexes*. Chemical Reviews, **98** (4), 1439 (1998).

[171] A. P. Monkman, H. D. Burrows, L. J. Hartwell, L. E. Horsburgh, I. Hamblett, and S. Navaratnam. *Triplet energies of π-conjugated polymers*. Physical Review Letters, **86** (7), 1358 (2001).

[172] A. Zahlan. *The Triplet State*. Cambridge University Press, London (1967).

[173] T. Tsuzuki and S. Tokito. *Highly efficient phosphorescent organic light-emitting diodes using alkyl-substituted iridium complexes as a solution-processible host material*. Applied Physics Express, **1** (2), 3 (2008).

[174] B. Schweitzer, V. I. Arkhipov, and H. Bässler. *Field-induced delayed photoluminescence in a conjugated polymer*. Chemical Physics Letters, **304** (5-6), 365 (1999).

[175] J. G. Müller, U. Lemmer, J. Feldmann, and U. Scherf. *Precursor states for charge carrier generation in conjugated polymers probed by ultrafast spectroscopy*. Physical Review Letters, **88** (14), 4 (2002).

[176] K. Brunner, A. van Dijken, H. Borner, J. Bastiaansen, N. M. M. Kiggen, and B. M. W. Langeveld. *Carbazole compounds as host materials for triplet emitters in organic light-emitting diodes: Tuning the homo level without influencing the triplet energy in small molecules*. Journal of the American Chemical Society, **126** (19), 6035 (2004).

[177] M. Deussen, P. H. Bolivar, G. Wegmann, H. Kurz, and H. Bässler. *Electric field-induced photoluminescence quenching in molecularly doped polymer light-emitting diodes*. Chemical Physics, **207** (1), 147 (1996).

[178] J. Mezyk, F. Meinardi, R. Tubino, and M. Cocchi. *Exciton dissociation in tris(2-phenylpyridine) iridium (III) probed by electric field-assisted time-resolved photoluminescence*. Applied Physics Letters, **93** (9), 3 (2008).

[179] J. Kalinowski, J. Mezyk, F. Meinardi, R. Tubino, M. Cocchi, and D. Virgili. *Phosphorescence response to excitonic interactions in ir organic complex-based electrophosphorescent emitters*. Journal of Applied Physics, **98** (6), 9 (2005).

[180] F. Cicoira and C. Santato. *Organic light emitting field effect transistors: Advances and perspectives*. Advanced Functional Materials, **17** (17), 3421 (2007).

[181] M. Muccini. *A bright future for organic field-effect transistors*. Nature Materials, **5** (8), 605 (2006).

Acknowledgments

Hallermann, Thomas Limmer, Alexander Urban and *Dr. Enrico Da Como* for proof-reading of my thesis.

My gratitude goes also goes to *Werner Stadler, Stefan Niedermaier, Dr. Andrey Rogach, Anna Helfrich, Christian Holopirek, Slavica Vrankovic, Gerlinde Adam* and *Irmgard Beier* for the supporting and the available help in many chemical, electronic, administerial oriented questions during my time in the group.

A special thank goes to all the people from my private environment. I would like to thank my *brother and his family* and especially my girlfriend *Anke Kinzler*, who gave me mental support during the last year of my thesis. Finally of course, I would like to thank from the bottom of my heart my parents *Helga and Franz Haneder*, who supported me during my studies, my dissertation and in fact during my hole life. You are the best parents one could wish for.

Curriculum Vitae

Personal details

Name	Stephan Haneder
Date of birth	20.02.1979
Place of birth	Regensburg

Education

Since 07/2006	Ph.D. student and position as researcher
	Ludwig-Maximilians Universität München
	Photonics and optoelectronics group (Prof. J. Feldmann)
	Title: *Correlation between electronic structure and light emission properties in phosphorescent emitters*
10/2000 - 04/2006	Diploma degree in Physics
	Universität Regensburg
	Thesis titled: *Fourier spectroscopy on quantum wire intersubband structures* (Prof. W. Wegscheider)
07/1999 - 08/2000	Community service
	University hospital Regensburg
09/1990 - 07/1999	Secondary school
	Regental-Gymnasium-Nittenau

Internships

04/2004 - 07/2004	European Synchrotron Radiation Facility (Grenoble, France)
	Project: *Combined microindentation and synchrotron radiation microdiffraction applied to polymers*
07/2003 - 01/2004	Siemens VDO Automotive Systems (Regensburg)
	Collaboration in the team Software Verification; main tasks:
	Software-tests and analysis of errors
	Automation of software and hardware tests
07/2002 - 09/2002	Max-Planck-Institute for plasma physics
	Adaption and installation of software packages

Munich, November 2009